INFORMATION TO USERS

This manuscript has been reproduced from the microfilm master. UMI films the text directly from the original or copy submitted. Thus, some thesis and dissertation copies are in typewriter face, while others may be from any type of computer printer.

The quality of this reproduction is dependent upon the quality of the copy submitted. Broken or indistinct print, colored or poor quality illustrations and photographs, print bleedthrough, substandard margins, and improper alignment can adversely affect reproduction.

In the unlikely event that the author did not send UMI a complete manuscript and there are missing pages, these will be noted. Also, if unauthorized copyright material had to be removed, a note will indicate the deletion.

Oversize materials (e.g., maps, drawings, charts) are reproduced by sectioning the original, beginning at the upper left-hand corner and continuing from left to right in equal sections with small overlaps.

Photographs included in the original manuscript have been reproduced xerographically in this copy. Higher quality 6" x 9" black and white photographic prints are available for any photographs or illustrations appearing in this copy for an additional charge. Contact UMI directly to order.

ProQuest Information and Learning
300 North Zeeb Road, Ann Arbor, MI 48106-1346 USA
800-521-0600

Machining of Particulate Metal Matrix Composites

By

Mariam S. El-Gallab

A thesis submitted to the Faculty of Graduate Studies
in partial fulfilment of the degree of

Doctor of Philosophy

Department of Mechanical Engineering

McMaster University
Hamilton, Ontario,
Canada

September 1999

DOCTORATE OF PHILOSPOHY (1999) **MCMASTER UNIVERSITY**

(Mechanical Engineering) Hamilton Ontario

TITLE: Machining of Particulate Metal Matrix Composites

AUTHOR: Mariam S. El-Gallab,
B.Sc. in Mechanical Engineering
The American University in Cairo
M.Sc. in Mechanical Engineering
The American University in Cairo

SUPERVISOR: Professor M. Sklad

OF PAGES: xviii, 179

Abstract

Particulate metal matrix composites (PMMCs) are being widely used in the aerospace and automotive industry due to their favourable properties, mainly high specific strength and wear resistance. However, machining of particulate metal matrix composites presents a great challenge to the industry as the reinforcing particles easily abrade most of the common cutting tool materials. Polycrystalline diamond (PCD) tools appear to be the most practical type of tool material for machining PMMCs.

The first part of the presented research concentrates on experimentally identifying the effect of the various cutting parameters on the chip formation mechanism, which in turn influences the tool wear. Increasing the feed rate had a beneficial effect on the tool wear due to abrasion. This is attributed to the reduced contact between the tool and the abrading reinforcing particles in the chip. The experimental work also involved an evaluation of the damage introduced into the workpiece due to machining. This damage is in the form of crushed particles, cracks and voids around the particles. The surface finish of the workpiece is a reflection of the tool's wear state.

The second part of the research involved building up numerical models for the cutting tool and workpiece. Computer simulation of the machining process can potentially reduce the number of experimental iterations needed to determine the optimum cutting parameters, which are the ones that produce the minimum tool wear and least workpiece damage with minimum cost. The model stress results were verified through scanning electron microscopic observations as well as transmission electron microscopic analysis. The finite element models revealed that the area beneath the machined surface experiences high tensile stresses, which cause void formation around the reinforcing particles. These voids join up to form cracks, which have serious implications on the fatigue life of the machined part.

Further research into the changes introduced in the microstructure of the chip and machined workpiece is recommended, as this could help in fully understanding the stress state beneath the machined surface.

Acknowledgements

I would like to express my sincere gratitude to my advisor Dr. M. Sklad for the opportunity to work on this extremely exciting research and his sage advice.

I would also like to thank my thesis supervisory committee, Dr. Subramanian, Dr. Spence, Dr. Capson and Dr. Latto for their technical assistance throughout the research.

A special thanks to United Technologies and Pratt & Whitney for supporting the project, Mr. D. Dyer from GE superabrasives and Mr. R. Bruski from Duralcan USA for providing the tools and material used in the research.

My thanks also go to the staff of the department of mechanical engineering, Betty-Anne, Rebecca, Dave Schick, Ron Lodewyks, Jim McLaren and Joe Verhaeghe for all of their assistance.

My friends, Milica Kojovic, Grazyna Chochol, Lena Raykowski, Karl Griffin, Carl Smythe and Patrick Chiu for the moments of laughter that kept insanity at bay.

Finally, I would like to thank my mother, my father and my husband for their support and encouragement throughout my academic career.

This thesis is dedicated to my son, the joy of my life, Alexander and the dream for a better future for the next generation.

Table of Contents

Nomenclature

α	Tool rake angle
β	Friction angle between the chip and the tool rake face
ε^C	Constrained strain
ε^T	Thermal strain, transformation strain
ϕ	Shear plane angle
λ	Portion of the heat conducted back to the workpiece
μ	Coefficient of friction between the tool and chip
ρc	Volumetric specific heat
A	The cross-sectional area of each asperity
A_c	Chip cross-sectional area
A_{ct}	The tool/chip contact area
A_l	Area of the tool flank wear
Dvol	Volume of metal removed
F_c	Cutting Force

F_h	Thrust force
F_s	Shearing force
H_t	Hardness of the tool material
H_w	The actual contact pressure
K	Shear strength
K_s	Specific cutting pressure
L	Seizure contact length
N	Applied normal load
R	Ratio of the tool thermal conductivity to the workpiece thermal conductivity
T	Temperature
T_s	Shear plane temperature
V	Sliding velocity
$Z_{\alpha/2}$	Standard normal random variable for Type I error α
b	Width of cut
f	Feed rate

h	Characteristic length of the asperity
p_f	Energy liberated due to friction
q_f	Heat generated over the tool/chip contact length
r	Chip ratio
s_e	Effective composite strength
s_m	Effective strength of the matrix
s_p	Length of the shear zone
t_o , d	Undeformed chip thickness
u_p	Shear velocity on the primary shear plane
v	Chip velocity
v_c	Cutting speed
v_f	Velocity along the flank face
v_s	Chip velocity at the shear plane
w_o	Depth of cut

List of Tables

List of Figures

CHAPTER 1

INTRODUCTION

The next generation of the automotive vehicles will require an increase in the overall performance to fulfil their mission roles. Among the requirements is to increase the life of the rotor brakes. Such an improvement is well beyond the capabilities of the monolithic alloys currently utilised in the automotive industry, and it is unlikely that future improvements in the traditional materials will be capable of meeting the targets.

Metal matrix composites (MMCs) form one group of the new-engineered materials that have received considerable research since the first trials by Toyota in the early 1980s [1]. Metal matrix composites offer various advantages in applications where high specific strength, stiffness and wear resistance are required. MMCs are multi-phase materials consisting of ceramic reinforcing fibres/whiskers/particles suspended in a metallic or intermetallic matrix. The most common reinforcements are silicon carbide (SiC) and alumina (Al_2O_3). Aluminum, magnesium and titanium alloys are commonly used as the matrix material. The mass density of most MMCs is approximately one third that of steels, resulting in high specific strength and modulus. MMCs compete with superalloys, ceramics, plastics and redesigned steel parts in several aerospace and

automotive applications [2-5]. Particulate metal matrix composites (PMMCs) are of particular interest since they exhibit higher ductility and lower anisotropy than fibre reinforced MMCs [4-9].

While many engineering components made from PMMCs are produced by the near net shape forming and casting processes, they frequently require machining to achieve the desired dimensions and surface finish. Machining of PMMCs presents a significant challenge to the industry since a number of reinforcement materials are significantly harder than the commonly used high speed steel (HSS) tools and carbide tools [1-40]. The reinforcement phase causes rapid abrasive tool wear; thus, the widespread usage of PMMCs is considerably impeded by their poor machinability and high machining costs. Therefore, the main objective of the proposed work is to find the optimum cutting conditions for machining PMMCs. The research will concentrate on Aluminum A356/20%SiC PMMC, which is used in car rotor brakes for its superior wear resistance. Both experimental and analytical techniques will be used to arrive at the optimum cutting conditions, which are the cutting parameters (speed (v), feed rate (f) and depth of cut (d)), tool material and tool geometry. Optimum cutting conditions are the ones that yield the least tool wear, and consequently minimum tool change. Since measurement techniques for the temperatures and stresses generated in the cutting tool can give, at best, average results, numerical methods, such as the finite element method (F.E.M) is employed to develop a model for the cutting tool. Simulation of the cutting parameters using the F.E.M model would help find the optimum cutting parameters.

Moreover, since it is well known that machining causes various residual geometrical and metallurgical defects in the machined surface region [3-6], one cannot draw conclusive decisions about the machinability of any material by just looking at the tool wear and tool wear rates. Hence, the research includes investigating the effect of the different cutting parameters on the workpiece surface integrity, which has a notable impact on the performance of the machined part. Another F.E. model is developed for the chip and workpiece in order to study the effect of the various cutting parameters on the stresses developed in the workpiece near machined surface as well as the fracture of the matrix material during the chip formation process.

Before conducting the preliminary experimental cutting tests, an extensive literature review was conducted in order to:

1. Determine the parameters that play a key role in the economics of cutting PMMCs,
2. Identify the factors that were overlooked by previous researchers.

A recapitulation of the literature review on machining of PMMCs is presented in chapter 2 of this thesis. Factors affecting the stresses during machining are also summarised. The basic cutting force models and cutting terminology is also included in chapter 2. Chapter 2 also includes the literature review of the F.E. models for the cutting tool and workpiece. The various factors that influence the properties and strength of PMMCs are discussed in chapter 2. Moreover, critiques of the previous work reported in this field are presented. Further clarification of the objective of the thesis is included at the end of this chapter.

Chapter 3 summarises the experimental procedures conducted. These experimental procedures are divided into two main categories.

1. The cutting tests set-up (which includes cutting force and temperature measurements),
2. The examination of the wear of the cutting tools (tool flank wear measurement and scanning electron microscopic (SEM) observations). The produced chips were also examined under the microscope to identify the chip formation mechanism. The surface quality of the machined part was quantified through measurements of the surface roughness. The subsurface stress and damage state was identified through microhardness measurements and transmission electron microscopic (TEM) examination.

Chapter 4 includes a summary of the numerical models used in the research, which comprise the finite element models for both the tool and the workpiece. Both the thermal and mechanical models are presented in chapter 4. The assumptions adopted in the models are also clearly identified. The type of elements employed in the mesh generation are discussed. Finally, the mesh optimisation procedure adopted in the analysis is summarised.

Chapter 5 includes the results of the experimental work as well as the numerical models. A comparison between the experimental observations/measurements and the numerical results is also made.

The results included in chapter 5 are discussed in chapter 6. The numerical results of the workpiece model are further substantiated through X-ray measurements of residual stresses and TEM observations. The optimum cutting parameters (within the

scope of the research) are also identified. A simple machining cost analysis is also presented.

Finally, chapter 7 includes the concluding remarks and future research suggestions.

CHAPTER 2

LITERATURE REVIEW

Machining of particulate metal matrix composites (PMMCs) represent a significant challenge to the industry since the reinforcing particles heavily abrade the cutting tools. This chapter presents a review of the publications on machining of these composites. The study of machining, in general, involves several aspects, which all interact together. Thus, the first sections of the chapter concentrate on basic issues of machining, such as the mechanics of chip formation which depends on the cutting parameters, tool/chip interface conditions, i.e. friction, lubrication etc..., and the workpiece material flow characteristics. Temperature and heat generation in metal cutting influence the workpiece deformation characteristics as well as tool wear. Tool wear, in turn, is influenced by the chip formation mechanism. A review of the tool wear models is also presented.

The finite element method (F.E.M) has been utilized and proven to be effective in modeling the metal cutting process once the proper boundary conditions are applied. A critic of the different finite element models of the metal cutting process is, hence, presented.

The final section of the chapter concentrates on issues, which affect the machining of particulate metal matrix composites, such as their strength, flow characteristics and failure limits.

2.1 Mechanics of Chip Formation

In metal cutting material is removed by advancing a wedge shaped cutting tool into the workpiece body. Depending on the inclination of the cutting edge with respect to the direction of the movement of the cutting tool, the cutting action is classified as being orthogonal or oblique [41]. If the cutting edge is normal to the movement direction, the cutting is orthogonal (Fig. 2.1.1), it is otherwise oblique (Fig. 2.1.2). The formed chip can be classified as one of three types: continuous chip, continuous chip with a built up edge, and a discontinuous chip [41]. Chip formation takes place by shearing in the primary deformation zone. As a result of the very high shear stresses and pressures at the tool/chip interface, a secondary deformation at the chip/tool interface also occurs.

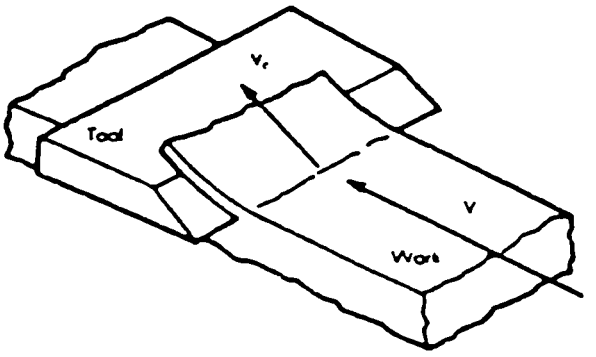

Figure 2.1.1: Geometry of Orthogonal Cutting [41]

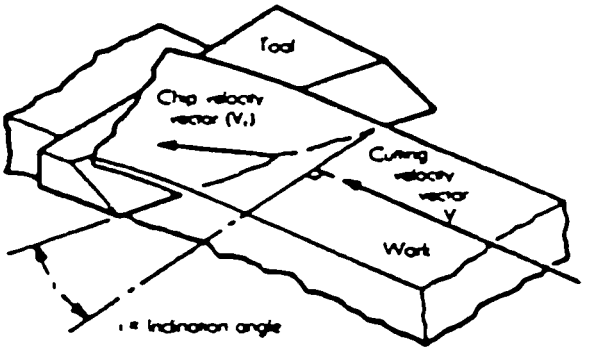

Figure 2.1.2: Geometry of Oblique Cutting [41]

Cutting parameters, workpiece material flow characteristics and thermo-physical properties and tool/chip interface conditions are all factors that affect the chip formation mechanism, which in turn affects the tool wear mechanism.

At low speeds (<1m/min) discontinuous chips are formed [42]. As the speed is increased, instabilities in the shearing process occur and result in partially segmented chips [43]. These instabilities are attributed to the void formation around the secondary phase particles in the workpiece material. These voids join up and form cracks that lead to the partial fracture of the chips. Other researchers [44] attributed the chip segmentation to strain hardening of the chip at the tool tip and thermal softening of the chip material at the end of the secondary shear zone.

Further increase in the cutting speed leads to the formation of shear localized chips. According to Komanduri et al [45], this type of chip deformation is confined to a narrow zone, which extends from the tool tip to the free surface. In this narrow zone (shear zone) temperature reaches the level at which the criterion for adiabatic instability are met. Concentration of the thermal energy in a narrow band or zone could be attributed to:

1. insufficient time for heat dissipation at high cutting speeds,
2. poor thermal properties of the workpiece material.

The large localized strains in a shear band often lead to fracture; the localized shearing greatly affects subsequent plastic deformation. Hence, shear bands have a dual significance: as a precursor to fracture and as a mechanism of large strain plastic deformation [46].

Researchers disagree about the mechanism behind the formation of segmented chips. Komanduri et al [47] viewed the mechanisms of the formation of segmented chips at high cutting speeds to start by plastic instability, which in turn leads to strain localization along a shear surface. The shear plane originates at the tool tip and extends almost parallel to the cutting velocity vector and gradually curves in until it meets the free surface. The formation of the chip is completed by gradual upsetting of the inclined wedge of the workpiece material ahead of the tool. Since there is almost no relative motion between the bottom surface of the chip and the tool face, then this model implies that the formation of fully segmented chips does not involve secondary deformation along the tool rake face, i.e. no seizure is involved. According to this theory, chemical wear of the cutting tool should be minimum with this type of chips. (A detailed discussion of tool wear is presented in section 2.6 of this thesis). On the other hand, Shaw [70] suggested that the formation of segmented chips at high cutting speeds is due to periodic gross fracture extending from the free surface of the chip inwards to the chip.

The important role of thermal softening in triggering the shear band deformation was recognized by Zener and Holloman in 1944 [48] who directed their research work towards the features contributing to and resulting from localization of strain and temperature. Other researchers, Recht [49], Culver [50], Backman [51], Merzer [52], Fressengeas [53], Olson [54] and Shawki [54], have studied the relative roles of thermal softening, strain hardening and strain rate sensitivity on shear localization under conditions where the onset of localization does not involve a substantial change in the stress state. Lemonds et al [46] developed a two dimensional

model that demonstrated the shear localization at strain rates up to 0.001 sec^{-1}. Thermal effects were also included in the model. The author of [46] discussed void initiation and growth as the destabilizing factor while the weakening induced by progressive micro-rupture can play an important role in triggering shear localization.

2.2 Friction in Metal Cutting

Tool/chip interface conditions, e.g. friction, plays a crucial role in the chip formation mechanism. Thus, the following subsection deals with friction in metal cutting.

Friction in metal cutting occurs in two areas: the tool flank/workpiece and the tool rake face/chip interfaces. The basic mechanisms of friction are adhesion and mechanical deformation.

Adhesion between the contacting surfaces dominate friction when the surfaces are very clean, which is the case in machining at high cutting speeds and at the tool tip vicinity. As a result, cold welding/seizure of the contacting asperities takes place. The strength of the adhesion bond between the contacting asperities is influenced by many factors, such as the degree of solubility of one material into the other, material phase, as demonstrated by the research carried out by Buckley [57] and the extent of plastic deformation. In metal cutting, interdiffusion between the adhering asperities can take place, leading to the formation of alloy compounds. The interdiffusion is assisted by the high temperatures generated during cutting.

Under seizure atomic contact at the tool/chip interface takes place. Hence, the layer of the tool chip in contact with the tool is stationary, yet relative motion takes place in the adjacent layers, where the shear velocity gradually increases until the bulk chip speed is reached [58-60]. Bowden et al [61] proposed that both the normal pressure and the shear stress determine the flow characteristics of the material under seizure conditions.

In metal cutting the friction force is the force required to shear off the welded asperities, plus the force required to plough the softer material surface by the action of the asperities of the harder material.

The distribution of the asperities at the interface layers play a major role in determining the interface conditions. Greenwood and Williams [62] developed a relation for the plastic flow of the asperities which depended on the material modulus of elasticity, indentation hardness and the geometry of the asperities.

To sum up, the effects of friction in metal cutting are rather complex due to the existence of high normal loads, which lead to the increase in the real area (sum of the asperities areas) of contact, and making it approach the apparent area of contact. When these conditions are reached, sticking friction is said to exist. Under sticking friction conditions, the coefficient of friction reaches the limiting value of 0.577, corresponding to τ_{max} according to Von Mises yield criterion. Also, the frictional force becomes independent of the normal force. The relative motion between the contacting surfaces, i.e. tool and chip, results in the dissipation of the energy in friction and shearing off the welded asperities or ploughing of the softer material.

2.3 Cutting Force Models for Orthogonal and Oblique Cutting

Many researchers have investigated forces in metal cutting operations. Ernst [63] and Merchant [64] pioneered in analyzing the chip formation mechanics and the latter developed models for the cutting forces, stresses and shear angle using the generalized relationships between vectors contained within the circle shown in Fig. 2.3.1. Merchant's approach had the following limiting assumptions:

1. continuous chip

2. shearing occurs in a plane

3. constant coefficient of friction (sliding or Coulomb friction) at the interface between the tool and the chip.

The model also neglected the thermo-plastic effects on the flow stress of the workpiece material.

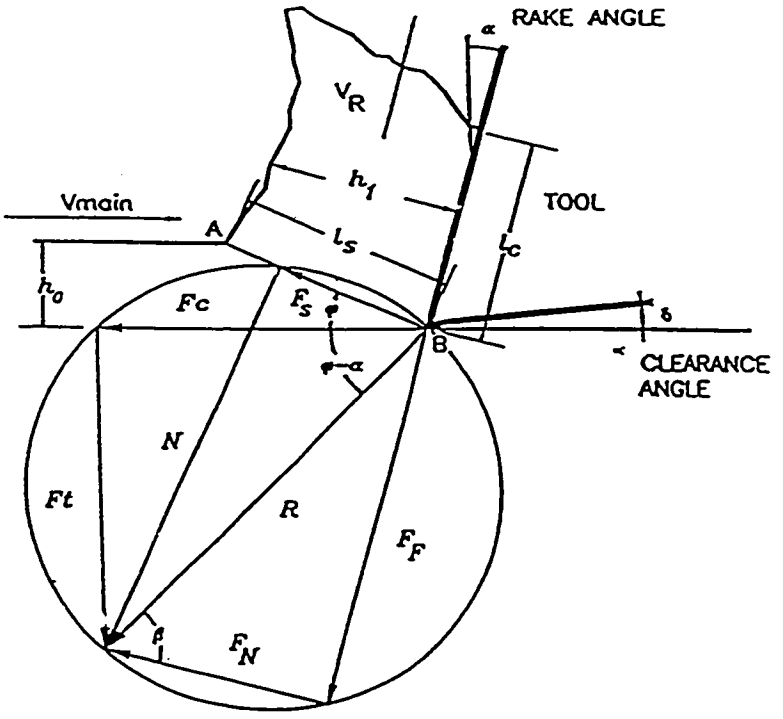

Figure 2.3.1: Merchant's force circle [65]

Lee and Shaffer [66] applied the same shear plane model to derive expressions for the shear angle based on minimizing the work done by the cutting forces. In a later publication, Lee and Shaffer [67] applied the slip line field theory to orthogonal metal cutting by assuming super plastic material behavior. However, neither of these models could incorporate the actual workpiece material behaviour into the model structure in a realistic way. Hence, the predicted results were not in agreement with the experimental observations made for different tool/workpiece material combinations. Moreover, it was stated by Boothroyd [68] that a unique relationship of the forms suggested by Merchant and Shaffer, for the prediction of shear and friction angles, can never hold for all materials. This is mainly due to the differences in the material properties, which have to be included into the shear angle and frictional angle relationships.

Later, Oxley et al [69] developed a shear zone model, as shown in Fig. 2.3.2. Another added feature of Oxley's model was the assumption of seizure at the tool tip. Oxley [70] further modified the model to account for the changes in the workpiece flow stress due to thermo-mechanical effects involved in the metal cutting process.

Wright [71] attempted to include the work material strain hardening properties obtained through tension tests in calculating the shear angle and friction angle. However, Baggci [72] in 1983 showed that unless the secondary shear zone effects are included, Wright's model could not hold for different combinations of tool geometries and work materials; so he proposed an experimental correction factor to take into account the different cutting conditions. Similar concepts have been applied by other researchers such as Yellowley [73] and Baily [74]. Nevertheless, there is, so far, no general model developed that can incorporate the various workpiece material

characteristics into the machining models without requiring additional experimental cutting force data.

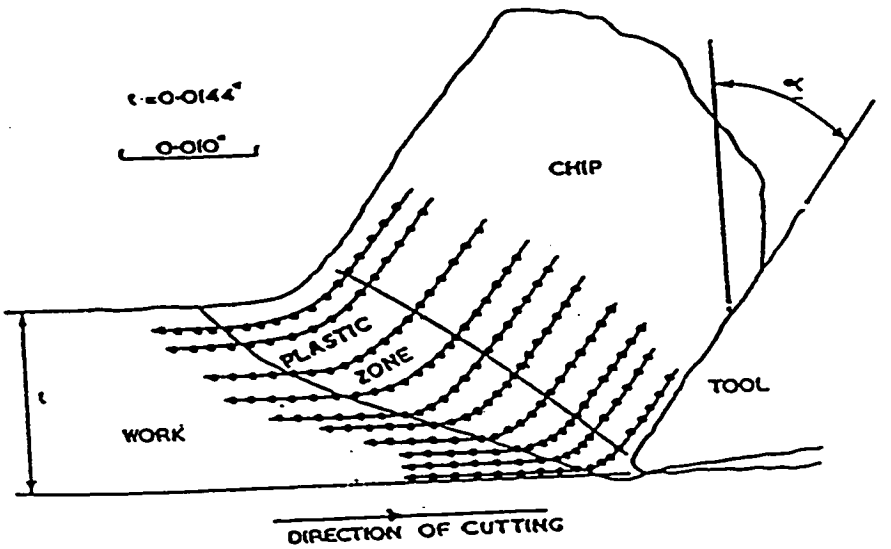

Figure 2.3.2: The Mathews,Hastings and Oxley shear zone model in metal cutting [69]

2.4 Stresses in Metal Cutting

The stress and strain distribution within the chip body was investigated by studying the deformed flow line patterns, Maruka et al[75]. It has been reported that the flow stress in the primary deformation zone remains nearly constant over a wide range of strains encountered in metal cutting. This is explained by the opposing effects of the strain hardening and temperature softening. Temperature distribution on the tool rake face is the factor which determines the force acting on the cutter and the temperature distribution at the interface surface. High compressive stresses and high temperatures are the two main factors affecting tool wear. Therefore, location and shape of the wear patterns, and the tool wear rate are directly influenced by the stress-strain and temperature distributions along the cutter face.

According to N.N. Zorev [76], the normal stress distribution in the tool-chip contact region may be closely represented by a power function. Alternatively, Palmer and Oxley [77] suggested that the chip does not come in contact with the tool near the edge point, i.e. normal stress does not exist there.

According to the work by Kato in 1972 [78] (in which split cutting tools and photoelastic analysis techniques were employed) the normal and shear stresses at the tool face were found to be distributed almost uniformly in the vicinity of the cutting edge. However, for brittle materials, the stresses were found to increase suddenly in close proximity of the cutting edge. The chip contact zone was found to depend closely on the undeformed chip thickness (a proportionality relationship exists). Moreover, according to Kato, the tool-chip contact region can be divided into two distinct zones, namely a plastic zone where stresses are distributed uniformly and an elastic recovery

zone where the stresses tend to zero away from the cutting edge. The extent of the plastic zone and the stress level reached there are influenced by the plastic deformation resistance of the material, frictional characteristics and strain hardening and temperature softening behaviour of the workpiece material. Fig. 2.4.1 shows the normal stress distribution for various ductile and brittle materials. It can be seen that for ductile materials the tool/chip contact length is much larger than those for brittle materials. As for the shear stresses , they were assumed to follow a similar trend as the normal stresses do, which indicates that the friction coefficient varies slightly along the tool/chip area.

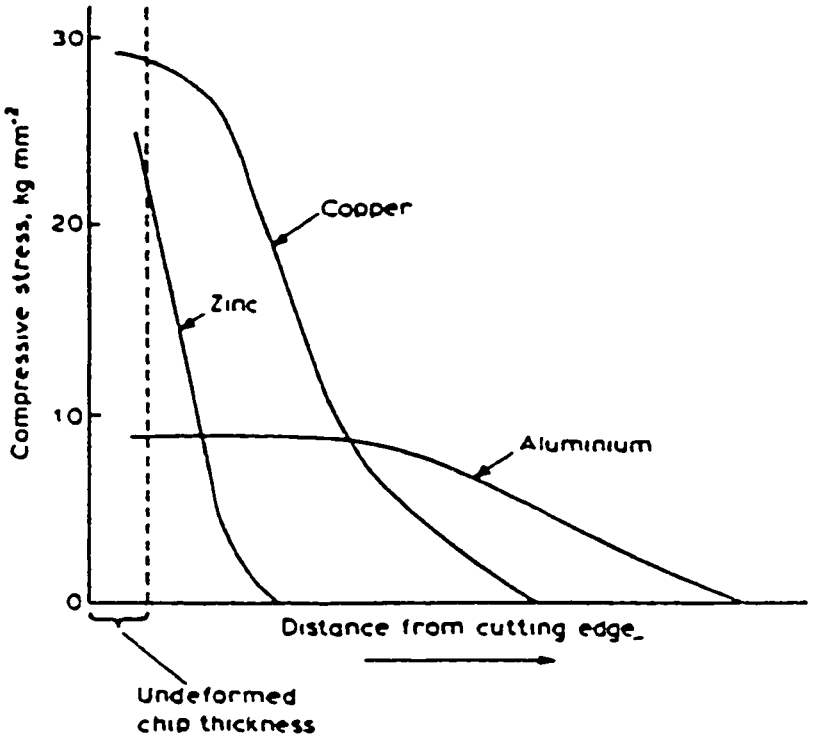

Figure 2.4.1: Typical Normal Load Distribution Along the Contact Length for Ductile (Cu and Al) and Brittle Zn [78]

Fig. 2.4.2 shows a general pattern of stress distribution along the tool/chip contact zone, where x is the distance from the cutting edge and σ and τ are the normal and shear stresses, respectively. Accordingly, the chip contact region can be divided into two distinct zones, a sticking zone ($0 < x < ls$) where stresses remain relatively constant and an associated sliding zone ($ls < x < lc$) where the contact stresses gradually decrease to zero. The average of this normal stress acting on a surface equal to the undeformed chip area, is called the pressure parameter and the ratio of the average normal stress to the average shear stress is called the friction parameter.

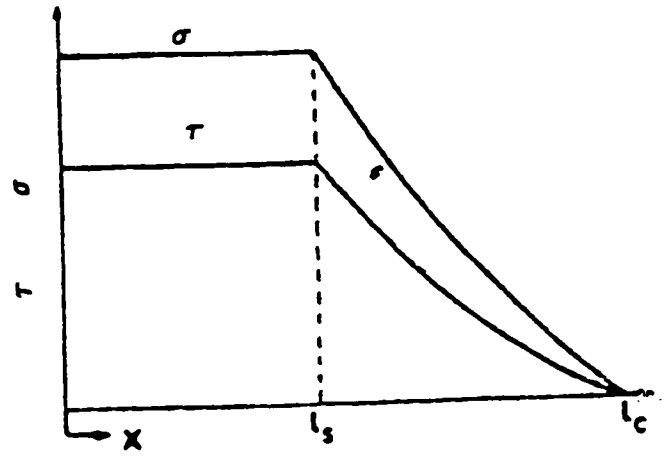

Figure 2.4.2: General Pattern of Stress Distribution [78]

Another model for the stress distribution on the tool cutting edge was proposed by Wright [79] after conducting tests with a transparent tool. The results indicated that the shear stresses are constant over the region of sticking friction and then decrease linearly over the tool/chip contact length. The normal stresses decrease linearly from the cutting edge and reach zero at the end of the contact length as shown in Fig. 2.4.3, where σ and τ are the normal and shear stresses, respectively.

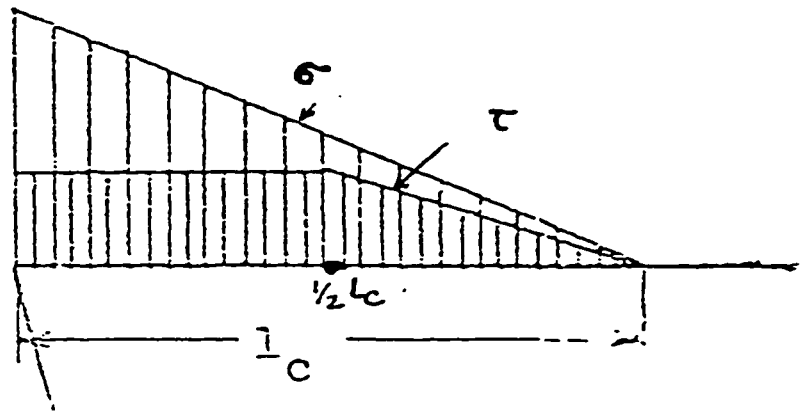

Figure 2.4.3: Stress Distribution on the Tool Cutting Edge [79]

2.5 Temperatures in Metal Cutting

Temperature in metal cutting is generated by the plastic deformation during the chip formation and interfacial frictional activities. High temperatures around the cutting edge accelerate the wear of the cutting tools. Temperatures at the tool/chip interface increase with the cutting speed, which therefore, limits the practical cutting speed for metals and alloys. Melting of the workpiece material at the cutter-chip interface due to high interface temperatures is reported [80].

Under the high strain rates encountered during metal cutting, the deformation work is converted into heat and temperature in the deformation zones. The temperature distribution in the cutting tool has long been of interest to those concerned with increasing the productivity of machine tools. This is because of the role of temperature in the tool wear as well as its effect on the surface integrity of the machined workpiece, which is discussed in section 2.8.4 of this thesis. Numerous investigators have dealt with the issue of temperature distribution using either experimental and/or analytical approaches. The main methods used to measure the cutting temperatures are: embedded thermocouples, tool/chip thermocouples, change in tool hardness, radiation pyrometers and thermo-colour techniques.

Direct measurement of tool temperatures is achieved by making holes in the tool close to the cutting edge and inserting a thermocouple to measure the temperatures at certain points. Significant errors may occur where the temperature gradients are steep, as the hole for the thermocouples may cover a considerable range of temperatures.

Tool/chip thermocouple is the most widely used technique to study the cutting temperatures. This method gives the mean temperature along the tool/chip interface. There are a number of sources of error in using the tool/chip thermocouple technique. In particular, the tool and work materials are not ideal elements for a thermocouple. Consequently, the emf tends to be low and the emf/temperature calibration is non-linear.

Temperature measurements using thermocouples necessitates the extrapolation of the temperature along the whole cutting edge using numerical techniques. On the other hand, estimating the tool temperature distribution through measurements of tool micro-hardness has proven to be successful once the calibration of the equipment is done accurately [81-82]. The hardness of the (tool/workpiece) material decreases as a result of the microstructure changes. These changes can be observed using optical and electron microscopes. These changes provide an effective means of determining temperature distributions in the tool during cutting. Micro-hardness measurements on tools after cutting can be used to determine constant temperature contours in the tools, but the technique is time consuming and requires very accurate hardness measurements.

Radiation techniques can be employed when the tool and workpiece can be observed directly. Cameras and films sensitive to infrared radiation are used to determine the temperature distributions.

Direct measurement of the temperature is difficult and can be performed only through destructive testing techniques [41]. Indirect measuring techniques are not accurate because of the high temperature gradients around the tool chip interface.

Alternatively, interface temperature distributions could be numerically analysed as done by several researchers [2.7].

The increase in temperature has a profound effect on the material's response. To illustrate this point, the increase in temperature could lead to thermal softening, which may lead to shear localization. This is because in most metals the dislocation movement is thermally activated. Thus, the increase in temperatures in the cutting tip vicinity affects the rate at which deformation and damage occur. Increasing the temperature results in lowering the stress-strain curve and increasing the fracture strain, thus Zener and Hollomon [83] proposed a temperature corrected strain rate parameter. Oxley et al [70] employed the velocity modified temperature rise due to plastic deformation.

Experimental measurements of the tool temperatures have demonstrated that equilibrium values of temperature are reached almost instantly after the start of cutting. The location of the maximum temperature, however, depends on the tool material as well as the cutting parameters. Figures 2.5.1 and 2.5.2 show typical temperature profiles (isotherms) in the cutting tools. High temperatures in the cutting tool tip promote the chemical wear of the tool as well as crater wear.

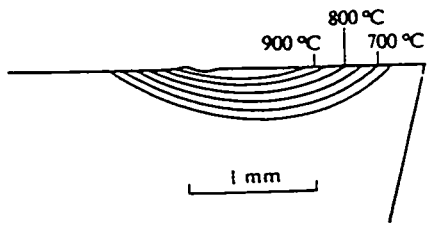

Figure 2.5.1: Isotherms for machining iron (0.04w/o C) at 183 m/min, feed rate of 0.25 mm/rev, depth of cut of 1.25 mm and cutting time = 30 sec. [41].

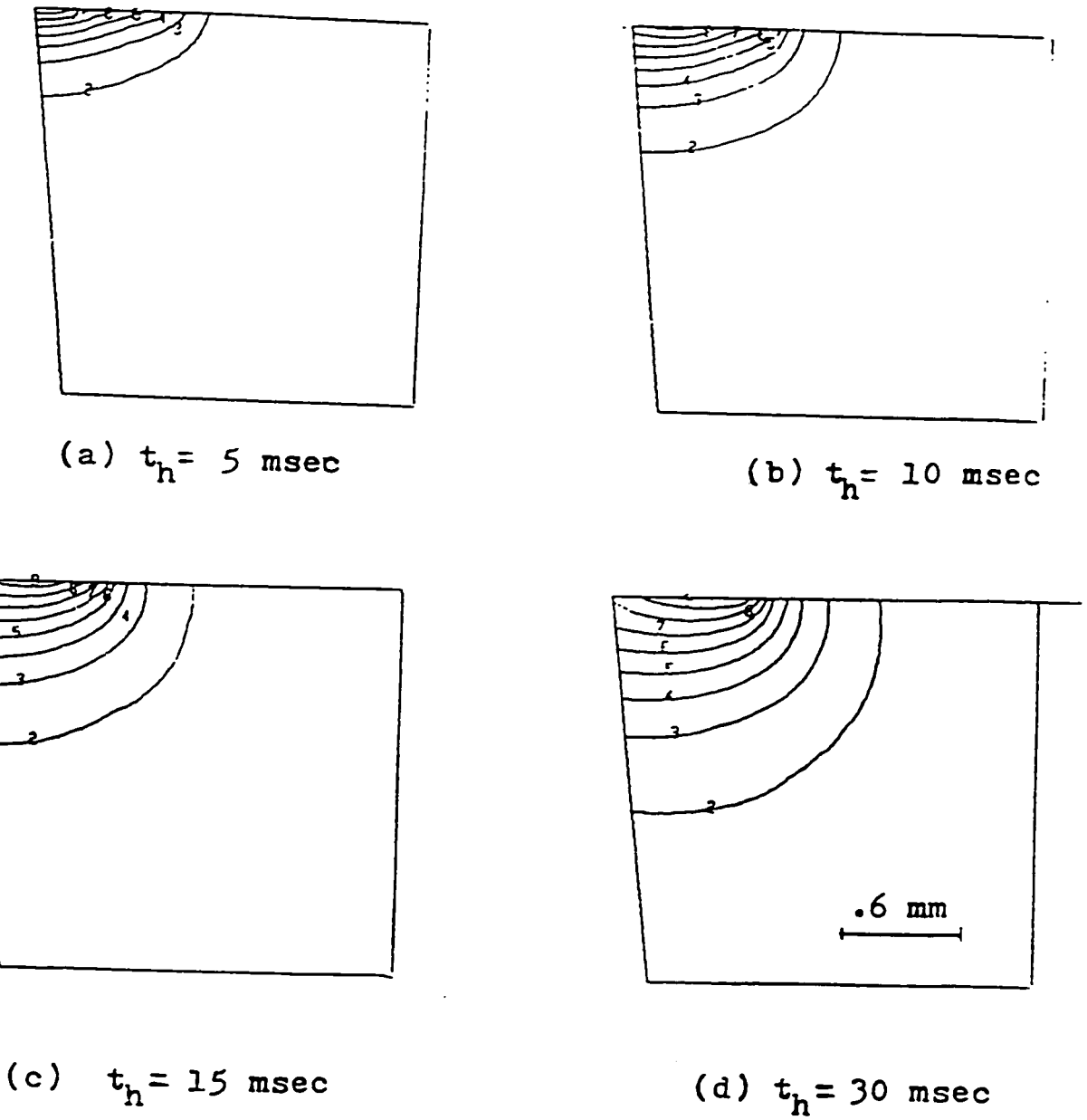

Figure 2.5.2: Temperature fields in a cutting cycle for halfimmersion up milling during the heating period [109]

2.6 Tool Wear

Understanding the tool wear mechanisms establishes the basis for reducing or preventing tool wear, and hence enhancing the economics of the metal cutting process as well as the produced workpiece surface integrity. In metal cutting tool wear can be broadly classified as physical and chemical wear. Physical wear includes: tool chipping, abrasion, attrition, and plastic deformation. Chemical wear, on the other hand, includes oxidation wear, corrosion and dissolution.

At low cutting speeds and when adhesion tendency between the chip and tool material is low abrasion wear dominates. Attrition wear occurs when small particles from the tool material are removed by the sliding chip as the weak adhesive junctions between the two materials are broken. The strength of the adhesion bond or weld between the tool and chip material increases as the cutting speed increases. This is attributed to the higher cutting temperatures and strain levels in the chip produced at high cutting speeds. At high cutting speeds seizure occurs. As a result of seizure, shear localized chips are produced. Furthermore, the chip layer adjacent to the tool face becomes intensely deformed (secondary deformation zone) [90]. Temperature at the tool/chip interface rises up as a result of the intense deformation.

If the tool material physical properties are such that heat dissipation from the tool tip is slow (i.e. low thermal conductivity and high specific heat) then the heat is accummulated in the tool tip area. These conditions could lead to thermal softening of the tool, that is to say the yield strength of the material is lowered to the extent to allow plastic deformation [91]. Plastic deformation of tools is reported in several publications [92].

The increase in temperature could also lead to another type of tool wear. This type of tool wear could be attributed to the chemical instability of the tool and chip material at high temperatures. Chemical instability can occur in various forms. For instance, the tool material could oxidize at high temperatures. Furthermore, under seizure conditions, dissolution wear takes place; the tool material is transported, by diffusion, to the chip . This type of tool wear is manifested in the form of crater wear. Ramanujachan and Subramanian [93] attributed the crater wear observed in machining AISI 12L14 and 1215 to diffusion. The researchers developed a finite element model to find the temperature distribution in the tool/chip seizure zone. The temperature profiles were then utilized in a quantitative model to predict the transport of tungsten from the tool into the chip by a diffusion mechanism. As a result of crater wear the tool tip becomes weak and is then subject to plastic deformation and edge chipping. Ingle [94] and Timothy [95] attributed the crater wear by diffusion and dissolution to the phase change incurred under high temperatures and compressive stresses present at the tool tip area.

Based on the aforementioned two broad divisions of tool wear mechanisms, some researchers attempted to develop models that predict the tool wear and tool wear rates. The following paragraphs summarize the most established tool wear models. Predicting the tool wear rate is crucial in the modern industrial environments as it helps reduce scrap workpieces and tool inventory. Two aspects of tool wear, namely abrasion and built-up edge, are presented in the following paragraphs. These wear mechanisms are found to be detrimental to the tool life during machining of particulate metal matrix composites (PMMCs).

Tool Abrasion Wear Models

According to Takeyama et al [96] the abrasion resistance of the tool is dependent on the tool temperature at the interface where the abrasion takes place. The workpiece ability to be abraded is dependent on the bulk temperature of the workpiece as it enters the shear zone. This temperature was chosen in place of the interface temperature since the ability of the workpiece to abrade depends not only on the hardness of the microscopic particles in the matrix, but also on the force with which these particles and the tool are brought together. This force is a function of the shear strength of the work material as it enters the zone of plastic deformation. Increasing the bulk temperature reduces both the hardness and the shear strength of the work material.

Although the abrasion tool wear model results have shown fair agreement with experimental observations during machining of hardened stainless steel, the model does not include the effect of the morphology of the abrasive inclusion on the tool wear rate. These effects were later included in a model developed by Kramer [97]. Kramer suggested that the abrasive wear behaviour might be separated into three regions depending on the ratio of the hardness of the abrasive to that of the surface that is being abraded. The model, which relies on experimental measurements, takes into consideration the shape and roughness of the abrading particles as well as the applied normal force between the surfaces and tool and inclusion hardness.

Investigations of Built-up Edge

According to Takeyama et al [98] fundamental conditions for the formation of a built-up edge are:

(1) The work material possesses an ability to strain harden;

(2) The existence of a suitable affinity between the work and the tool, that is suitable frictional characteristics at the tool/chip interface;

(3) The existence of a suitable temperature distribution in the plastic region of cutting;

(4) The existence of a suitable stress field in the plastic region of cutting.

Further, the authors separated the formation of a built-up edge into two stages:

(1) Adhesion between the tool and the work material through the origination of a nucleus of the built-up edge;

(2) Growth of the adhered material.

For the first stage, adhesion occurs through a process of diffusion where Takeyama et al applied Fick's laws of diffusion. The growth of the built-up edge could be modeled using the classical adhesive wear models, such as those presented by Kannatey [99] and Bhattacharyya et al [100].

According to Kannatey [99] the volume of metal removed from one material (dVol) and transferred to the surface of the mating material was found to be equal to :

$$dVol = (N/H_w)*(n/Lb)^{1/2}\, Vdt*(1/H_t) \qquad (2.6.1)$$

where,

dt: the time increment

V: the sliding velocity

n: number of asperity junctions

L: seizure contact length

b : width of the cut

N: applied normal load

H_W is the actual contact pressure, given by

$$H_W = N/(n*A) \tag{2.6.2}$$

where,

n is the number of welded asperities and A is the cross-sectional area of each asperity.

H_t is hardness given by:

$$H_t = K_O / h \tag{2.6.3}$$

where,

K_O is a constant and h is the characteristic length of asperities.

The literature review on the built-up edge indicates that generalized criteria for the BUE formation, size and shape are still being sought. The main obstacle in establishing these criteria is the fact that one cannot measure the actual size of the built-up edge. This is due to the fact that very often parts of the built-up edge break-off of the tool upon disengaging from the workpiece, leaving only a residual amount for measurement.

2.7 Heat Generation in Metal Cutting

During plastic deformation of the workpiece material, most of the energy is converted into heat. In metal cutting the material is subjected to extremely high strains, and the elastic deformation forms a very small proportion of the total deformation; therefore, it may be assumed that all the energy is converted into heat. Conversion of energy takes place in two principal regions of the plastic deformation as shown in Fig. 2.7.1-a. First, the shear zone or the primary deformation zone, AB - where heat is generated due to the plastic deformation associated with the chip formation. The second region is the secondary deformation zone BC which is the tool/chip interface where heat is generated due to frictional resistance between the chip and the tool. Moreover, a third source BD may be present due to flank wear, but the heat generated in this zone is comparably very small.

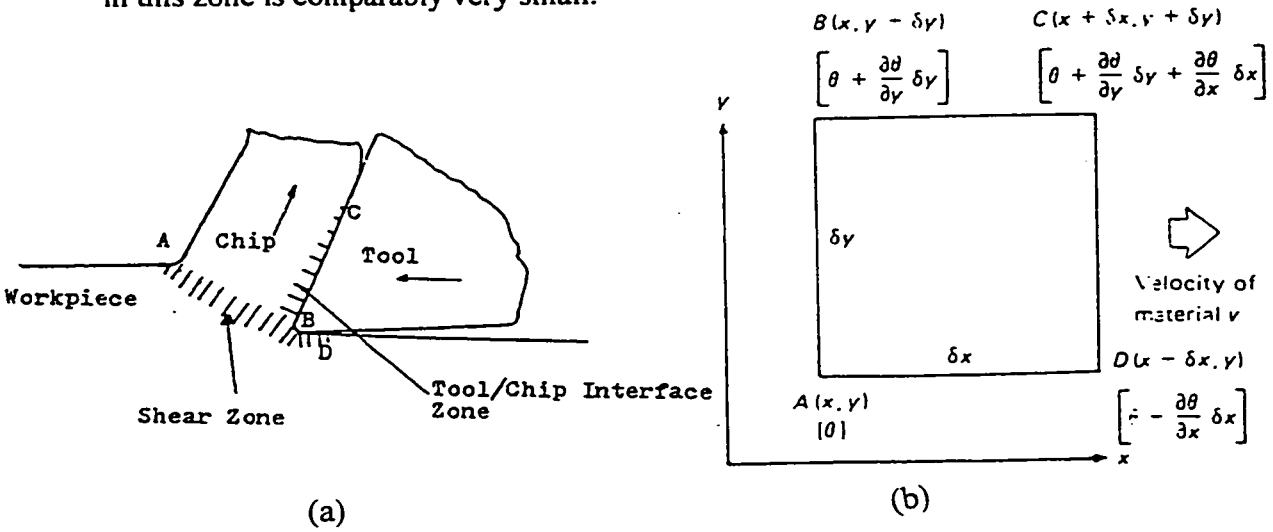

Figure 2.7.1: Generation of Heat in Orthogonal Cutting [68].

(a) Heat generation; (b) Heat transfer by chip transportation

The chip carries part of the primary deformation zone energy away while the other part is conducted back into the workpiece. The amount of heat conducted back to the workpiece depends mainly on factors such as the cutting speed, feed rate and the chip size, the combination of which makes the problem very complex. A closed form solution to this problem is not yet possible without further simplifying assumptions. Perhaps the most useful suggestion was made by Weiner [85] who assumed that no heat was conducted in the material in the direction of its motion. This assumption was shown to be justified in metal cutting because at high speeds the transfer of heat in the direction of motion is mainly by chip transportation (Fig. 2.7.1-b), and the conduction term can be neglected. Moreover, Nakayama [86] employed a thermocouple technique to measure the heat carried away by the workpiece and his results agree with the work of Weiner over the range of cutting conditions.

As for the tool/chip interface temperature, the solution of this problem involves the heat transfer calculation for stationary and moving heat sources. First, Rapier [87] proposed that the heat flux distribution along the tool/chip interface is a uniform plane source of heat. Then, Boothroyd [88] measured the temperature distribution in the tool, chip and workpiece using a photographic technique and proposed that the friction heat is distributed either over a triangular or rectangular area in the chip. The researcher also found that a triangular heat source distribution compares favorably with the experimental data. Lowen and Shaw [89] assumed that the heat flux distribution along the tool/chip interface is non-uniform. They employed the method of successive approximation to obtain the heat flux and the temperature distribution at the interface.

2.8 The Application of Finite Element Method in Metal Cutting

As early as 1971 it was realized that the finite element method is a useful approach for modeling metal cutting. There are several models based on the finite element method in the literature which investigate the effect of various cutting parameters on the thermal and mechanical stress and temperature distribution induced in the tool, chip and workpiece during cutting.

Tay et al [101] applied the finite element method to compute the temperature distribution in the workpiece, chip and tool. In their two dimensional analysis, the shear and tool/chip heat sources were considered to be distributed over a wide area of the chip. The distribution of the heat source was obtained from quick stop tests along with measured cutting forces. Their method gave relatively accurate results, but the preparation of the input data from the flow field was laborious. Hence, in their second publication they employed an analytical method to compute the velocity and strain in both the shear and tool/chip interface zones instead of the flow field. This method allowed the complete temperature distribution to be obtained given only experimental values of the cutting forces, chip thickness and thermal properties of the tool and workpiece materials.

Klamecki [102] in 1973 developed a three dimensional model for the tool, workpiece and chip. However, it was limited to only the initial stages of the chip formation. Later in 1982, Osui and Shirakshi [103] developed a finite element model which accounted for the chip formation under steady state cutting conditions, yet the analysis relied greatly on experimental data and was limited to rate independent deformation behaviour.

Tlusty and Masood [104] examined the problem of tool chipping and breakage of carbide inserts through an analysis of the stresses in the tool. This analysis was simplified to a two-dimensional, plane-strain, elastic problem. As a result, it was found that the stress distribution obtained was compatible with experimental and theoretical data only in regions away from the cutting edge and that the tensile stresses were maximum at a distance along the rake face of approximately three times the tool chip contact length.

Hsu [105] investigated the stresses in a tool during interrupted and continuous cutting and assumed initially, in interrupted cutting, that on impact only normal stresses would be acting on the tool face. The maximum shear stress was found to be very close to the cutting edge suggesting a major cause of chipping. It is unlikely, however, that initial contact conditions would be such that only a normal force is applied. When both normal and shear stresses were considered the position of the maximum shear stress was still within the tool/chip contact length, but it was now much further from the edge, reducing the likelihood of edge failure by chipping.

Stevenson, Wright and Chow [106] developed a finite element program for calculating the temperature distribution in the chip and the tool in continuous metal cutting. The program takes as an input a strain rate field and a set of conditions from quick stop tests using specimens printed with fine grids. The preparation of the input to the finite element module was quite laborious and thus the researchers developed another finite element model with a reduced mesh size. Discrepancies of about 50^{o}C (10%) between computed and measured temperatures were found. Also, the calculated isotherms were displaced along the tool rake face relative to those of the experiments.

These discrepancies were attributed to the fact that the calculations were based on a steady state basis, while in reality transient conditions exist.

Iwata, Osakada and Terasaka [107] in 1984 developed a numerical model for plane strain orthogonal cutting in steady state on the basis of a rigid-plastic finite element method. The shape of the chip and distribution of stresses and strains were calculated. In their method a trial model is first generated by giving the cutting conditions and the shape of the tool. The model is then modified by using the result of the plane strain finite element analysis. This modification was iterated until the obtained shape of the chip and the distribution of strain coincided with the assumed ones. This is a relatively time consuming process since the velocity field is computed by the finite element method for the trial model and the streamlines are drawn in each trial. Furthermore, the deformation model does not account for the elastic deformation. Thus, the residual stresses cannot be predicted based on this model.

Strenkowski and Carrol [108] in 1985 developed a finite element model of orthogonal metal cutting in which they introduced a new chip separation criterion based on the effective plastic strain in the workpiece. The tool friction along the tool rake face and the geometry of both the cutting edge and the workpiece were included. The model predicts the chip geometry and residual stresses as well as the temperature distribution in both the workpiece and the tool. The model is based on an updated Lagrangian formulation for plane strain conditions that was provided by the general-purpose code NIK2D. However, caution must be exercised in selecting an appropriate value of plastic strain for the chip separation if residual stresses are sought.

Orady [109] constructed a two-dimensional tool/chip model which reflects the interaction between the heat sources generated during cutting. A finite element program provides the capability of computing the transient temperature fields for both the cutting and non-cutting periods for peripheral milling. The model has, however, several simplifying assumptions concerning the material behaviour. It also assumes that the properties of the chip and the tool are temperature independent.

Dokainish et al [110] analyzed the stresses in the workpiece during exit in interrupted cutting with chamfered tools. An elastic-plastic finite element model was developed to examine the stress fields in the workpiece using various chamfer tools and exit angles. However, the cutting process was treated as a plane strain problem, and the tool was assumed to be rigid. Despite the limitations of their model, it predicted the tool expected failure by "foot-forming" which depended greatly on the tool exit angle as previously depicted by Pekelharing in 1978 [155].

Younis [111] constructed a tool model to determine the thermal and mechanical stresses in a carbide insert due to heat and cutting forces. Moreover, the flank wear effect was included in the model. The tool chipping and breakage were related to the stresses, which developed in the tool. Nevertheless, the model is limited to two-dimensional analysis only.

In 1990, Strenkowski and Moon [112] presented an Eulerian finite element model to simulate orthogonal steady state metal cutting. The process was treated as a large deformation process involving viscoplastic material. It was assumed that the elastic effects were negligible and hence the constitutive law turned into a viscous flow equation relating flow stress to the instantaneous strain rate. For this model, the initial

chip geometry was first approximated with a finite element grid, then nodal velocities were calculated for the interior and free surfaces of the chip. Non zero normal velocity components that occurred on the free surface were used to adjust the surface in the direction of the normal velocity component and the new chip geometry was formed with a new finite element grid. The velocity equation was then resolved until the normal velocity component on the free surfaces of the chip was found to be zero. This technique, however, is essentially suitable only for steady state situations.

Chan and Braiden [113] examined the effects of both mechanical and thermal loading on the tool and suggested that the rake face normal stress distribution was of a triangular form with a maximum value at the cutting edge. The shear stress distribution was assumed to be uniform over 5/8 of the contact length (sticking region) and decreasing in a linear manner to the end of the tool/chip contact zone. The tool was considered to be under plane strain.

Komvopoulous and Erpenbeck [114] in 1991 used the finite element method to model the chip formation in orthogonal metal cutting under plane strain assumptions. They performed a quasi-static finite element simulation to investigate the significance of the deformation of the workpiece on the cutting process. Elastic-perfectly plastic and elastic-plastic with isotropic strain hardening and strain rate sensitivity constitutive laws were used in the analysis. Yet, for simplicity, the tool material was modeled as a perfectly rigid part.

In 1992 Stevenson and Ali [115] analyzed the tool temperatures in interrupted metal cutting by modeling the tool tip as a semi-infinite rectangular plate heated by a time varying heat flux subject to various spatial distributions - mainly uniform,

triangular and exponential. However, for short heating cycles, discrepancies with the experimental measurements were large. One reason for these discrepancies is the over-simplified assumptions employed in partitioning the heat generated between the tool and the chip. Moreover, in their analysis the chip thickness was assumed to be constant, which is generally not the case in interrupted metal cutting processes, such as milling.

Ueda et al [116] developed a three dimensional model for the chip formation, where rigid plastic finite element method was employed. The model relied on measured forces and input chip geometry changes. Thermal effects were not included in the model.

Ahmad et al [117] developed a two-dimensional tool wedge model using a range of cutting geometries including tools with double rake angles. The results presented revealed the significance of the chosen boundary conditions. Their results also indicated that the region of tensile stresses might be as high as five times the contact length for negative rake cutting tools.

Bayoumi and Zbib [118] attempted to model the chip formation in orthogonal cutting. However, the chip separation was based on a predetermined line of separation between the workpiece and chip. Nodes on this line were separated when the tool tip was sufficiently close, or when a certain level of plastic strain was attained. Evidently, this simple approach was not capable of predicting the correct chip morphology.

Sekhon and Chenot [119] used mesh adaptivity to allow for an arbitrary surface of separation. However, elastic strains were not encountered for, which precluded the computation of residual stresses in the workpiece.

In 1994, Zang and Bagchi [120] developed a two dimensional model that simulates the chip formation. Two node link elements were used in the model to simulate chip separation. The chip and workpiece elements are connected using these link elements along a predefined separation line. The chip separation was initiated when the distance between the leading node and the tool edge was equal to or smaller than a given value.

Shih [121] developed a plane strain finite element model for the simulation of orthogonal metal cutting. The mesh size was optimized to control the number of elements within a computationally acceptable level.

In 1995 El-Wardany et al [122] developed a tool model for determining the temperature distribution in a ceramic tool during machining of a nickel based alloy. In their model a measured tool temperature was input into the finite element model. Neither the effect of tool/chip nor tool/workpiece interactions was taken into consideration in the model. Furthermore, the tool properties were assumed to be temperature independent and the material was assumed to have the elastic properties throughout the run, i.e. the model would have failed to predict any plastic deformation within the tool.

Marusich et al [123] developed a Lagrangian finite element model of orthogonal high speed machining. The model utilized continuous re-meshing to alleviate element distortion problem associated with the finite deformations encountered. Both ductile and brittle fracture initiation and propagation were accounted for during processing; an essential feature in determining shear-localized

chip morphologies. The model results agreed well with experimental observations for orthogonal cutting.

Athavale and Strenkowski [124] developed an Eulerian finite element model for the tool and chip. Although the model was limited to orthogonal cutting, the predicted chip breakage based on the accumulated damage in the chip material as well as the chip geometry was in fair agreement with experimental measurements for the range of the test conditions.

2.9 Particulate Metal Matrix Composites (PMMCs)

Metal matrix composites (MMCs) became important in their application to structural components as materials with improved specific strength, creep and wear properties at elevated temperatures. Yet machining of MMCs, and in particular partiulate metal matrix composites (PMMCs), present a challenge to industry. Understanding the strengthening mechanisms of the MMCs and PMMCs constitutes the basis for understanding their deformation during machining and hence the tool wear and resulting workpiece surface integrity.

There are several factors that influence the strengthening of PMMCs and their failure. Thus, the following sections attempt to summarize these different factors. While section 2.9.2 concentrates on some of these factors - such as matrix properties and particle volume fraction, morphology and spatial distribution, section 2.9.1 introduces some of the available models for the strength of these composites. Section 2.9.3 deals with the failure mechanisms of these composites as well as the effect of temperature on the damage accumulation in these composites. Section 2.9.4 includes a summary and

critics of the research carried out on the machining of PMMCs as well as the studies carried out on the residual stresses due to machining.

2.9.1 STRENGTHENING OF PMMCs

It is well known that the reinforcement of hard ceramic particles, fibre or whiskers in soft metallic matrices produces composites with substantially higher yield strength compared to that of the matrix. The strengthening effect is primarily attributed to two factors. Ramakrishnan, Nardone and Prew [31] proposed a *Shear Lag Model (MSL)* which ascribes the entire strengthening effect to the load bearing feature of the hard reinforcement. On the other hand, Vogelsang et al attributed the strengthening to mainly the enhanced strength of the matrix - due to the increase in the dislocation density of the matrix by several orders of magnitude. According to the *Enhanced Dislocation Density (EDD)* models the strengthening mainly depends on the reinforcement size and only weakly on the volume fraction. On the other hand, according to the MSL theory, the relationship between the effective composite strength, s_e, and the reference matrix strength, s_m, is expressed as:

$$s_e = s_m (1+f_l) \qquad (2.9.1)$$

where f_l is a factor that primarily depends on the volume fraction of the reinforcement in addition to the geometrical parameters such as aspect ratio and shape. Thus, according to the MSL theory, the composite strength, s_e, turns out to be insensitive to the reinforcement size, which contradicts several experimental studies.

In an attempt to generalize the MSL theory, Nardone et al revised the connotation of the matrix strength s_m (in equation (2.9.1)) to mean the enhanced

strength of the reinforced matrix, i.e., take into consideration both the load bearing effect of the reinforcement and the enhanced dislocation density of the matrix. The appropriate matrix strength could be evoked through a continuum mechanics approach or through employing the EDD model [31].

The increase in the dislocation density is assumed to be entirely due to the residual plastic strain developed due to the difference in the coefficient of thermal expansion of the reinforcement phase and the matrix during the post fabrication cooling. According to Ramakrishnan [31], the approximate models for the increase in dislocation density presented by Pickard et al, Mori and Mortensen all lack a systematic study of the effect of the volume fraction and the reinforcement size on the spatial distribution of the dislocation density and they also ignore the load bearing aspect of the reinforcement.

Ramkrishnan's model:

The residual stresses developed due to the difference in coefficient of thermal expansion can be large enough to induce plastic relaxation in the matrix and this increases the dislocation density by few orders of magnitude leading to the matrix strengthening. According to the study presented in [31] a composite sphere approximation of PMMCs, as shown in Fig. 2.9.1, is assumed to determine the dislocation density of the matrix.

The composite sphere, in its most general form, is assumed to comprise three zones (Fig. 2.9.1): elastic reinforcement, surrounding matrix plastic zone and outer elastic zone. A set of equations is established invoking the equilibrium and the compatibility conditions in the composite sphere; ideal plastic condition and volume

conservation are assumed in the plastic zone. Moreover, the temperature is assumed to be uniform in the entire composite sphere, but the temperature dependence of the material properties is taken into account. The flow stress is described using Von Mises effective stress.

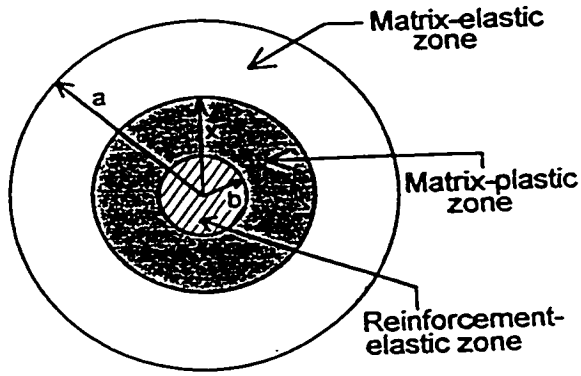

Figure 2.9.1: Composite sphere approximation of the particulate reinforced MMCs [31].

In this procedure, the increments of the residual stress and strain are established for a small decrease of the temperature, and in each step, the following boundary conditions are imposed:

a) the outer boundary is assumed radial stress free;

b) at the interface of the matrix-elastic and plastic zones as well as the particle-matrix interface, the radial stress and the tangential strain are assumed to be continuous;

c) across the interface of the matrix-elastic and the plastic zones, the Von Mises effective stress is prescribed to be continuous. Analysis of the model assumptions is presented in full detail by the author in [125].

Eshelby's Model

Wilkinson et al [32-35] and Davis et al [36] believe that PMMCs are distinguished from dispersion hardened systems, of which they are a natural extension, by the fact that, because the reinforcement is large (approximately 1-100 μm), it makes a negligible contribution to strengthening by Orowan inhibition of dislocation motion. In addition, since the volume fraction is relatively high (5-40%) the load transfer from the matrix is no longer insignificant. However, unlike continuously reinforced systems, the matrix strength, as affected by precipitation and dislocation strengthening, also plays an important role. According to Eshelby's theory [36] internal stresses arise as a result of some kind of misfit between the shapes of the constituents (matrix and reinforcement, i.e. fibre, whisker or particle). Such a misfit could arise from a temperature change, or created during mechanical loading - when a stiff inclusion tends to deform less than the surrounding matrix. The key point in Eshelby's model is that the *reinforcement is elliptical* in shape, can have any aspect ratio and has a uniform stress at all points within it. The technique is based on representing the actual inclusion by one made of matrix material (an "equivalent homogeneous inclusion") which has an appropriate strain (an equivalent transformation strain), such that the stress field is the same as for the actual inclusion.

Eshelby approached the problem by visualizing a series of cutting and welding exercises, as illustrated in Fig. 2.9.2. A region (the inclusion) is cut from the unstressed elastically homogeneous material, and is then imagined to undergo a shape change (the transformation strain ε^T) free from the constraining matrix (so that the strain is "stress-free). The inclusion cannot now be directly replaced back into the cavity from where it came. Instead surface tractions are first applied in order to return it to its original shape. Once back into position, the two regions are then welded together once more and the surface tractions are then removed. Equilibrium is then reached between the matrix and the inclusion as a constrained strain (ε^C) of the inclusion relative to its initial shape before removal.

Since the inclusions are strained uniformly throughout, the stress within it can be calculated using Hooke's Law in terms of the elastic strain ($\varepsilon^C - \varepsilon^T$) and the stiffness tensor of the material (C_M).

$$\varepsilon_1 = C_M (\varepsilon^C - \varepsilon^T) \tag{2.9.2}$$

For a specified shape change ε^T, all that is now required in order to calculate the inclusion stress is a knowledge of the final constrained strain ε^C. Eshelby found that ε^C can be obtained from ε^T by means of a tensor "S", which can be calculated in terms of the inclusion aspect ratio and the Poisson's ratio of the material.

$$\varepsilon^C = S \varepsilon^T \tag{2.9.3}$$

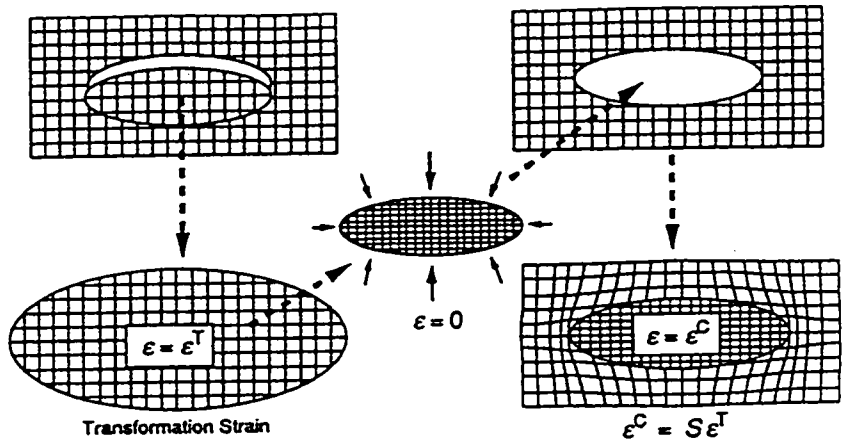

Figure 2.9.2: Eshelby's cutting and welding exercises for the uniform stress-free transformation of an ellipsoidal region [36].

The tensor "S" expresses the relationship between the final constrained inclusion shape and the natural shape mismatch. The inclusion stress can now be evaluated in terms of the stress-free shape misfit by combining equations 2.9.2 and 2.9.3.

Eshelby employed the same method to calculate the misfit strain - differential thermal contraction, where a "ghost inclusion" made up of the matrix material is employed in calculating the matrix stresses and strains. Detailed representation of Eshleby's model is given by Davis and Ward in [36].

Finally, the *matrix stress field* can also be calculated through incorporating another tensor which relates the constrained strain at a point "x" within the matrix to the stress free transformation of the ghost inclusion. Also, although the abovementioned techniques is for a single inclusion, ***non dilute systems*** could be handled through incorporating the volume fraction of the inclusions. In this particular case, a mean stress field, however, yields a lower bound estimate for the strength as shown in Fig. 2.9.3.

Chinghua and Kobayashi [127] attempted to analyze the plastic deformation of the fibre reinforced boron/aluminum metal matrix composites using finite element. The two-dimensional model, however, assumed, rigid fibres.

Brayshaw et al [128] developed closed form expressions for the effective composite properties in the presence of time dependant effects in terms of the properties of the composite phases. However the model is restricted to unidirectional composites.

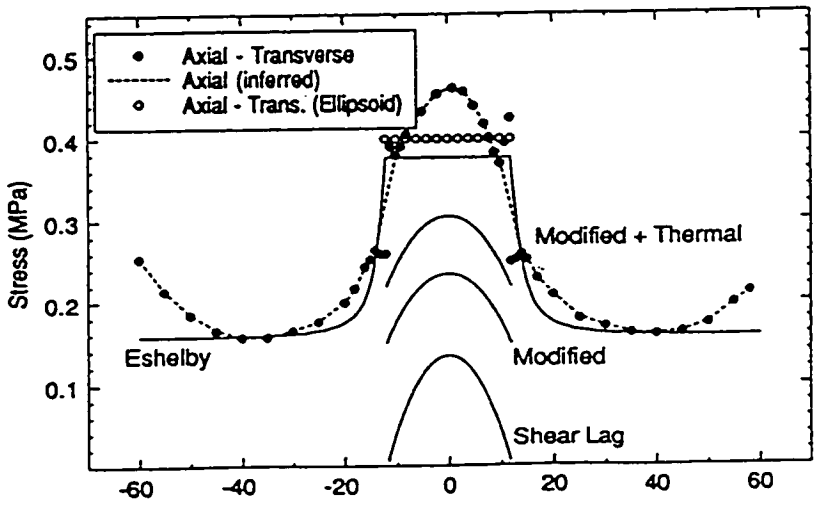

Figure 2.9.3: Predicted and experimental stress variations along the symmetry axes of the composite [36].

2.9.2 Factors Affecting the Strength and Mechanical Behaviour of PMMCs

Influence of Matrix Properties

Both theory and experimental work by Corbin and Wilkinson [32] indicate that the degree of strengthening imparted by the SiC particles increases with the matrix strain hardening rate. However, one should mention that the rate at which strengthening increases with the matrix strain hardening exponent (n) was underestimated in their theoretical predictions. The authors attributed this difference in results to the fact that their model did not include the exact shape of the particles. Instead spherical particles were assumed. The strain hardening properties of the investigated composites were varied by employing different heat treatment operations - which has an effect on the matrix alone. Fig. 2.9.4 illustrates this effect. The various heat treatment operations are described in Table (2.9.1).

Table (2.9.1). Description of the various aging treatments used in the study [32].

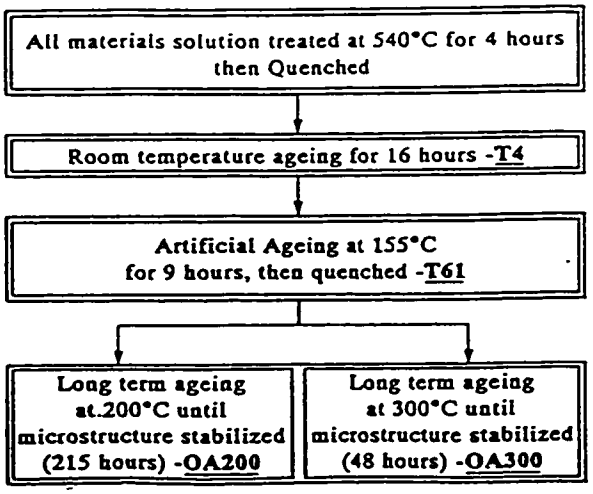

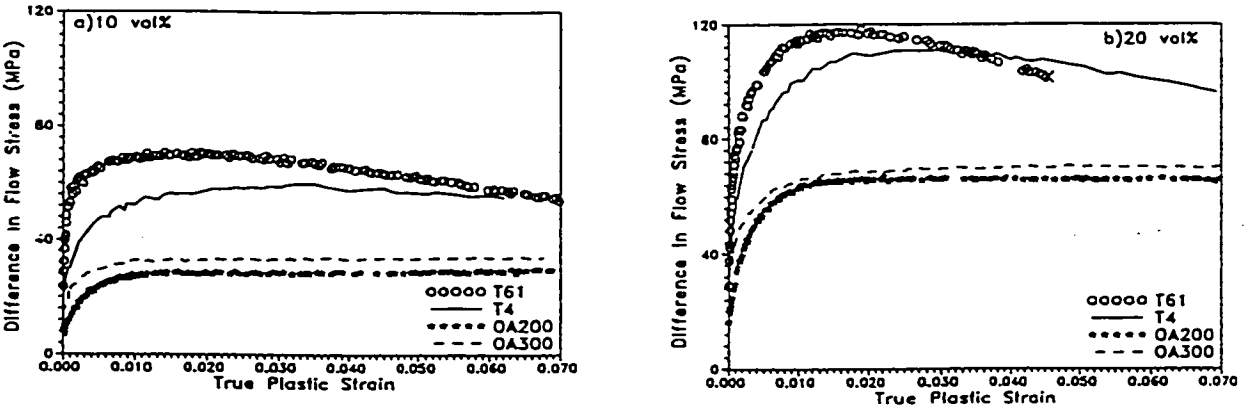

Figure 2.9.4: Difference between the flow stress of the composite and alloy in the various aging conditions; (a) 10% vol. SiC/A356; (b) 20% vol. SiC/A356 [32].

Influence of Particle Shape

Bao et al [37] studied the influence of the particle shape on the strength of PMMCs using the FEM. Their analysis suggests that reinforcement by cylindrical particles provides greater strengthening than do ellipsoidal particles. Therefore, representing the reinforcement phase by spheres will result in an underestimation of the composite flow strength. However, in the model developed by Bao et al [37] the particles were assumed to be perfectly aligned, whereas studies by Wilkinson et al [33,34] indicate that the inhomogeneity in particle distribution has a profound effect on the strength and failure of PMMCs.

Effect of Particle Distribution

Wilkinson et al [33,34,38] extended their analysis of PMMCs, using a self-consistent model based on Eshelby's method, to include the effects of non-uniform particle distribution. This was accomplished by representing the microstructure as a bimodal distribution of particle-rich regions and particle-poor regions. The authors suggest that clustering leads to interactions during the elastic/plastic deformation and can profoundly affect the ductility and strength of a material since the spatial distribution of the reinforcement phase has an effect on the damage accumulation. For instance, the work hardening rate of a clustered composite was found to be higher than of a composite with the same particle volume fraction but uniformly distributed. Moreover, the high volume fraction regime bears a greater portion of the load and is therefore more susceptible to damage. Nevertheless, the predicted strain hardening rates of the various PMMCs were underestimated. The authors attributed the difference between their analytical results and the experimental ones to "damage accumulation" which was not accounted for in their model.

Effect of Particle Size

Nan and Clarke [39] developed a hybrid methodology for calculating the deformation response of PMMCs in terms of an effective medium approach combined with the essential features of dislocation plasticity. The effect of particle size on the PMMCs strength was also incorporated in the model. Nan and Clarke's results, which

are shown in Fig. 2.8.6, indicate that when the particle size is large, i.e. d > 10μm, there is only a slight effect of the particle size on the behaviour of the composite and so continuum plasticity dominates. In contrast, when the particle size is small, i.e. d < 10μm, the dislocation strengthening dominates and the mechanical behaviour is strongly affected by the particle size. In the intermediate particle size range, both mechanisms play a significant role in the deformation response of these metal matrix composites.

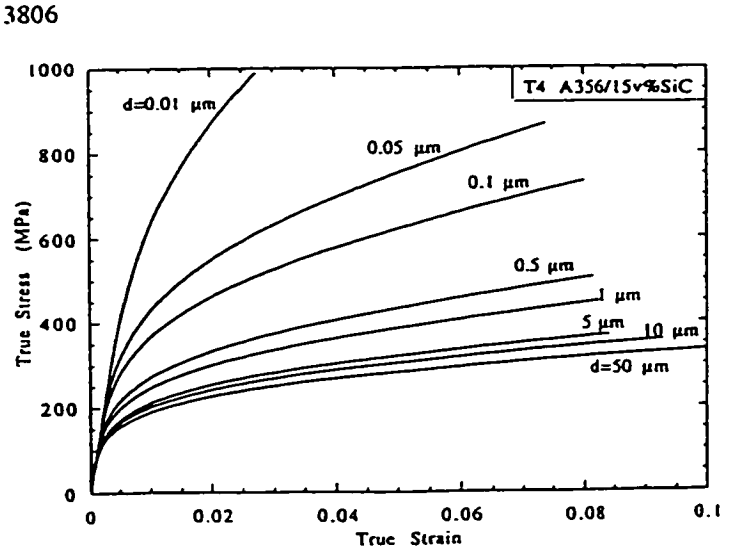

Fig. 2.9.6: Predictions for the effect of different uniform particle sizes on the flow behaviour of the T4 Al-15% vol. SiC composite [39].

2.9.3 Failure Mechanisms of PMMCs

Numerous researchers studied the failure mechanism of PMMCs. Among them are Wilkinson et al [32] who conducted the standard tension and compression test on PMMCs in order to investigate the failure mechanism in each case. Under compressive loads, the results suggest that the composite exhibits essentially the same hardening characteristics as the corresponding matrix material. This could suggest that the composite flow behaviour is dominated by that of the matrix, while the strength enhancement arises from the non-deforming elastic inclusions. Comparison of flow curves, established for the matrix material, showed that the tension and compression curves are essentially equivalent to one another. In contrast, the tensile flow curves for the composites consistently fall below their compressive counterparts. In all tensile tests, fracture is preceded by the formation of a diffuse neck. Beyond necking, the strain becomes more localized. Polished sections through the fractured tensile specimens revealed varying amounts of particle cracking, dependent on the matrix temper and plastic strain. The cracks form primarily in the larger particles, perpendicular to the loading direction. Near the fractured surface, the fraction of cracked particles is somewhat higher, a result of higher local strain. Cracking is believed to be the main source of the tension/compression asymmetry in the flow response. In other words, the volume fraction of the cracked particles is the parameter that governs the flow response of the composite.

Dong and Wu [40] investigated the stress fields and failure mechanisms in PMMCs. According to their experimental analysis, under tensile load, failure always begins in the polar regions of the inclusion. As the load increases, the yielding zone

gradually extends and the matrix in the polar region of the particle gradually debonds from the particles. Voids appear in the polar zones growing along the tensile direction. When the load reaches the yield strength of the material, some deformations in the matrix are evident. Finally, shear yielding forms and the material loses its load carrying capacity.

Similar results, about damage in PMMCs is reported by Caceres and Griffiths [129]. According to their studies of the cracking of Si particles during plastic deformation, the number of cracked particles increases with the applied strain. Similar results were reported by Kiser et al [130]. It was observed by them that, in general, larger and longer particles were more likely to crack. No cracks were observed at the particle matrix interface. The cracks were perpendicular to the macroscopic tensile axis, suggesting that cacking occurs due to the development of tensile stresses. In the coarser structures, broken particles were found on both cell and grain boundaries. In finer structures, cracking initiated on the grain boundaries. As the strain was increased, cracked particles gave place to voids that grew and joined together, forming cracks in the aluminum matrix that eventually became unstable and caused fracture of the sample. The authors also described the particle cracking as a Weibull distributed failure.

Damage Accumulation

In the studies by Kiser et al[130], etching the test samples revealed that the larger particles crack preferentially, as a result of their irregular shape. A damage saturation level of 0.5 may be a result of a bimodal distribution in particle flaw size (a characteristic of larger agglomerated particles). Presumably, at higher stress levels, the

smaller particles would also crack, leading to a further increase in damage. The damage saturation level may also be influenced by "shielding effects". Specifically, the polar regions adjacent to the larger particles are expected to relax following particle cracking. Consequently, smaller particles situated within these regions also undergo relaxation and thus their subsequent probability of failure diminishes. The hardening rate depends sensitively on the rate of damage accumulation, which, in turn, is controlled by the strength characteristics of the particles as well as the flow behaviour of the matrix. Finally, damage accumulation significantly increases with the increase in particulates volume fraction. In addition, the damage rate in the composite depends on the matrix strength.

Effect of Temperature on Damage in PMMCs

Corbin and Wilkinson [35] studied the effect of temperature on the fracture mode of the composite. It was found that, at room temperature, void nucleations determined by cracking of the particulates are followed by tensile failure of the matrix. At higher temperatures, on the other hand, less particulate cracking occurred and the particle/matrix decohesion provided the void nucleation for the ductile failure of the matrix. Also, the strengthening afforded by the particulates varies with temperature as well as matrix temper.

2.9.4 Machining of PMMCs

Machining of PMMCs presents a significant challenge to the industry since a number of reinforcement materials are significantly harder than the commonly used high speed steel (HSS) tools and carbide tools [2]. The reinforcement phase causes

rapid abrasive tool wear; thus the widespread usage of PMMCs is considerably impeded by their poor machinability and high machining costs.

From the available literature on PMMCs it is clear that the morphology, distribution and volume fraction of the reinforcement phase, as well as the matrix properties are all factors that affect the overall cutting process [1,2], but as yet relatively few published reports are related to the optimization of the cutting process. For instance, Monaghan [1] studied the wear mechanism of the carbide tools during machining of 25% SiC/Al PMMCs at speeds lower than 20 m/min. Although the chips appeared to be of the favorable type, the author recommended further research on the subsurface damage.

Tomac et al [7] developed a tool life relation for carbide tools during machining of SiC/Al PMMCs at speeds lower than 100m/min. However, the authors recommended further research on the built-up edge phenomenon that is observed in all tools during machining of SiC/Al PMMCs.

O'Reilly et al [8] ranked various tool materials with respect to tool wear and surface finish; however, their cutting parameters did not exceed 125m/min and 1.0 mm depth of cut, achieved using cubic boron nitride tools. Similar test results were reported by Brun et al [9] who related the tool wear rate, mainly due to abrasion, to the tool hardness. Further, they suggested using lower cutting speeds to reduce the cutting temperature, which accelerates adhesion and diffusion wear and thermally weakens the tool. Since aluminum tends to seize on the tool face and since the grain boundaries are the sites of seizure, the authors further recommended the use of carbide tools with larger grain size.

Winert [10] attributed the wear of the carbide tools to the abrading Al_2O_3 particles that form on the tool surface and rub the tool in the direction of chip flow. However, pulled-out SiC particles could also lead to the same effect since SiC particles are harder than tungsten carbide (WC).

Several researchers [9-27] indicated that PCD (polycrystalline diamond) tools are the only tool material that is capable of providing a useful life during machining of SiC/Al PMMCs. PCD is harder than Al_2O_3 and SiC, and does not have a chemical tendency to chemically react with the workpiece material.

Tomac et al [7] compared the performance of CVD (chemical vapor deposition) inserts to that of TiN, Ti(CN) and Al_2O_3 coated tools. CVD tools offered better overall performance than the other coated tools. Lane et al [20-21] studied the performance of different CVD tools with thin and thick coating films. According to their observations, CVD tools with thin coating films failed catastrophically during end milling of 20%SiC/Al PMMCs. This tool failure was attributed to the spalling of the coating and consequent damage to the relatively soft carbide substrate. The inherent brittleness of the ceramic layer and the increased friction across the tool rake face are the reasons behind spalling. CVD tools with thin coating films cannot take advantage of the tough tungsten carbide substrate since the cobalt present in the binder leads to the graphitization of the diamond during the coating deposition process. On the other hand, CVD tools with thick brazed films showed superior performance. Eventually, the authors recommended carrying further research and development on the brazing alloy to achieve higher wetness and stronger braze joint.

PCD tools with a grain size of 25μm better withstand abrasion wear by micro-cutting than tools with a grain size of 10μm [10,16]. Further increases in the PCD grain size is not beneficial to the tool life, but rather causes significant deterioration in the surface finish. This is because PCD grains with size greater than 25μm are easily pulled out of the cutting edge. Researchers at Duralcan USA [14-25] recommend using PCD tools in turning Al 356/20%SiCp composites at speeds up to 600m/min. For good results, honing of the cutting edge is recommended.

The matrix alloy and heat treatment condition affect the machinability of the composite profoundly [2]. Hypereutectic aluminum alloys (A359) contain more silicon than the hypoeutectic alloys. Hence, composites of the latter alloys are found to be less abrasive than those based on wrought alloys [16,21]. Thus, the authors recommended machining aluminum foundry PMMCs in the solutionized condition rather than in the T-4 or T-6 heat treatment conditions. To overcome the problem of dimensional instability incurred during the tempering process, the authors recommended rough machining in the untreated condition, age the part and then carry out the finishing process.

The reinforcement phase and size determine how easily the particle is sheared by the cutting edge. The ease of shearing the particle is inversely proportional to the aspect ratio of the reinforcement phase. Small round particles or blocky ones are the most difficult to machine (shear), platelets are less difficult and whiskers are the easiest of all [2,16].

As for the effect of the cutting parameters on the tool life, Lane et al [13-17,19-21] attributed the increase in wear by abrasion of PCD tools to the increase in kinetic

energy gained by the abrading SiC particles. On the other hand, Brun et al [9] attributed the increase in tool wear to the thermal degradation of the tool material. Tomac et al [7] attributed the narrow grooves formed on the tool rake face to the ploughing effect produced by the SiC particles.

Tool wear was found to be inversely proportional to the feed rate [11]. Tomac et al [7] attributed the increase in tool life at higher feed rates to the thermal softening of the composite. The authors suggest that the workpiece material becomes softer and the SiC particles are pressed into the workpiece, causing less abrasion on the tool itself. On the other hand, Finn et al [26] and Morin et al [27] attributed the reduction in tool wear with faster feed rates to the reduced contact between the cutting edge and the abrasive SiC particles.

Finally, although the application/type of coolant has a tremendous effect on the cutting process, little research has been devoted to this aspect. Particulate reinforced composites have all the characteristics of materials that form a built up edge [7,8,11,16]. In the case of an abrasive material, such as Al/SiC particulate composites, a beneficial stable built-up edge can actually protect the cutting edge and reduce its wear by 80% [16]. However, at higher speeds or upon using a coolant the built-up edge is not stable. That is to say, the built-up edge could be detached and smeared along the path of the cutting tool, causing tool surface damage and poor workpiece finish. As for the application of a coolant, researchers at Duralcan USA [13-17, 19-25] recommend investigating the possibility of dry rough machining in order to take advantage of the "protective built-up edge" phenomenon.

Residual Stresses in Machined PMMCs

Despite the fact that machining causes subsurface damage in the workpiece [3-6], which has notable implications with regrad to the parts performance, so far, no research has been carried out to determine the effect of the cutting parameters on the PMMCs workpiece surface integrity. Oden et al [28], however, studied the near surface deformation in an aluminum-silicon carbide whisker composite due to grinding. Other researchers [1,7,8,10,11,29,30] limited their studies to relating the effect of the machining cutting parameters and tool wear to the produced workpiece surface roughness, which could be misleading. This is because, in most cases, during machining of Al/SiC PMMCs the produced surface roughness, Ra, is much lower than that obtained during machining of the matrix alloy alone. O'Reilly et al [8] attributed the improved surface finish to the burnishing or honing effect produced by the action of small SiC particles trapped between the flank face of the tool and the surface of the workpiece. Most researchers, nonetheless, recommended investigating the effect of the cutting parameters on the subsurface deformation produced due to high stresses and temperatures generated during cutting as well as the chip formation mechanism.

Perhaps the most in depth study on residual stresses in machined composites was carried out by Oden et al [28] who used X-ray diffractometry to view the deformation in the near-machined surface. X-ray diffractometry data revealed that the deformation, in the form of micro-cracks, dislocations and lateral grain boundary cracks, was highly localized in the very top surface zone. The depth of this layer is dependent on the severity of the machining process.

Ahn et al [131] combined Vicker's indentation hardness measurements with fracture mechanics to estimate the residual stresses in machined and annealed ceramics. However, the absence of a detailed model for indentation crack systems and the existence of steep residual stress gradients near the machined surface made the indentation technique attempt unsuccessful in relating them more closely with the residual stress values determined using X-ray diffraction methods.

It's probably worth mentioning that a unique "best way" for measuring the residual stresses in multi-phase materials is still disputed among researchers. Thus, the literature includes several attempts or methods to measure the residual stresses in these materials. Among these attempts is one by P.K. Wright [132] who employed X-ray diffraction and neutron diffraction, where the latter yielded results that are closer to the analytical values. Results by Todd et al [133] and Arsenault et al [134] agree with this trend. On the other hand, Cerretti et al [135] recommended X-ray diffraction over neutron diffraction techniques. Liu et al [136] recommend X-ray diffraction as well.

Levy et al [137] and Ho et al [138] developed finite element models to estimate the residual stresses in particulate metal matrix composites. Nevertheless, neither of these researchers compared their analytical results to measured ones.

Brayshaw et al [128] developed a closed form solution for the composite residual stresses which includes time dependent effects in terms of the composite phases. However, the model is limited to unidirectional composites.

2.9 Summary

After carrying out a literature review on machining of particulate metal matrix composites one can come up with the following conclusions:

A great deal of attention has been recently devoted to understanding the strengthening mechanisms in metal matrix composites, which are distinguished by a large particulate volume fraction and relatively large diameter. This class of composite materials lies between: 1. the dispersion hardened composites, where the strengthening comes from the particles that act as obstacles to dislocations movement (the load transfer to the particles provides only a small strengthening increment). 2. Continuous fibers or whiskers, where load transfer to the particles is the primary strengthening mechanism. PMMCs lie between these two categories, and hence the strengthening mechanism is less clear. Therefore, probably a hybrid model, such as that developed by Nan and Clarke [39], would be the best to describe the behaviour of composites in which the diameter of the reinforcing particles exceeds that of the dispersion hardening case, but is less than the length scales associated with the movement of dislocations.

Another important issue in understanding and modeling the strength of PMMCs is to consider the effect of particle shape, size and clustering. Heat treatment, on the other hand, affects the matrix properties and hence the strain hardening of the composite, in general. Finally, almost all researchers agree on the failure mechanisms of this class of composites. At room temperature, particles crack in a direction perpendicular to the tensile load direction; voids form at the crack and eventually they link up. The cracked particles then fail to carry the load, very excessive deformation occurs in the matrix material which ultimately leads to fracture. On the other hand, at

higher temperatures decohesion between particles and matrix develops and voids are initiated at these areas.

The strengthening mechanism in PMMCs affects their machinability. So far, little published work is related to improving the machinability of this class of materials. Polycrystalline diamond tools appear to be the only tool material that could be used to machine Al/SiC PMMCs with a reasonable tool life. Although all researchers recommended further research on the effect of machining on subsurface damage in the workpiece, all the research, so far, to the best of knowledge of the author, is limited to surface finish of the machined part. Tool wear mechanisms encountered during machining of these composites is also not fully understood. In-depth analysis of the chip formation mechanism during machining PMMCs has not been attempted yet.

Finally, the finite element method appears to be an efficient tool to model the metal cutting process.

Objectives of the presented research

The literature review indicates that the cutting parameters profoundly affect the tool wear and tool life, and hence the economics of the cutting process. Therefore, the cutting parameters that yield the optimum cutting parameters are of a prime importance. These optimum cutting parameters are the ones that yield the maximum tool life with acceptable surface and subsurface characteristics.

In order to achieve the abovementioned objectives two finite element models are to be formulated. The first model is for the tool. From the tool model, the tool temperature and stress profiles, and hence the tool wear modes, could be determined for various cutting conditions. The second model is for the machined workpiece. The stresses induced in the part during machining as well as the residual stress after machining are to be predicted by the model for different cutting conditions. Both models are three-dimensional in order to accurately reflect the cutting process. Thermal and mechanical loads are coupled in the models. The results of the two models are to be validated experimentally.

Combining the results of the two models should help predict the optimum cutting parameters for turning PMMCs, which currently presents a great challenge to industry.

CHAPTER 3

EXPERIMENTAL PROCEDURES

3.1 Workpiece Material

The machining investigations were carried out using Duralcan F3S.20S Al/SiC metal matrix composites. The SiC particles had an average diameter of 12μm. Fig. 3.1.1 shows the microstructure of the test material. Table (3.1) shows relevant physical and mechanical properties of A356-20%SiC particulate metal matrix composites at T-71 condition. Prior to carrying out the cutting experiments the test material was fully heat treated to the T71 condition, where the material was solution treated at 540°C for 4 hours, then quenched and aged for 16 hours at room temperature. The material was then artificially aged at 155°C for 9 hours and then quenched. The test material was in the form of bars 177.8 mm in diameter and 305 mm in length.

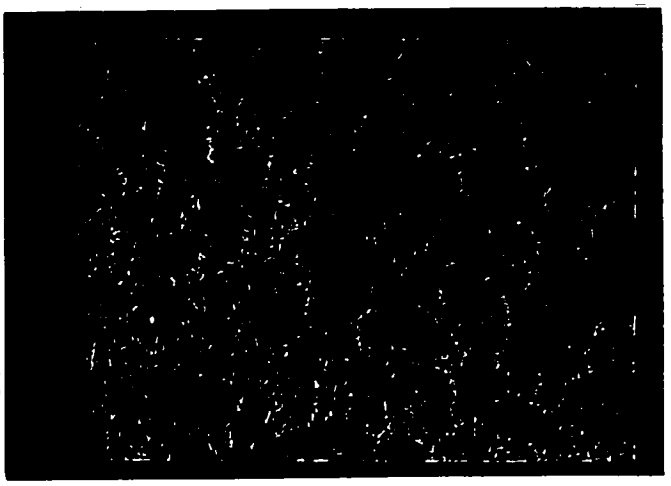

Figure 3.1.1:
Workpiece microstructure

Table (3.1). Typical Physical and Mechanical Properties of Duralcan F3S.20S – T71 condition [22].

Property	
Density (g/cm^3)	2.77
Thermal conductivity (J/(s.m.^oC)) at 22 ^oC	0.0196
Specific Heat (J/(g .^oC))	
100 ^oC	0.9127
200 ^oC	1.0006
300 ^oC	1.0843
Average coefficient of thermal expansion (mm/mm/^oC)	x10^{-6}
50-100 ^oC	17.5
50-300 ^oC	21.1
50-500 ^oC	21.4
Ultimate Strength (MPa)	262
Yield Strength (MPa)	21.4
Elongation (%)	1.9
Modulus of Elasticity (GPa)	98.6
Rockwell Hardness (B)	67 +/- 1.5

3.2 Cutting Tools

Various tool materials (coated carbide, Al_2O_3/TiC and Polycrystalline diamond PCD) were employed in the study. Oblique turning tests were carried out and different cutting parameters were employed for each tool material. However, for the purpose of comparing tool wear all cutting tests were carried out at a fixed volume of metal removed (300 mm^3). Table (3.2) summarizes the cutting tools data.

Table (3.2). Cutting Tools Material and Geometry

Tool	Geometry
PCD (tipped – 80° rhomboid)	PCD thickness: 25μm, 50μm PCD grain size: 10μm, 25μm, 50μm Rake angle, α : -5°, 0°, 5° Clearance angle : 7° Approach angle: 5° Tool nose radius, r : 0.8mm , 1.6mm
TiN coated carbide (triangular)	TiN thickness: 25μm Rake angle, α : 0° Clearance angle : 7° Approach angle: 5° Tool nose radius, r : 1.6mm
Al_2O_3 ceramic (triangular)	Rake angle, α : 0° Clearance angle : 7° Approach angle: 5° Tool nose radius, r : 1.6mm

3.3 Design of Experiments

In order to ensure the accuracy of the experimental readings of the cutting forces, tool wear and cutting temperatures, which are to be later considered in the analytical models, the experiments were conducted according to the following procedure: First, each experiment was repeated several times. Replication increases the precision by reducing the standard error. Second, the sequence of the experiments was randomized in order to eliminate bias and ensure independence among the observations. A completely randomized design (CRD) of experiments was adopted since its statistical analysis is relatively simple and it provides maximum degrees of freedom for error [139]. The precision of CRDs is best if the units are grouped into homogeneous blocks and the treatments are equally replicated.

To begin with, the data collected for "p" treatments, for example cutting speeds v_1 to v_p, each replicated "r" times (i.e. r observations) is arranged as shown in Table (3.4). The sample size is determined based on a set confidence level of 95% for the interval and a set maximum error of estimation, sometimes referred to as error bound "B". The sample size determined to estimate the mean to within a bound "B" is given as:

$$r = [Z_{\alpha/2}\, \sigma / B]^2 \qquad (3.3.1)$$

where, $Z_{\alpha/2}$ is equal to 1.96 for 95% confidence [140]. The error bound "B" was chosen to be equal to the accuracy of the measuring device.

Table (3.4) Data Table for CRD with Equal Number

Treatment					
	1	**2**	**3**	**....**	**p**
	y_{11}	y_{21}	.....		y_{p1}
	y_{12}	y_{22}			y_{p2}
	...				
	y_{1r}	y_{2r}	...		y_{pr}
Sum	y_1	y_2			y_p
Mean	$\bar{y}_1$	$\bar{y}_2$			$\bar{y}_p$

Where,

y_{ij} = yield of the j-th unit in the i-th treatment,

$y_i = \sum_j y_{ij}$ = total of yields for the i-th treatment

$\bar{y}_i = y_i / r$ = mean of the i-th treatment

The collected data is further analysed as shown in Table (3.5).

Where,

$$SSTot = \sum_i \sum_j y_{ij}^2 - C$$

$$C = y^2 / rp$$

$$SST = 1/r \sum_i y_i^2 - C$$

$$SSE = SSTot - SST$$

$$MST = SST / (p-1)$$

$$MSE = SSE/(p(r-1))$$

Table (3.5) ANOVA for CRD [139]

Source of Variation	Degrees of Freedom	Sum of Squares	Mean Square	F_T
Total	$rp-1$	SSTot		
Treatments	$p-1$	SST	MST	F_T
Error	$p(r-1)$	SSE	MSE	

Where $MSE = s^2$, which is an unbiased estimate of σ^2, the variance associated with the experiment units.

The sample standard error of $\bar{y}_i$ is given as:

$$s_y = (MSE/r)^{1/2} \qquad (3.3.2)$$

The sample standard deviation is then compared to the assumed one from equation (3.3.1) and the sample size is corrected accordingly.

Finally, $F_T = MST/MSE$. F_T is a test through which the means are compared at certain confidence level $(1-\alpha)$.

3.4. Cutting Tests

The cutting tests were carried out on a 10HP Standard Modern NC lathe. The cutting was performed dry, i.e. without using any cutting fluid. Different cutting parameters (speed, feed rate and depth of cut) were employed. Table (3.6) summarizes the cutting parameters. All the cutting tests were oblique turning.

Table (3.6). Cutting Parameters

Tool	Cutting parameters
PCD	Cutting speed : 670 m/min 894m/min Feed rate: 0.15mm/rev. 0.25 mm/rev. 0.35 mm/rev. 0.45 mm/rev Depth of cut: 1.5mm 2.5 mm
TiN coated carbide and Al_2O_3 ceramic tool	Cutting speed : 150m/min 248m/min Feed rate: 0.15mm/rev. 0.25 mm/rev. 0.30 mm/rev. Depth of cut: 0.25 mm 0.5mm 0.75 mm

During all cutting tests, the three components of the cutting forces (tangential force, feed force and thrust force) were measured using Kistler 3-component piezo-electric transducer type dynamometer. To avoid excessive charge leakage, maximum charge amplifier input impedence was employed and high insulation resistance of the load washer was provided. An externally applied force on the piezo-electric crystals causes a displacement of the ions in the crystal, which in turn leads to a change in the length of the electric dipole. The dynamometer is designed such that compressive forces on the crystal result in an excess charge density at the ends of the crystal. The dynamometer responds proportionally to the three cutting forces. The produced charges (signals) are fed to three channels of an Analog to Digital converter after being amplified. A hardware low-pass filter was employed in the setup to smooth the signal. Fig. 3.4.1 shows the experimental set up.

The measurement sampling rate was selected such that it is greater than 4 times the maximum operating frequency of the machine tool in order to avoid signal aliasing. Global lab III software was used for the data acquisition. Prior to conducting each set of cutting tests, the dynamometer calibration was verified.

In some of the cutting tests the tool temperature was measured using K-type thermocouples that were glued onto the tool rake face. The thermocouples were positioned 1 mm away from the cutting edge.

The reliability of the force and temperature measurements was constantly checked by repeating the experiments. The results of each set of experiments were accepted if they exhibited an error less than 5%.

Each cutting test was performed using a new cutting tool tip. At the end of each cutting test samples of the produced chips were collected, tool wear examined as well as the produced workpiece. The following sections summarize the analyses carried out on the chips, tools and workpiece.

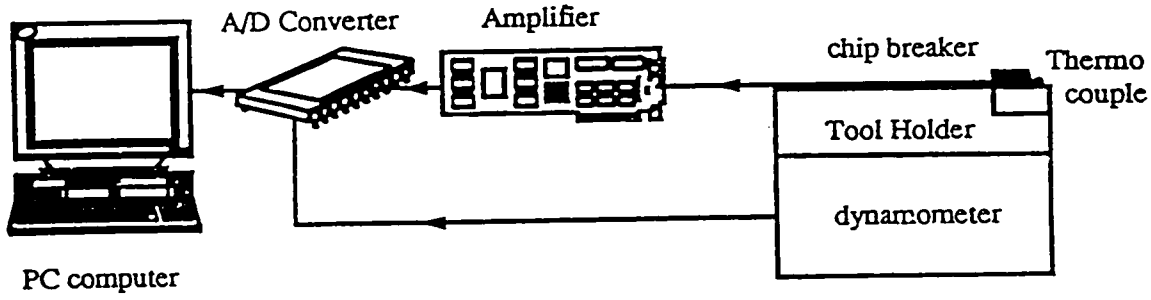

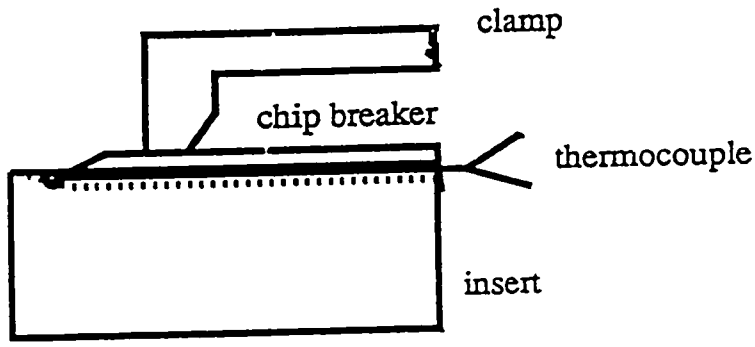

Figure 3.4.1: The experimental set-up

3.4.1. Examination of the Cutting Tools

At the end of each cutting test the tool wear was examined using optical and scanning microscopes. The tools flank wear (V_B) was measured using a tool makers microscope, where for each measurement of tool flank wear, the average of ten readings was taken

The adhering workpiece on the tool flank and rake faces was first analyzed using X-ray dispersion technique and then removed by soaking the tool in NaOH for one hour. The PH of the tool was then normalized using HCl and water. The tools were finally cleaned using acetone.

The tool/chip contact length was determined from photographs of the tool rake face using optical microscope. The average of ten readings was taken. Fig. 3.4.2 illustrates the measurement of the chip/tool contact length. The cutting tool is made of Al_2O_3. The tool shown in Fig. 3.4.2 was used in turning A356 20% SiC particulate metal matrix composites at a cutting speed of 150m/min, feed rate of 0.25mm/rev. and depth of cut 0.5mm.

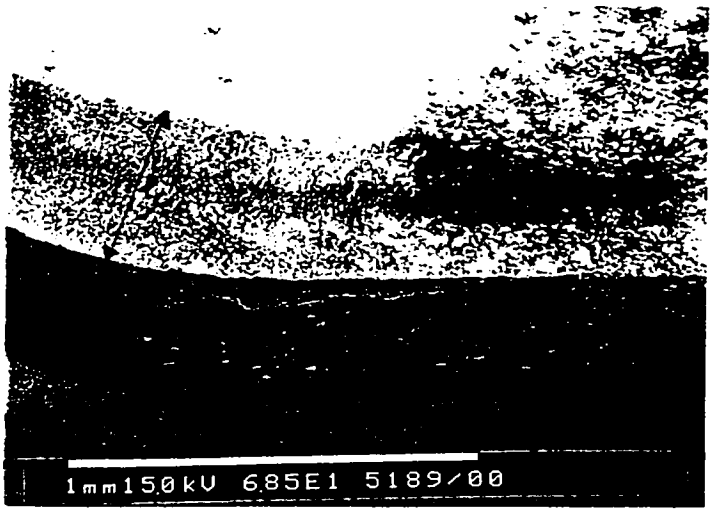

Figure 3.4.2: Measurement of the Tool/Chip Contact length.

3.4.2 Examination of the Produced Chips

At the end of each cutting test samples of the produced chips were collected for further examination. The chip morphology can give clues with regard to the shearing process as well as explain the tool wear mechanism.

Chip thickness

The thickness of the produced chips was measured using a tool makers microscope. The average of 10 readings was taken. The chips were leveled using a plasticide mounting.

Shear plane angle

Predicting the shear plane angle "ϕ" has occupied the attention of many investigators. The literature includes several attempts to calculate the shear angle under orthogonal cutting conditions; relatively few publications pertain to the determination of the shear angle(s) under oblique cutting conditions. Merchant [64] predicted the shear angle to be:

$$\phi = \pi/4 + \alpha/2 - \beta/2 \qquad (3.4.1)$$

where, α is the tool rake angle and β is the friction angle between the chip and the tool rake face.

This model, however, fails to predict the ϕ accurately. Lee and Shaffer [66,67] applied the slip line theory, which yielded poor results as well. Wright in [142]

presented the following scheme that was followed in this thesis. This particular method was selected as it provided a good agreement with experimental measurements.

According to Wright's theory, in the primary shear zone the rate of work done in a discrete parallel-sided shear zone "W_p" is given as:

$$W_p = K \,.\, u_p \,.\, s_p \tag{3.4.2}$$

where,

K is the general shear strength of the material

u_p is the shear velocity on the primary shear plane

s_p is the length of the shear zone.

$$W_p = K\,[(\cos\alpha / \cos(\phi - \alpha)) \,.\, w_o\, t_o / \sin\phi] \tag{3.4.3}$$

where, w_o is the depth of cut and t_o is the undeformed chip thickness (feed rate)

The general method for predicting the shear angle thus relies on calculating the lowest plastic work rate for initiating the shear instability in severely work hardened material K_1, and then assuming that the system will continue to operate at this work rate while shearing the softer material K_o, along the longer shear plane ϕ_o, where K_1 and K_o are the workpiece shear yield strength and shear strength corresponding to (ultimate strength in tension / $\sqrt{3}$).

Therefore equating the rate of work done in both zones (at ϕ_1 and ϕ_o), shown in Fig. 3.4.3, the shear zone angle could be determined as:

$$\cos(\phi_o - \alpha) = K_o/K_1\,[\cos(45-\alpha/2) \,.\, (\sin 45 + \alpha/2)] \tag{3.4.4}$$

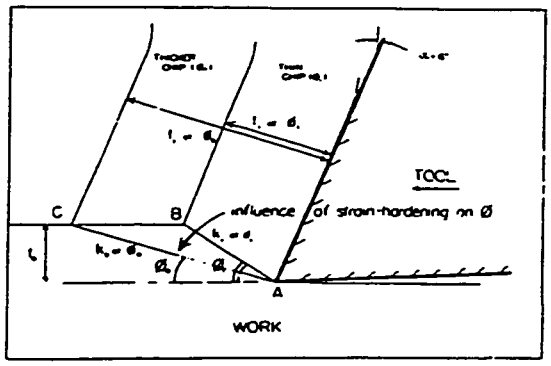

Figure 3.4.3: Diagrammatic illustration
of the shear zone angles [142]

Scanning electron microscope (SEM) and optical microscope examination of the chips

Transverse cross-sections of the chips were mounted in transparent moulds. The chip samples were then polished and etched using a solution of: 2.5ml HNO_3, 1.0 ml HCl, 1.5 ml HF and 95 ml H_2O. Etching was carried out to reveal the type of deformation in the chips. An optical microscope was used for viewing the deformation bands in the chips. Deformation in the chips was also viewed using SEM.

3.4.3 Examination of the Machined Workpiece

Surface roughness measurements

The surface profile traces of the machined workpieces were obtained using the Talysurf roughness tester. The device consists of a stylus stand, profile recorder and a measuring instrument that operates as follows: The stylus is allowed to slide on the machined surface. A motor and a gearbox, which control the speed of the stylus, provide the movement of the stylus. The stylus itself is mounted on an arm that is pointing at the contact limit of an "E-shaped" iron head. The outer limbs of the iron head have two induction coils. A small gap exists between the arm and the outer limbs of the head. Upon the movement of the stylus (as a result of changes in the surface topography) the air gap in the coils changes, and consequently the displacement of the stylus is recorded as proportional to the impedance of the coils (which is proportional to the air gap).

R_{max} roughness was chosen, rather than R_a (average) roughness because the latter could give misleading results of the surfaces that include fine cracks, which could have serious implications with regards to the fatigue life of the machined part.

TEM, SEM and Optical microscope examination of the workpiece

The machined workpieces were first cut into small parts (5 cm thick) using water jet machining. Using water jet machining the depth of the damaged layer that may be induced by water jet is small compared to the depths of cut and feed rates employed in

the present study. Furthermore, the cut pieces were divided into smaller specimens (1 cm thick) using a diamond saw at very low speeds and under flood cooling. The specimens were then placed in moulds to facilitate their handling. The specimens were then polished using a rotary polishing table with soft pads that were impregnated with fine diamond paste (1μm). The deformation in the machined workpiece cross-sections was viewed using scanning electron microscope as well as an optical microscope.

Transmission electron microscope (TEM) was used to view the deformation in the matrix material at high resolutions. Each sample was cut into two pieces that were glued together with the machined surfaces facing each other. The preparation of the specimens for the TEM examination involved diamond grinding, starting with 6μm diamond paste and ending with 1μm diamond paste on a soft cloth. The specimens were then etched by ion beam sputtering.

Estimation of the machined workpiece residual stresses using Vicker's microhardness measurements

Vicker's microhardness measurement tests were conducted using 50 grams weight. A small weight was selected because of the presence of hard particles in the relatively soft aluminum matrix. The domain of the measurements was 5 mm diameter circle, on which ten equally spaced measuring points were allocated, their hardness average being taken to represent the hardness of a particular specimen. The tests were carried out on polished cross-section samples of the workpiece. The measurements started at 10 μm below the machined surface and continued inwards. Both the hardness and the distance from the machined surface were recorded for each data point. The

microhardness-depth profiles were utilized to estimate the depth to which the plastic zone extends beneath the machined surface.

CHAPTER 4

NUMERICAL MODELS

4.1 Finite Element Models

In metal cutting, failure of the cutting tool leads to deterioration of the workpiece surface, loss of dimensional tolerances and other catastrophic consequences such as increasing the machining down time to change and set the tools. Thus, predicting the tool stresses and temperatures, and hence wear and failure mode, is highly desirable. Similarly, predicting the stresses developed in the workpiece could help predict the strength properties and performance of the part. Measurement techniques for the temperatures and stresses generated in the cutting tool can give, at best, average results. Hence, numerical methods, such as the FEM, offer a more promising approach.

4.1.1. Cutting Tool Model

A 3-D model of the tool was formulated using the solid modeler of the commercial software I-DEAS [143]. Loads and boundary conditions were applied on the solid model surfaces and edges. Relating the boundary conditions to the solid model attributes facilitates remeshing the model in case of minor tool geometry changes. Fig. 4.1.1 shows the solid model for the tool with the boundary conditions.

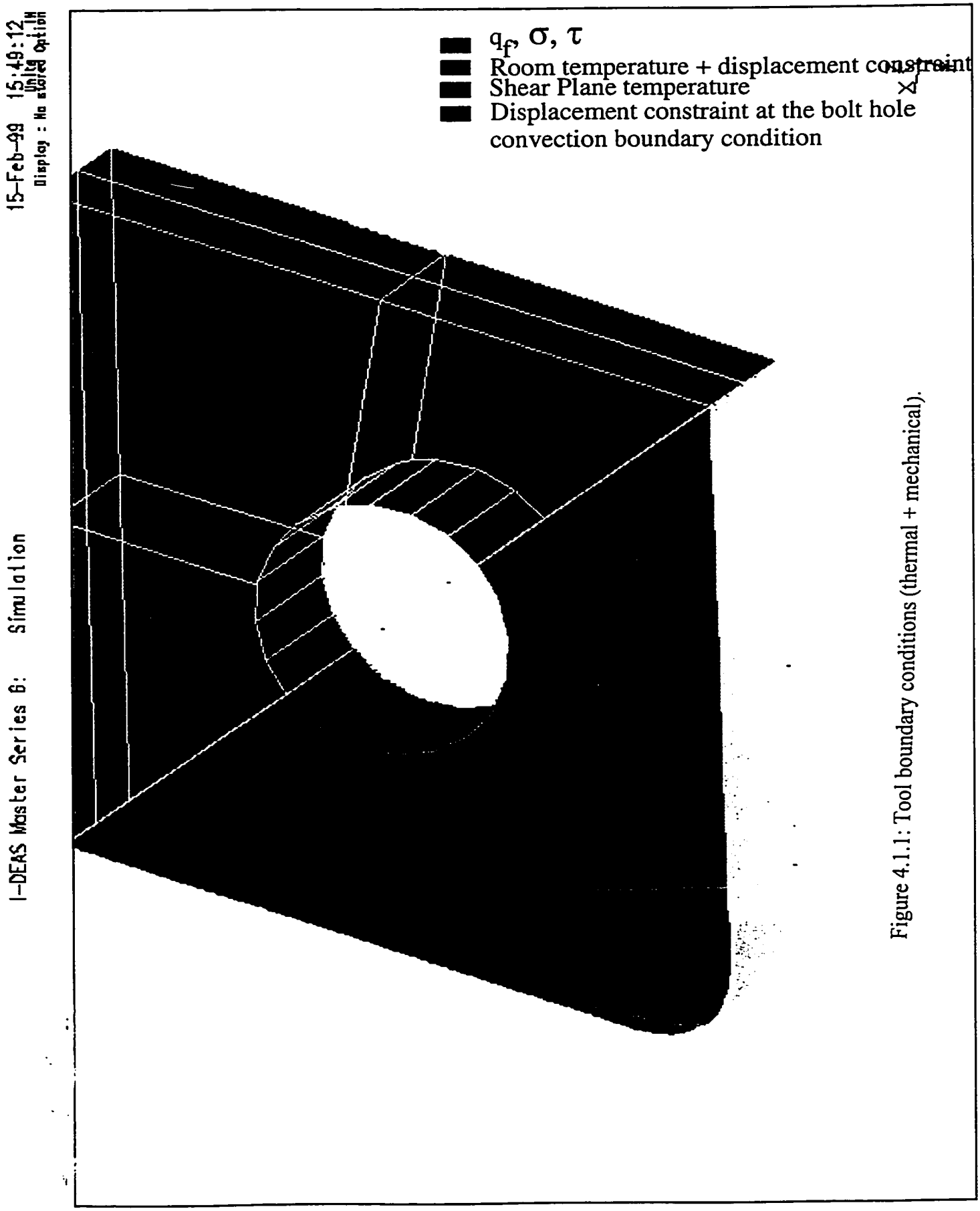

Figure 4.1.1: Tool boundary conditions (thermal + mechanical).

Thermal Loading

The cutting edge is exposed to three heat sources. The first heat source is the heat generated over the tool/chip contact length due to friction (q_f), where

$$q_f = P_f / A_{ct} \qquad \text{.....(4.1.1)}$$

where,

P_f : the energy dissipated due to friction,

A_{ct} : the tool/chip contact area,

The energy dissipated due to friction is equal to:

$$P_f = F_c \cdot \mu \cdot v \qquad \text{.....(4.1.2)}$$

where,

F_c: is the cutting force,

μ: the coefficient of friction between the tool and the chip,

and v: the chip velocity.

The cutting force was evaluated using Koenigsberger's equation [82] , where

$$F_c = K_s \cdot A_c \qquad \text{.....(4.1.3)}$$

where,

K_s: the specific cutting force

A_c: the chip's cross sectional area (=depth of cut (d) x Feed rate (f))

The actual tool/chip contact area, A_{ct}, used in equation (4.1.1), was assumed to be proportional to the chip thickness, as follows [64,70,77]:

$$A_{ct} = a \cdot f \qquad \text{.....(4.1.4)}$$

where,

a: constant of proportionality relating the tool/chip contact length to the chip thickness

The chip velocity (v) is equal to :

$$v = r \cdot v_c \qquad \text{.....(4.1.5)}$$

where,

r: the chip ratio

v_c: cutting speed

The second heat source is due to the chip shearing. The energy liberated due to the chip shearing , P_s, is equal to:

$$P_s = F_s \cdot v_s \qquad \text{.....(4.1.6)}$$

where,

F_s: the shearing force

v_s: the chip velocity at the shear plane

Using Merchant's cutting forces diagram [65,70], Fs is equal to:

$$F_s = F_c \cdot \cos \phi \qquad \text{.....(4.1.7)}$$

where,

ϕ: the shear angle

The energy generated at the shear plane is divided into 3 parts. The first part is carried away by the chip. Most researchers [65-77] agree that the portion of heat carried away by the chip is approximately equal to 80% of the total heat generated at the shear

plane. Another part of the heat generated at the shear plane is conducted back to the workpiece. Weiner's relations [68] were employed in the calculation of the portion of heat conducted back to the workpiece. Weiner's relations take into consideration the shear angle as well as the workpiece thermal number.

Thus, the shear plane temperature, T_S, is evaluated as follows:

$$T_S = (1-\lambda)\, P_{S2} / (\rho\, c\, .\, v_S\, .\, A_C) \qquad \text{.....(4.1.8)}$$

where,

$$P_{S2} = 0.2\, P_S \qquad \text{.....(4.1.9)}$$

$\rho\, c$: volumetric specific heat

and λ: portion of the heat source conducted back to the workpiece

If the tool has some flank wear, a third heat source results from the friction between the tool flank face and the workpiece. The heat flux on the flank face, q_l, can thus be expressed as:

$$q_l = R.\, v_f\, .\, \mu\, F_h / A_l \qquad \text{.....(4.1.10)}$$

where,

R: the ratio of the tool thermal conductivity to the workpiece thermal conductivity

v_f: velocity along the flank face

F_h: thrust force

A_l: area of the tool's flank wear

μ: coefficient of friction

The boundary conditions at areas other than the tool/chip contact area were modeled as follows:

1. convection boundaries at the flank and rake surfaces
2. room temperature is reached way from the cutting tool tip, i.e. at the tool shank.

Mechanical Loading

The three components of the cutting forces were taken into consideration in the finite element model. Wright's stress model [79,142] was employed in the distribution of the shear and normal forces. Sufficient displacement constraints were prescribed at the tool shank to prevent rigid body motion. Nodes at the bolt hole were also fixed as shown in Fig. 4.1.1.

Meshing the tool model

The model was meshed using mainly brick elements (Fig. 4.1.2) and few tetrahedral elements (Fig. 4.1.3). Fig. 4.1.4 shows an example of a meshed cutting tool.

The mesh is refined towards the cutting edge, where the mesh size depends on the elements' strain energy. The element strain energy is basically the elastic energy stored in the structural element. Strain energy, calculated by the finite element analysis, provides a measure of the distribution of deformation within the analysed part. A uniform strain field is indicative of an optimally designed part, whereas high and low strain energy concentrations can represent under and over-designed portions of the model, respectively.

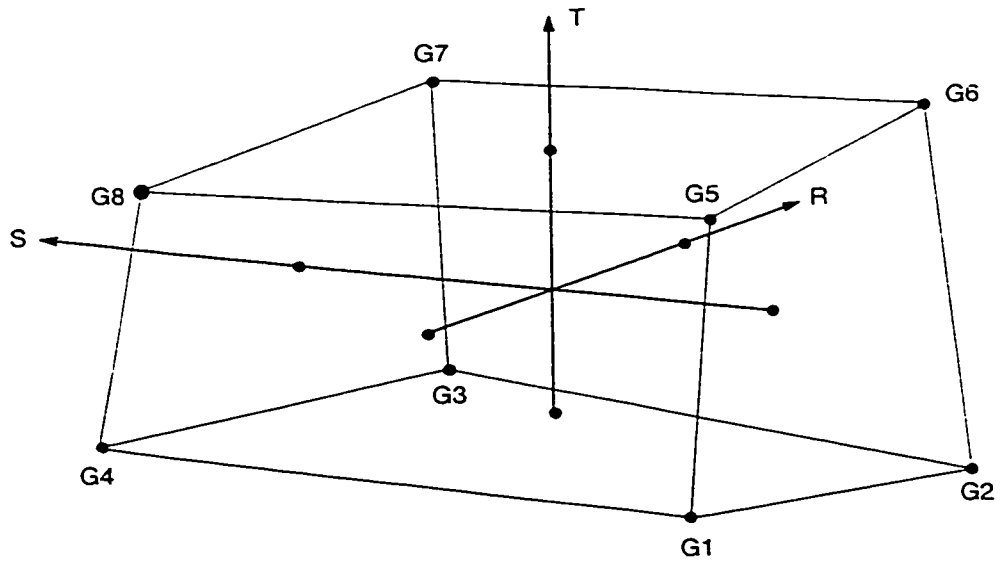

Figure 4.1.2: 8-noded brick element (CHEXA) [144].

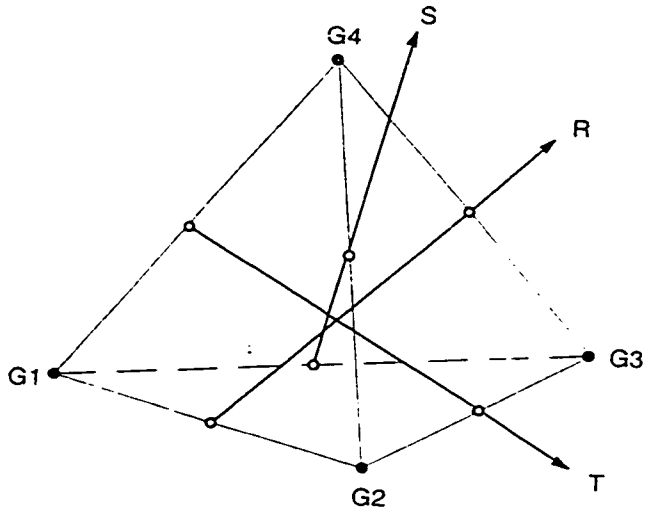

Figure 4.1.3: 4 noded tetrahedral element [144].

Figure (4.1.4) Meshed Tool

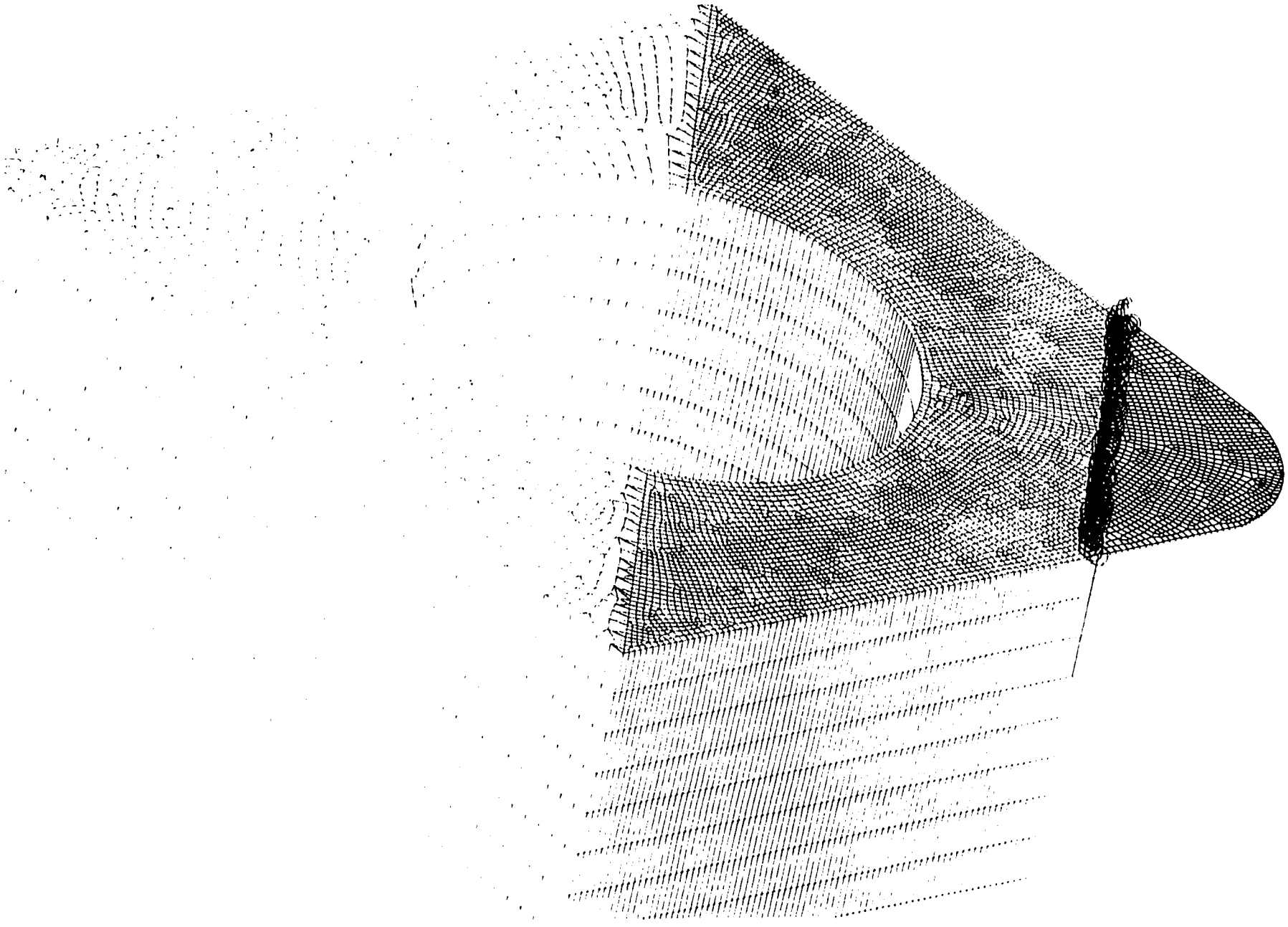

Dissimilar meshes (coarse and fine) were connected using spline elements. In a spline element, the displacements are interpolated using equations for elastic beam element passing through the grid points [143]. Table (4.1) shows the format of the spline element.

Analysis was carried out using the commercial software NASTRAN [144]. The analysis process was divided into two stages: thermal and mechanical. The output from the thermal analysis was nodal temperatures, which were taken as an input in the mechanical analysis stage.

Table (4.1). Rspline element [144].

1	2	3	4	5	6	7	8	9	10
RSPLINE	EID	D/L	G1	G2	C2	G3	C3	G4	
	C4	G5	C5	G6	-etc.-				

Example:

RSPLINE	73	.05	27	28	123456	29		30	
	123	75	123	71					

Loads were applied using rigid elements (RBE2) [144], which defines a rigid body with independent degrees of freedom that are specified at a single grid point and with dependent degrees of freedom that are specified at arbitrary number of grid points. Displacement constraints were applied using constrained element (RBE3) [144].

4.1.2 Workpiece Model

A solid model of a machined workpiece has been constructed using I-DEAS master series 6 [143]. Equations (4.1.1. – 4.1.10) have been employed to calculate the workpiece's share of thermal load. Cutting loads and friction loads were also applied to the cutting plane and the chip, respectively.

The solid model of the workpiece was meshed using squared brick elements. The finite element formulation of the brick elements is given in Appendix (A). Each element was 20μm on each side. Temperature dependant material properties were employed for the reinforcement phase and the matrix material. Thermal loads solution is obtained first, followed by the solution of mechanical loading. Fig. 4.2.1 shows a part of the workpiece mesh (the fine part near the cutting zone), while Fig. 4.2.2 is a magnification of Fig. 4.2.1. Fig. 4.2.2 illustrates the different phases. Coarser mesh was employed away from the cutting zone. Sufficient displacement constraints were employed far from the cutting zone to prevent rigid body motion.

4.2 Finite Element Formulation

The analysis of heat transfer in a solid continuum can be reduced by finite element techniques to the solution of a set of equilibrium equations in which the unknowns are defined at a discrete set of points. Thus, the general equation that is employed is:

$$[K]\{\phi\} + [B]\{\dot{\phi}\} = \{P\} + \{Q\} \qquad \text{.....(4.2.1)}$$

where,

{ϕ} is a vector of temperatures at grid points;

{P} is a vector of applied heat flows that are known as functions of time;

{Q} is a vector of non-linear heat flows that depend on temperature;

[K] is a symmetric matrix of constant heat conduction coefficients;

[B] is a symmetric matrix of constant heat capacity coefficients.

The output of the heat transfer analysis includes the temperature at grid points, the temperature gradients and heat fluxes within volume heat conduction elements, and the heat flow into surface elements. Thermal expansion of the elements produces equivalent loads at the grid points. A vector of thermal strains represents thermal expansion, which is used in the load vector given by equation (4.2.2).

$$\{F\} = [Ks]\ \{\delta u\} \qquad \text{.....(4.2.2)}$$

where,

{F} is a vector that represents forces due to body forces, initial strain and initial stress;

[Ks] is material stiffness matrix*;

{δu} displacement vector

**The temperature dependant material data were obtained from military standards.*

4.3 Interpolation of cutting forces

The preliminary runs were carried out using measured cutting forces and temperature data. These runs were primarily used to validate the assumptions used in formulating the finite element model. After calibrating the model (tool and workpiece) other cases were run using interpolated values for the cutting forces and temperatures as

well as flank wear. Experimental measurements of the tool temperature, forces and the wear land were used in a non-linear interpolation scheme to arrive at relations between the cutting forces, temperatures and flank wear relative to the cutting parameters (speed, feed rate and depth of cut). The program Maple [145] was utilized in the calculation of the coefficients of the polynomial.

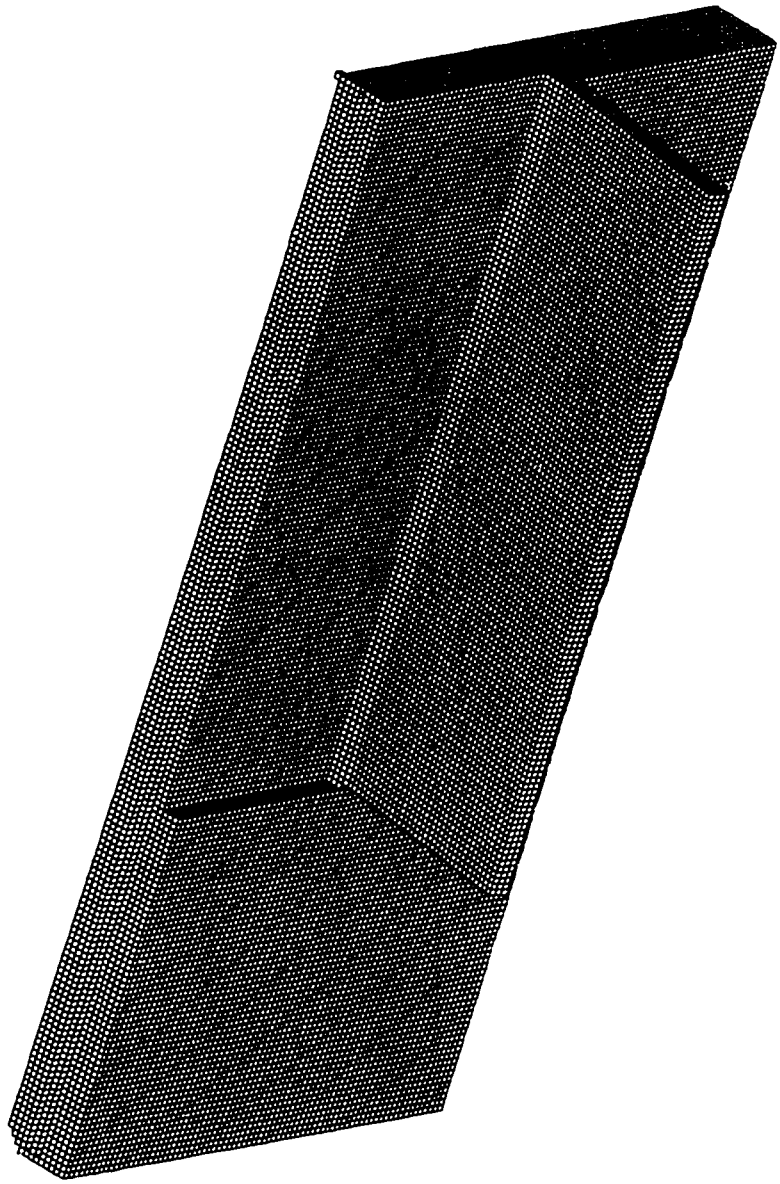

Figure 4.2.1: Meshed Workpiece

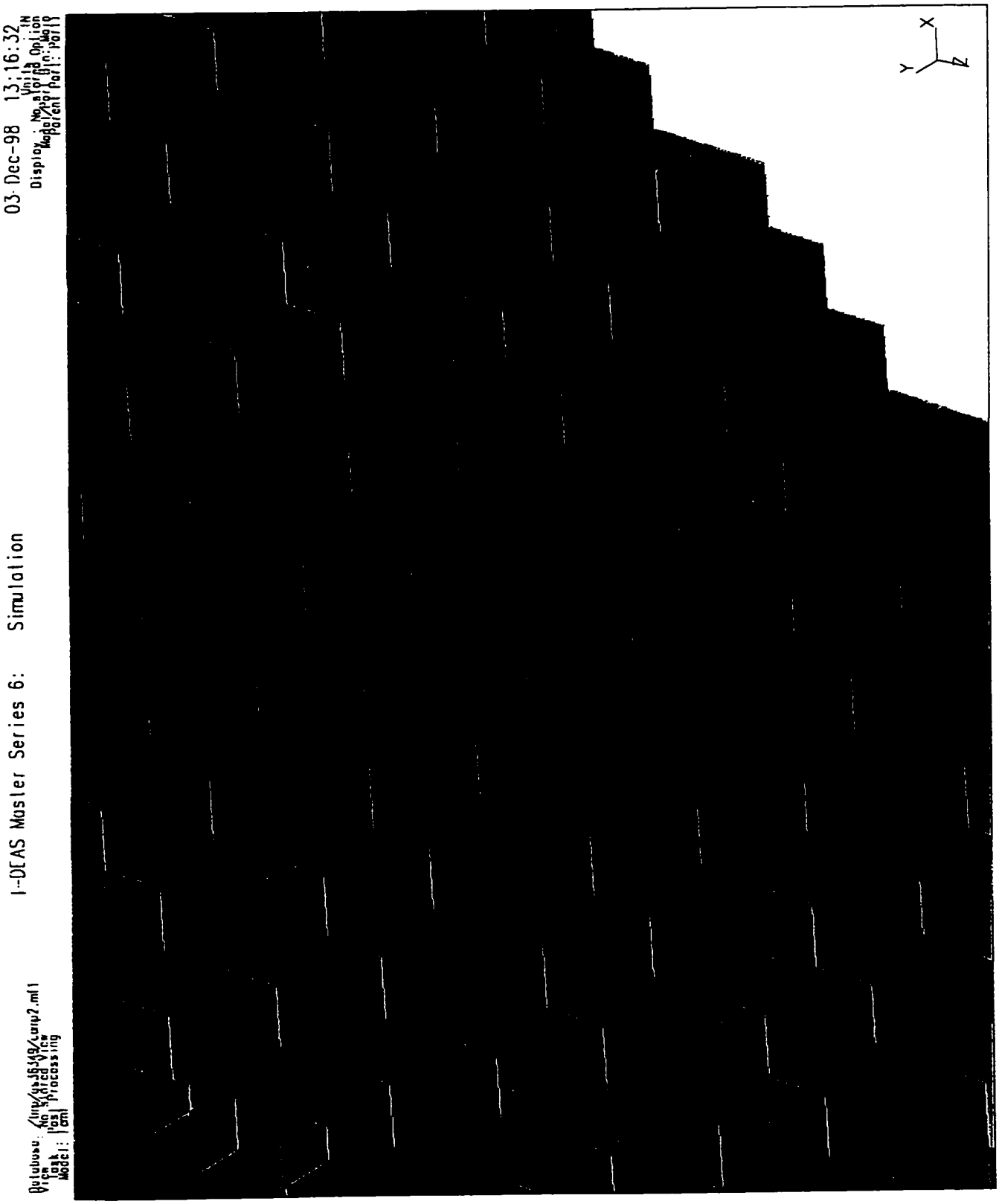

Figure 4.2.2: Magnification of Fig. 4.2.1 – Meshed workpiece

CHAPTER 5

RESULTS

5.1. Cutting Tool

5.1.1 Effect of tool material

A series of preliminary tests was conducted to assess the effect of tool material on the tool wear, cutting forces and cutting temperature during rough turning of 20%SiC/Al PMMC. Fig. 5.1.1 shows that Al_2O_3/TiC tools suffered excessive wear in the form of edge chipping. Al_2O_3 particles are pulled out by the abrading workpiece particles, which have higher Vickers Hardness Number than the Al_2O_3 particles (VHN for Al_2O_3/TiC = 2500Kg_f/mm^2, VHN for SiC=3000Kg_f/mm^2). Crater wear was also observed. This crater wear is due to widening of grooves which were caused by abrasion. Due to severe edge chipping, the cutting forces for the Al_2O_3/TiC tool were much higher than those experienced by TiN coated tools (Table 5.1). TiN coating provided some protection against the abrasive effects of the SiC particles. The superior performance of polycrystalline diamond tools (PCD), compared to both Al_2O_3/TiC and TiN coated carbide tools, is attributed to their high abrasion resistance and high thermal conductivity, which led to lower cutting temperatures, as shown in Table 5.1. Table 5.2 shows a sample of forces measured and recorded during machining using PCD tools.

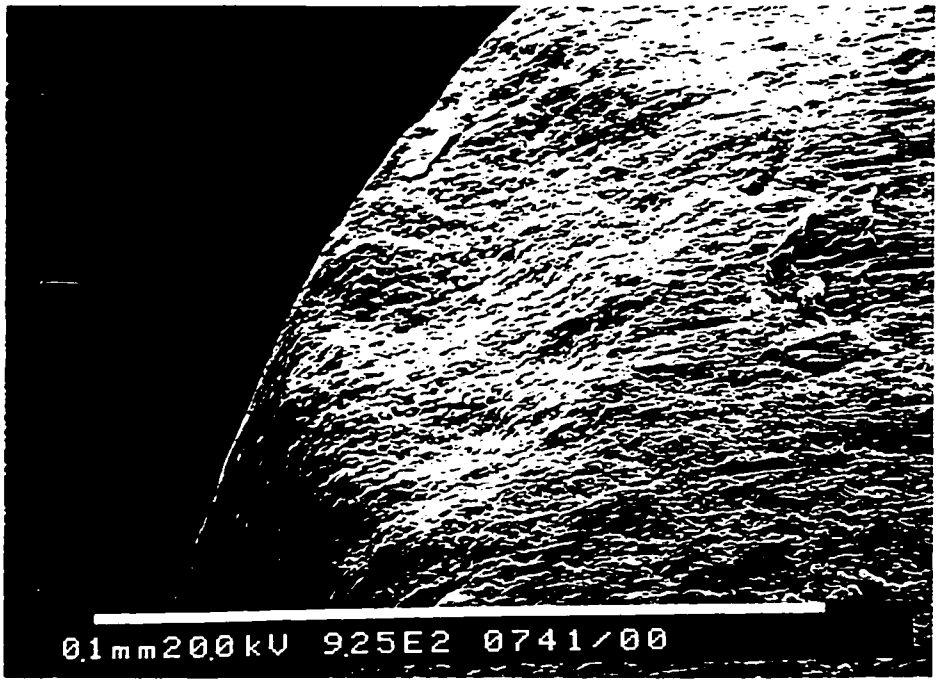

Figure 5.1.1: SEM figure showing wear on Al_2O_3 tool
(v = 488 m/min, f = 0.2 mm/rev, d = 0.5 mm, r = 1.6 mm, $\alpha = 0^o$).

Table 5.1: Effect of Tool Material on Cutting Forces and Temperatures (r=1.6mm, $\alpha=0^o$).

Tool Material	Measured Cutting Forces (N)	Measured Cutting Temperature (^{o}C)
PCD v = 894 m/min, f = 0.45 mm/rev, d = 2.5 mm	97.00	440
PCD v = 670m/min, f = 0.25 mm/rev, d = 1.5 mm	98.10	410
Al_2O_3 v = 248m/min, f = 0.2 mm/rev, d = 0.5mm	183.85	520
	143.52	500

Table 5.2: Cutting Forces During Machining Al/SiC PMMC using PCD tools ($r = 1.6$ mm, $\alpha = 5^o$)

Fx	Fy	Fz
2115.000000	2103.000000	2084.000000
2125.000000	2106.000000	2085.000000
2118.000000	2104.000000	2084.000000
2116.000000	2104.000000	2084.000000
2122.000000	2101.000000	2083.000000
2116.000000	2098.000000	2082.000000
2112.000000	2103.000000	2082.000000
2119.000000	2104.000000	2083.000000
2120.000000	2104.000000	2083.000000
2115.000000	2109.000000	2085.000000
2119.000000	2109.000000	2086.000000
2119.000000	2109.000000	2087.000000
2118.000000	2105.000000	2086.000000
2118.000000	2107.000000	2087.000000
2118.000000	2105.000000	2086.000000
2116.000000	2099.000000	2084.000000
2120.000000	2106.000000	2085.000000
2119.000000	2104.000000	2084.000000
2114.000000	2107.000000	2085.000000
2121.000000	2111.000000	2087.000000
2120.000000	2108.000000	2086.000000
2118.000000	2110.000000	2087.000000
2126.000000	2112.000000	2088.000000
2115.000000	2103.000000	2084.000000
2125.000000	2106.000000	2085.000000
2118.000000	2104.000000	2084.000000
2116.000000	2104.000000	2084.000000
2122.000000	2101.000000	2083.000000
2116.000000	2098.000000	2082.000000
2112.000000	2103.000000	2082.000000
2119.000000	2104.000000	2083.000000
2120.000000	2104.000000	2083.000000
2115.000000	2109.000000	2085.000000
2119.000000	2109.000000	2086.000000
2119.000000	2109.000000	2087.000000
2118.000000	2105.000000	2086.000000
2118.000000	2107.000000	2087.000000
2118.000000	2105.000000	2086.000000
2116.000000	2099.000000	2084.000000

--More--(7%)
[immrc]

The results of the finite element thermal analysis agree with the experimental measurements of the cutting temperatures, as shown in Fig. 5.1.2 which shows the temperature distribution along the PCD tool rake face. As can be seen from Fig. 5.1.2, the highest temperature occurs at the cutting edge and decreases along the rest of the tool rake face.

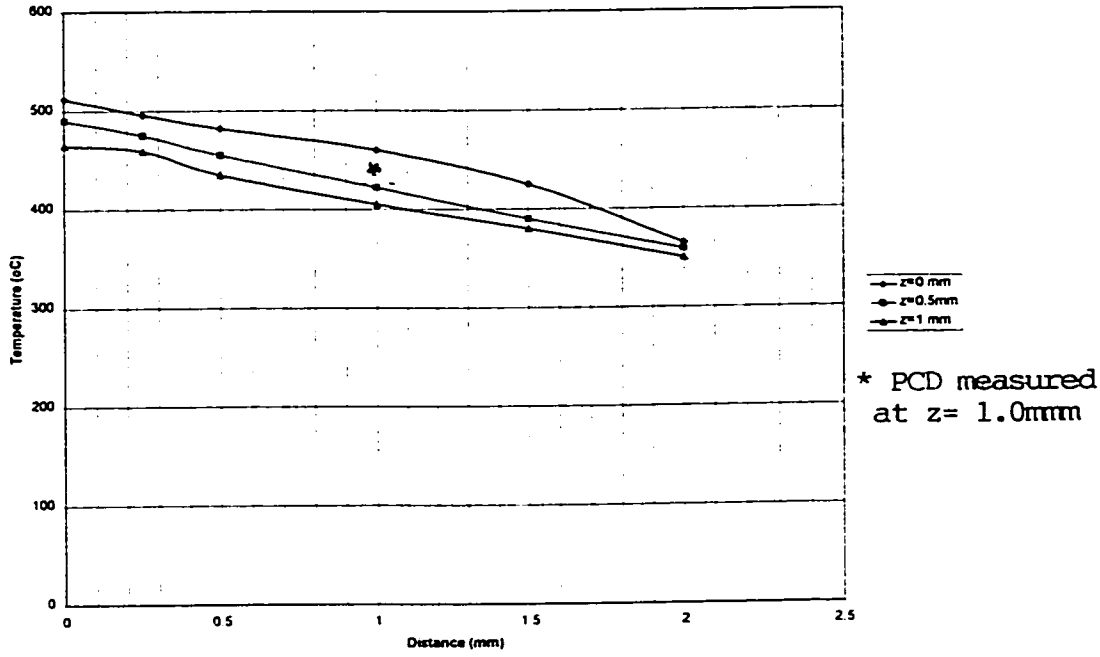

Figure 5.1.2: Temperature distribution on tool rake face
(v = 894 m/min, f = 0.45 mm/rev., d = 2.5mm)

Upon changing the tool material to TiN and Al_2O_3 the temperature profiles changed as shown in Fig. 5.1.3. Comparing the three tool materials, the superior performance (i.e. lower cutting temperatures) of the PCD tools is attributed to the higher thermal conductivity of the PCD compared to TiN and Al_2O_3.

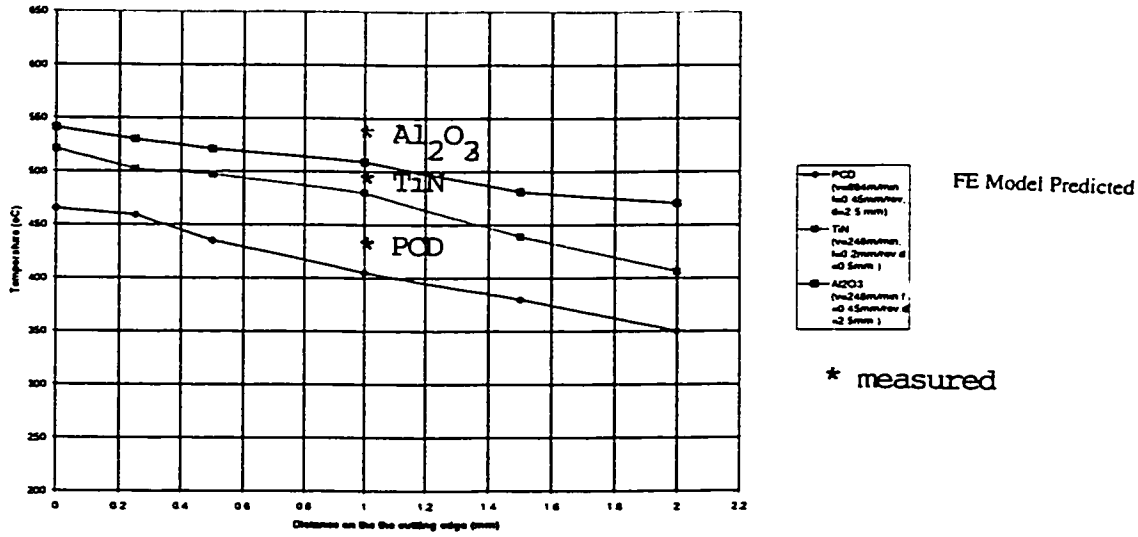

Figure 5.1.3: Effect of Tool Material on Temperature Distribution on the Tool Rake Face (z=1).

The effect of the tool material on the minimum principal stresses in the tool is presented in Fig. 5.1.4. As can be seen from Fig. 5.1.4 the PCD tool endures the least stresses, and thus expected to suffer the least crater wear. These results are also in agreement with the experimental observations as shown in the microscopic views in Fig. 5.1.5-a and Fig. 5.1.5-b.

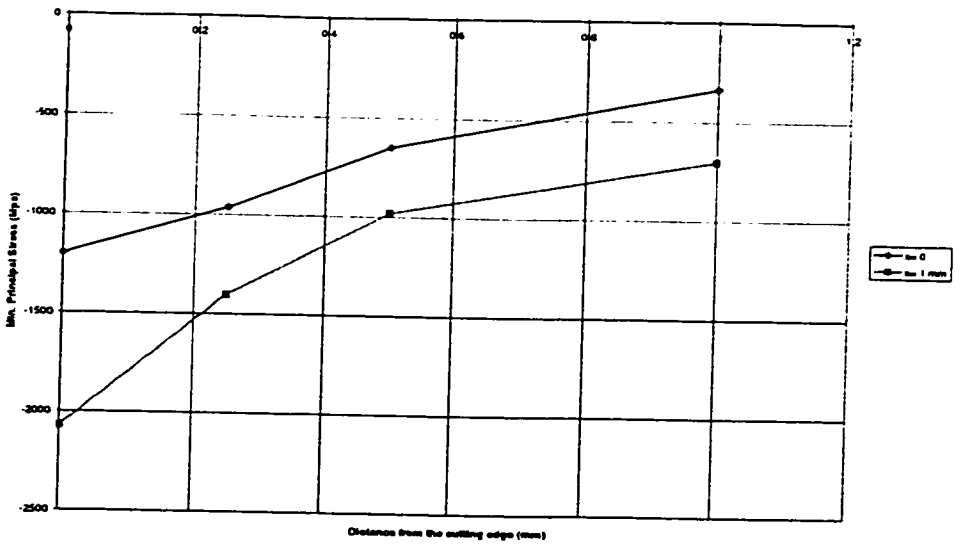

Figure (5.1.4): Minimum principal stress
Distribution on the tool rake face.

Figure 5.1.6 shows the effect of the PCD layer thickness on the maximum shear stresses in the tool. Increasing the PCD layer thickness, which has superior thermal and mechanical properties, clearly lowers the tool stress; yet the selection of the optimum thickness of the PCD layer would depend on cost factors. Fig. 5.1.7a and Fig. 5.1.7b show the effect of thhe PCD layer thickness on the tool life.

All machinability studies carried out thereafter were concerned with the optimization of the cutting process using PCD tools.

Figure 5.1.5a: Crater Wear - TiN tool

(v = 248 m/min, f = 0.2 mm/rev., d = 0.5 mm).

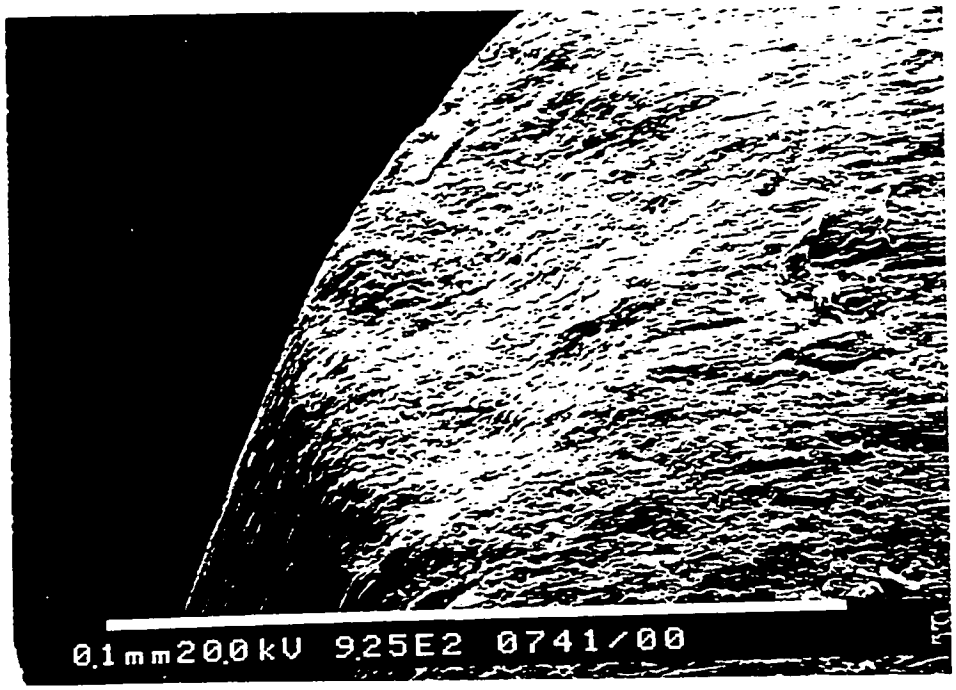

Figure 5.1.5b: Crater Wear - Al_2O_3

(v = 248 m/min, f = 0.2 mm/rev., d = 0.5 mm).

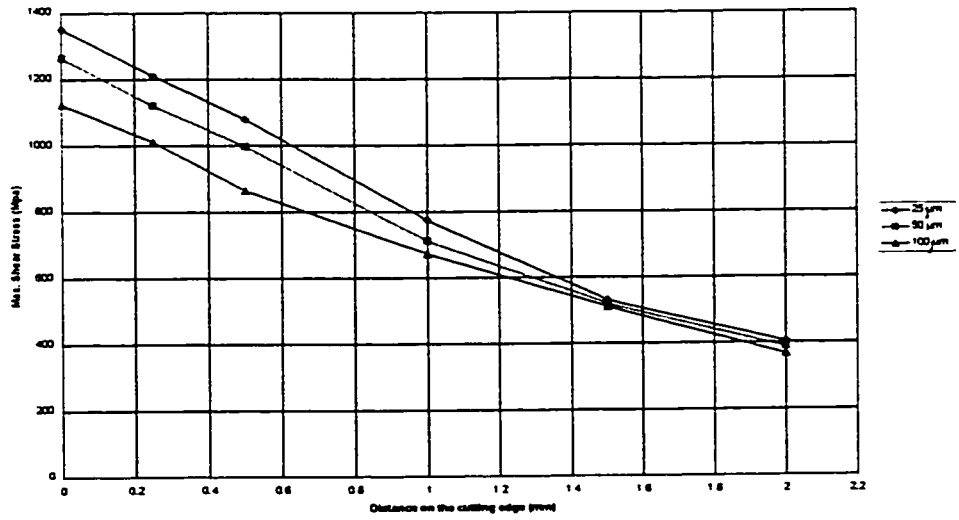

Figure 5.1.6: Effect of PCD layer thickness on the maximum shear stress distribution on the tool rake face
(v = 894 m/min, f = 0.25 mm/rev., d = 2.5 mm).

(a)

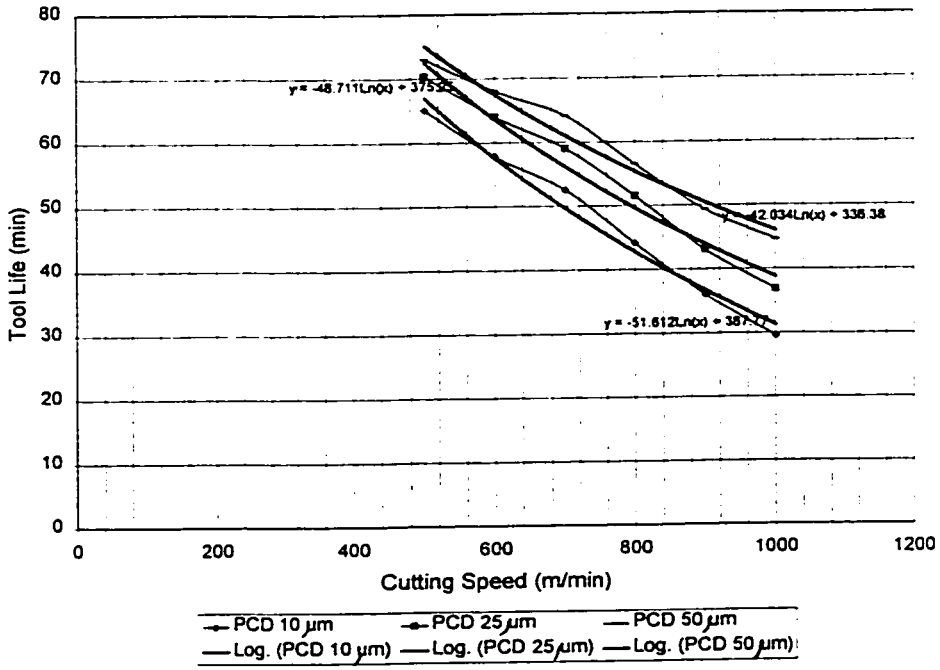

(b)

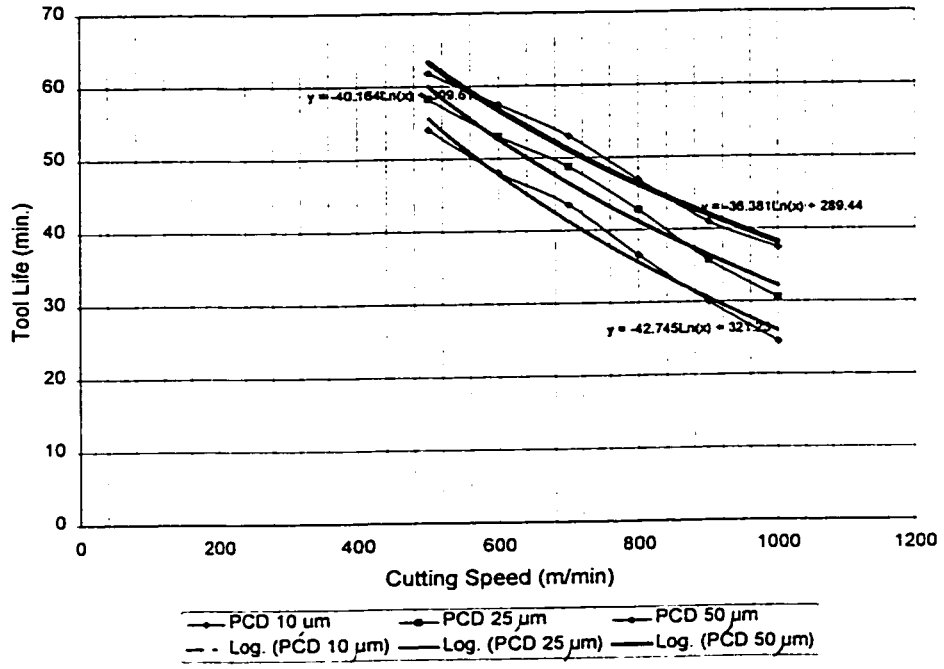

Figure 5.1.7: Variation of PCD Tool life with the cutting speed and depth of cut (α=0°) (a) d = 1.5 mm; (b) d = 2.5 mm.

5.1.2. Effect of Cutting Parameters

Fig. 5.1.8a and Fig. 5.1.8b show that as the cutting speed and/or the depth of cut increase, the cutting forces decrease. This could be attributed to thermal softening of the workpiece material. Another possible reason is due to the changes introduced into the tool geometry upon the formation of built-up edge. Fig. 5.1.9b shows an X-ray dispersion of the built-up material shown in Fig.5.1.9a.

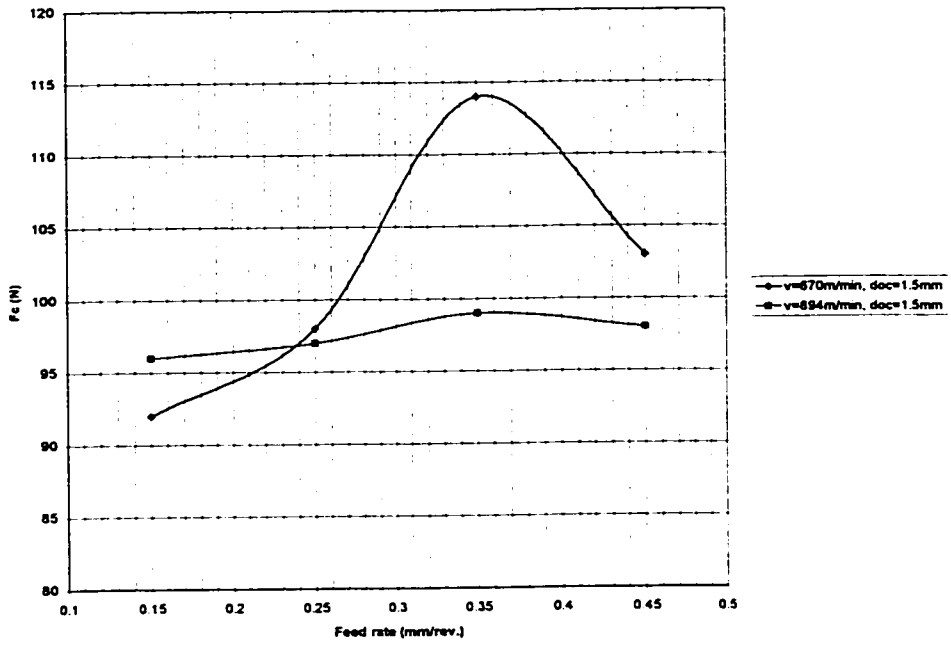

Figure 5.1.8a: Effect of cutting speed on the cutting forces.

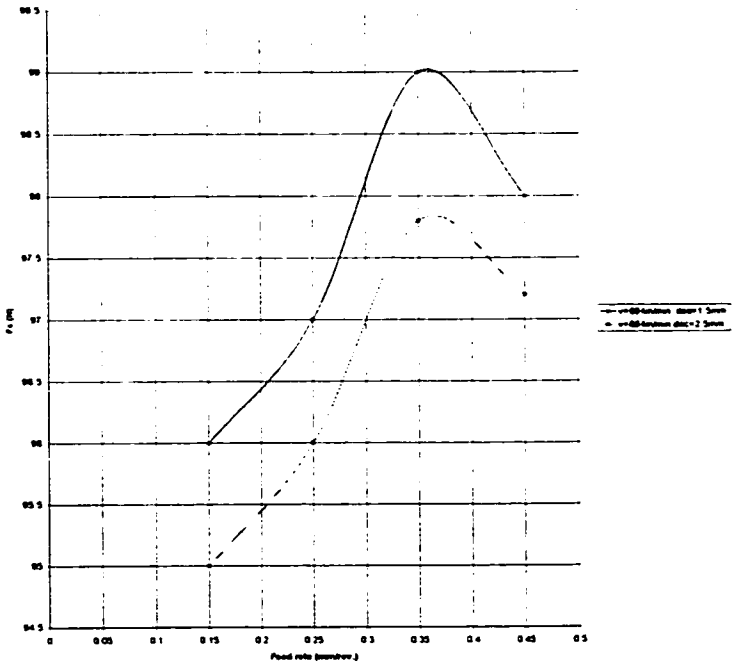

Figure 5.1.8b: Effect of depth
of cut on the cutting forces.

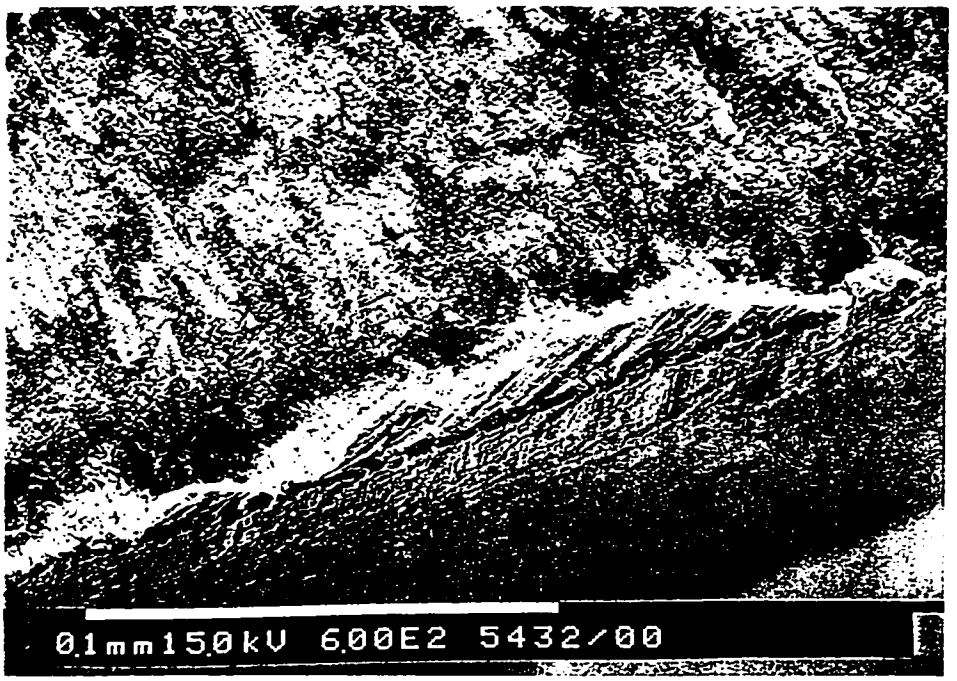

Figure 5.1.9a: Built-up edge on PCD tools
(v = 670 m/min, f = 0.25 mm/rev., d = 2.5 mm, r = 1.6 mm., $\alpha = 0^{o}$)

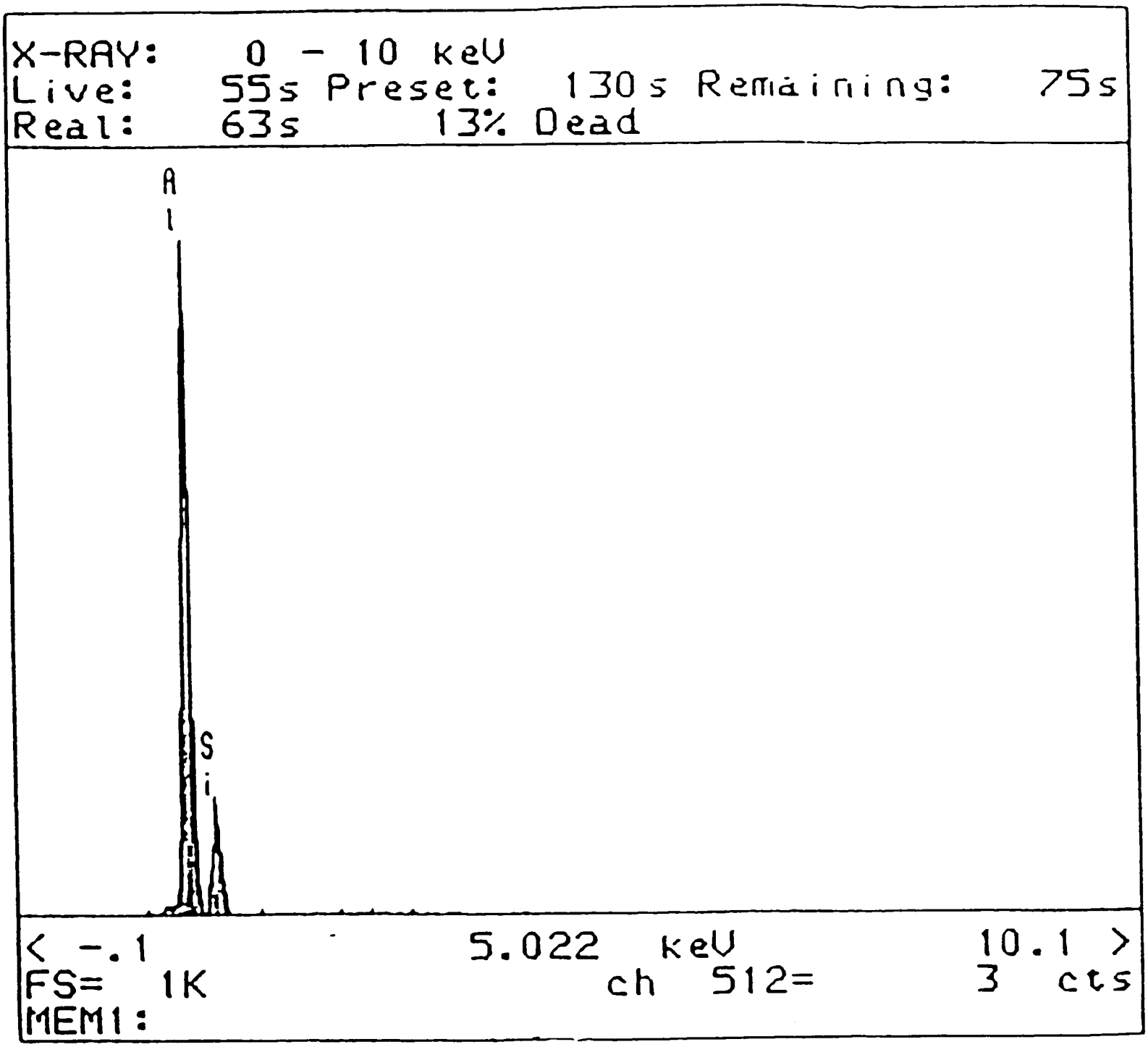

Figure 5.1.9b: X-ray dispersion of built-up edge shown in Fig. 5.1.9a.

At high cutting speeds (v = 894m/min in Fig. 5.1.10b), a smaller BUE is formed, compared to the BUE formed at v=670m/min (Fig. 5.1.10a). (The height of the BUE was measured perpendicular to the rake face) On the other hand, by increasing the depth of cut from 1.5 mm to 2.5 mm a larger BUE is formed (Fig. 5.1.11a, and Fig. 5.1.11b), which could break off the tool causing tool chipping and other adverse effects on the workpiece surface finish and dimensional accuracy.

Topographies of the tool rake face indicate that the main wear mechanism of PCD is abrasion (manifested as grooves parallel to the chip flow direction). These grooves could be attributed to three factors. The first is that Al_2O_3 is formed at the tool edge, which is hard enough to produce grooving wear in the PCD. The second explanation for the PCD grooving is aluminum seizure and pull out process of the PCD grain, as shown in Fig. 5.1.12a and Fig. 5.1.12b. The third possible reason behind PCD grooving is that SiC particles abrade the tools. Thus, PCD tools with PCD grains larger than the grain size of the SiC particles could better withstand the abrasion and "microcutting" by the SiC particles. However, one should note that as the size of the PCD grains increases, the fracture properties of the PCD tool deteriorate, due to increased number of flaws in the material.

(a)

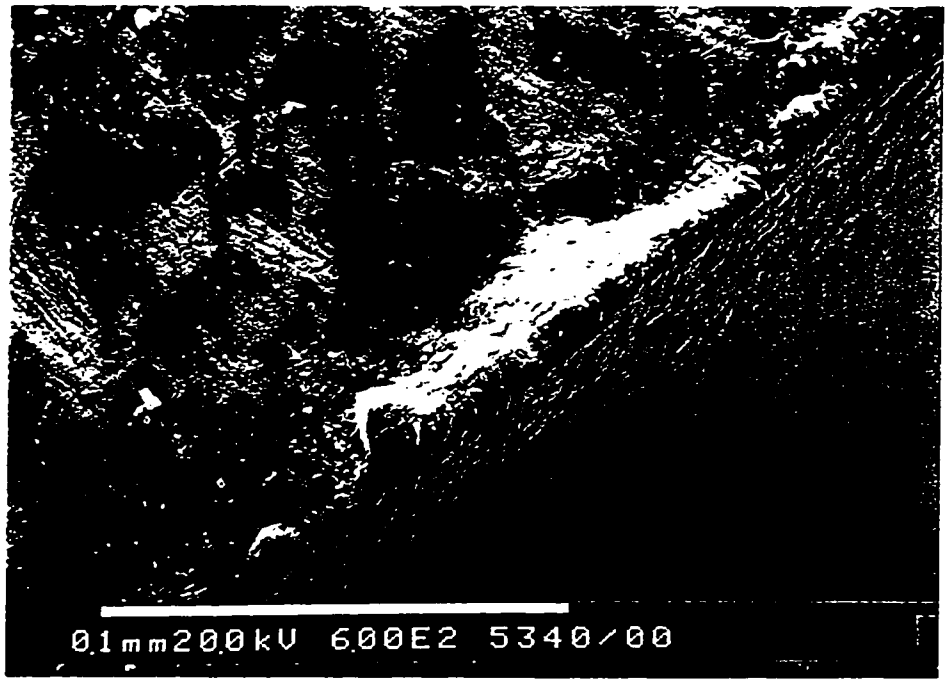

(b)

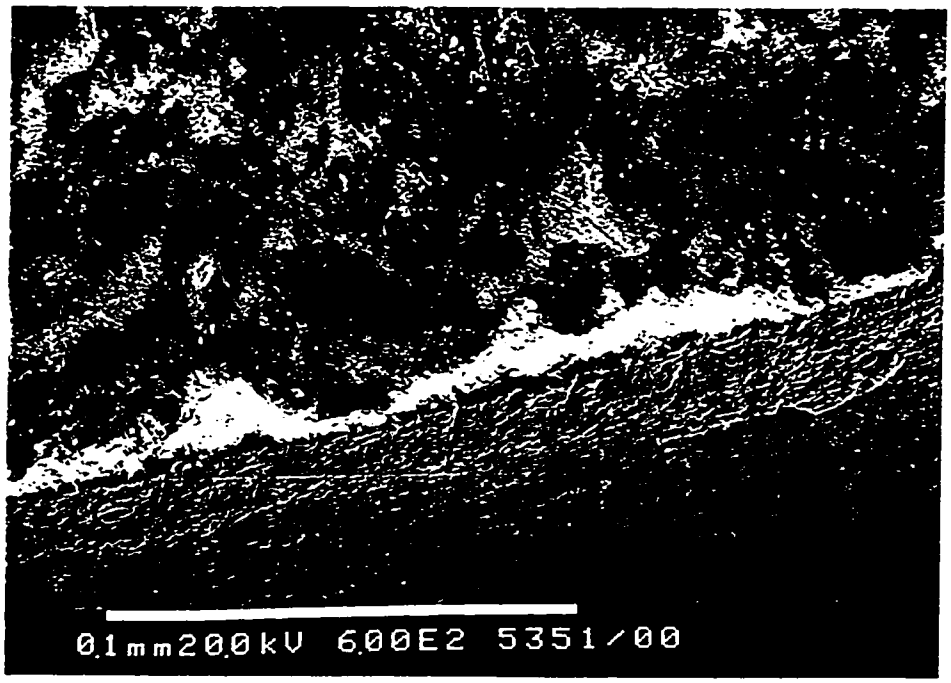

Figure 5.1.10: Built-up edge on PCD tools (f = 0.45 mm/rev., d = 2.5 mm, r = 1.6 mm, α=0°); (a) v = 670 m/min; (b) v = 894 m/min.

(a)

(b)

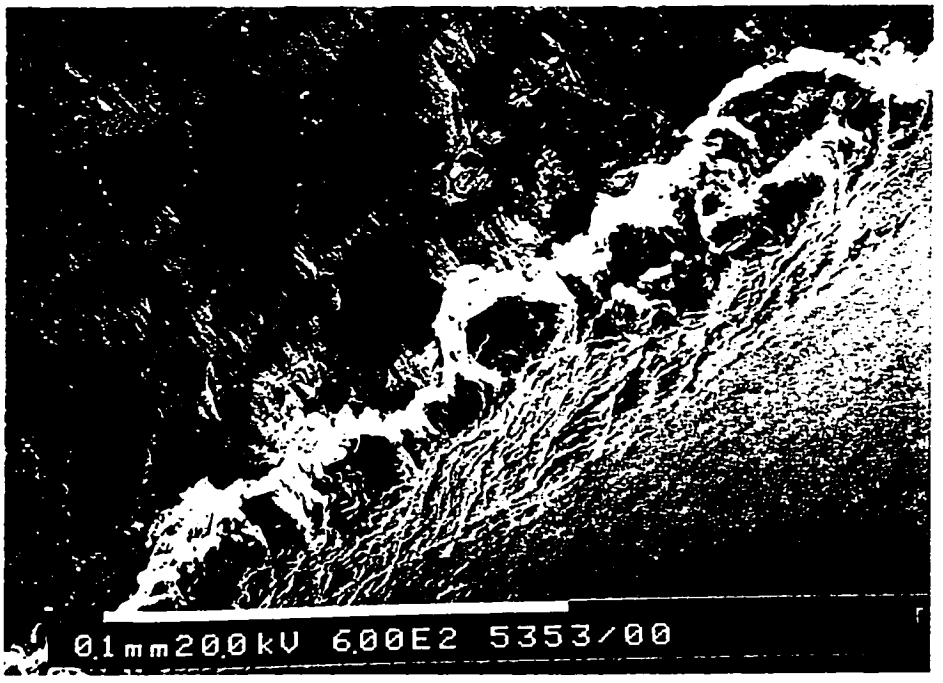

Figure 5.1.11: Built-up edge on PCD tools (v = 670 m/min, f = 0.35 mm/rev., r = 1.6 mm, $\alpha = 0^{o}$); (a) d = 1.5 mm; (b) d = 2.5 mm.

(a)

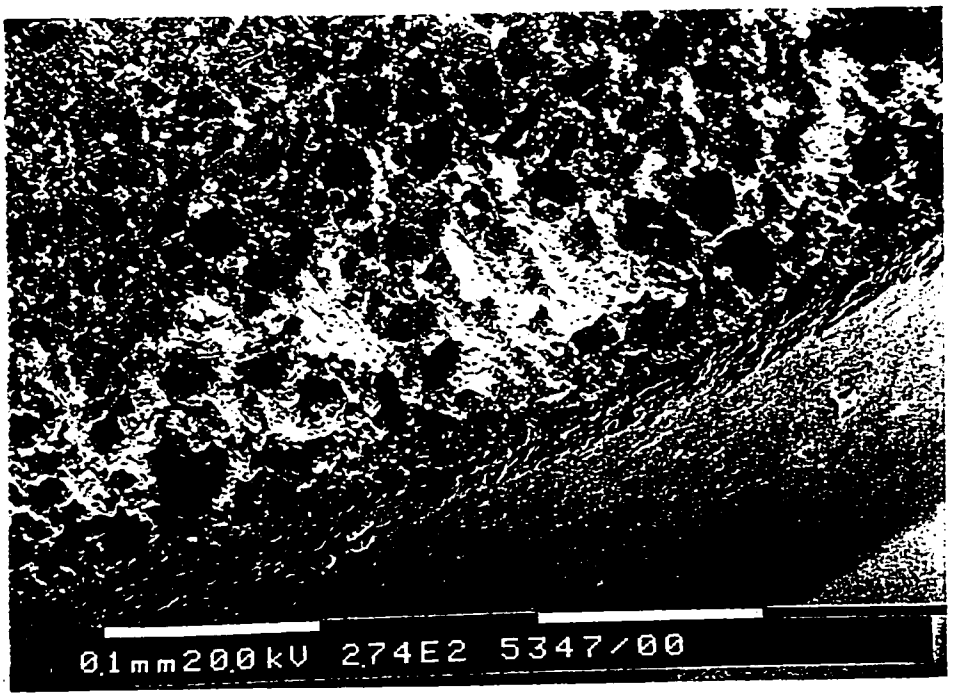

(b)

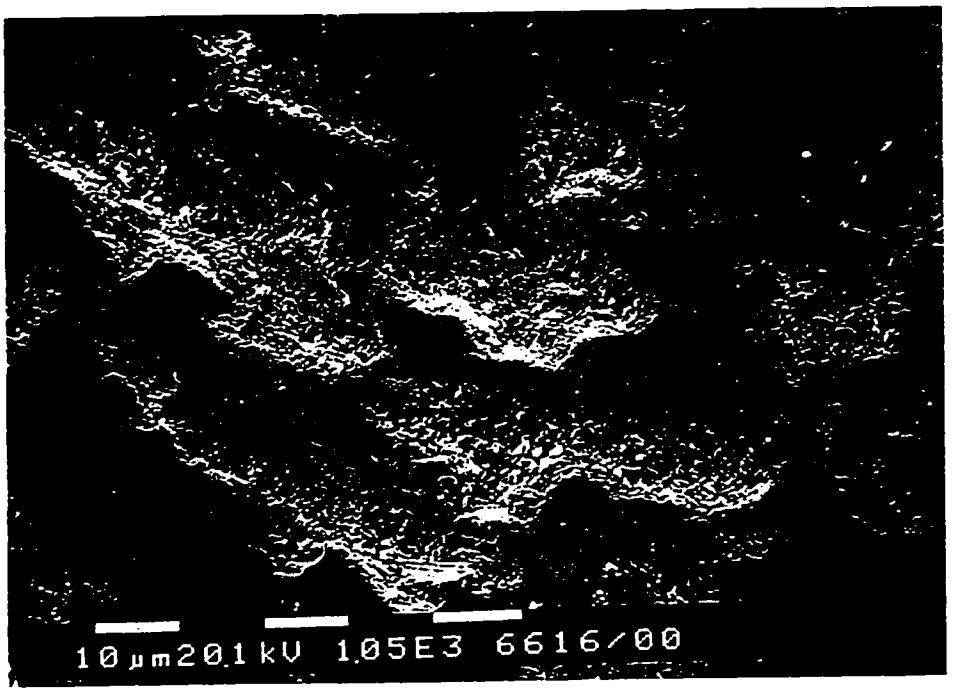

Figure 5.1.12: (a) SEM image illustrating the wear on the PCD tool rake face after dissolving the BUE with NaOH (v = 670 m/min, f = 0.15 mm/rev., d = 1.5mm, r =1.6 mm, $\alpha=0^{o}$); (b) higher magnification of the rake face of the tool shown in Fig. 5.1.11a.

The grooves that were formed on the tool face were filled with the workpiece material. This adhering layer somewhat protected the tool rake face against further abrasion. Nonetheless, the tool flank face continued to be subjected to wear by abrasion. Hence, flank wear (Vb) was taken as the tool life criterion with Vb_{lim}=0.18 mm. Fig. 5.1.13 shows that as the cutting speed increases, the flank wear increases. This could be attributed to the increase in the kinetic energy of the abrading particles, as previously suggested by Lane [19-21].

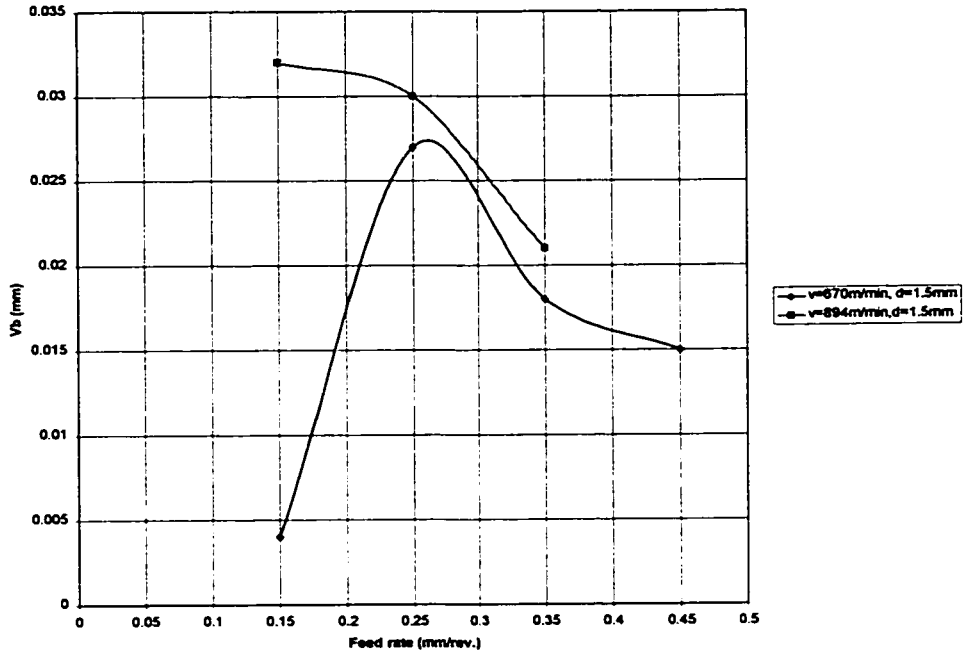

Figure 5.1.13: Effect of the cutting speed
on tool flank wear (PCD tool r = 1.6 mm, $\alpha = 0^{o}$).

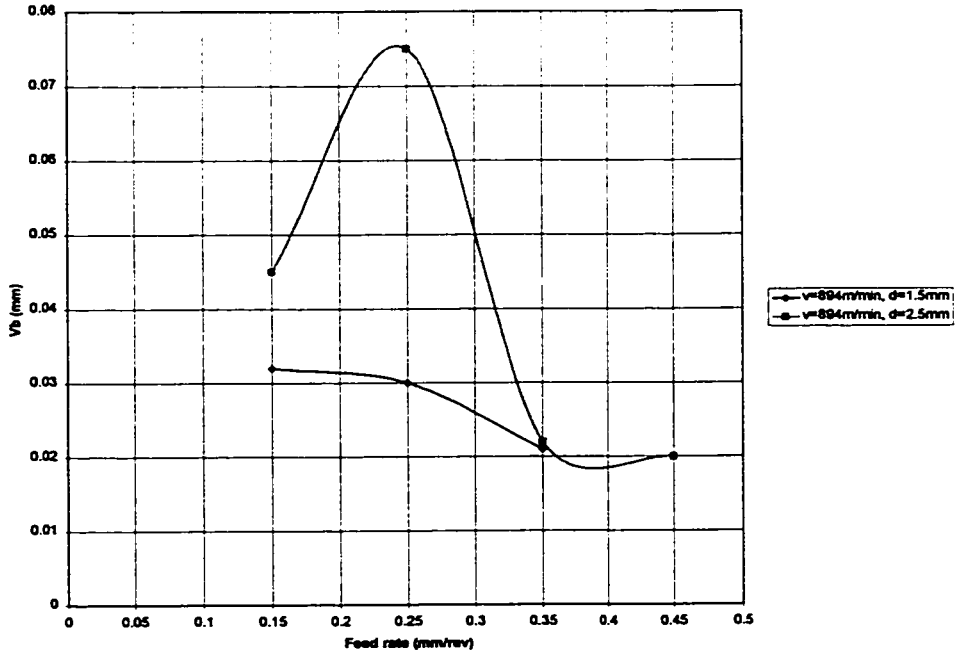

Figure 5.1.14: Effect of the depth of cut
on tool flank wear (PCD tool r = 1.6 mm, $\alpha = 0^{o}$).

Increasing the depth of cut leads to an increase in the flank wear (Fig. 5.1.14). This is attributed to enhanced abrasion wear by microcutting at the tool flank face. To illustrate this point, in case of higher depth of cut a larger surface area of the tool flank face is exposed to abrasion.

The results of the finite element stress analysis explain the tool wear observed. Fig. 5.1.15a, Fig. 5.1.15b and Fig. 5.1.15c show regions of constant stress representing maximum principal stresses in the PCD tool. They indicate that tensile stresses exist at the tool tip. Away from the cutting tip the stresses decrease. Compressive stresses, of low values, are also observed far from the cutting edge. Fig. 5.1.16a, Fig. 5.1.15b and Fig. 5.1.15c show the distribution of the minimum principal stresses along the tool rake face. As can be seen from Fig. 5.1.16a, Fig. 5.1.15b and Fig. 5.1.15c, high compressive stresses are formed close to the tool wedge. The results in Fig. 5.1.15a, Fig. 5.1.15b and Fig. 5.1.15c and those in Fig. 5.1.16a, Fig. 5.1.16b and Fig. 5.1.16c indicate that high compressive and tensile stresses occur in the vicinity of the tool cutting wedge, which could result in the fracture of some parts of the tool (tool pitting) if these stresses exceed the ultimate tensile strength of the tool material. The maximum compressive stresses occur in the vicinity of the cutting edge where high temperatures also exist (Fig. 5.1.2 and Fig. 5.1.3). The combination of the high compressive stresses and high temperatures could lead to the formation of crater wear. According to the finite element results (Fig. 5.1.2, Fig. 5.1.16a, Fig. 5.1.15b and Fig. 5.1.15c), crater wear is expected to start at the tool cutting edge and extends 0.7 mm on to the tool's rake face. These results are in agreement with the experimental observations as illustrated in the microscopic views shown in Fig. 5.1.17.

The amount of tool material removed at the crater wear location depends on the abrasion characteristics of the tool material relative to the workpiece. The experimental work, specifically SEM examination of the tools, showed that the crater wear appeared to develop by abrasion.

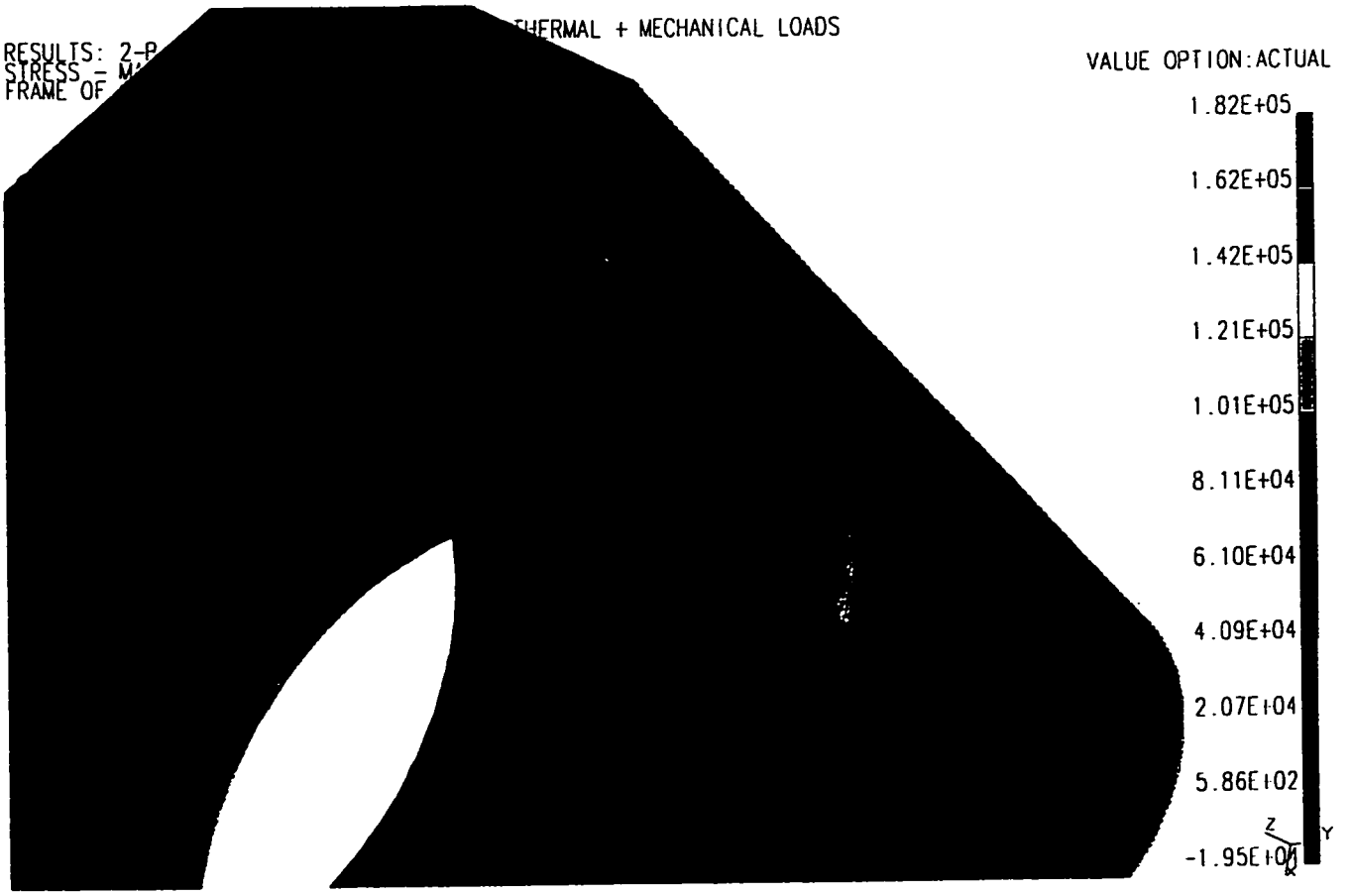

Figure 5.1.15a: Max. principal stresses [x10^{-3} MPa]- PCD tool
(v = 894 m/min, f = 0.35 mm/rev, d = 2.5 mm)

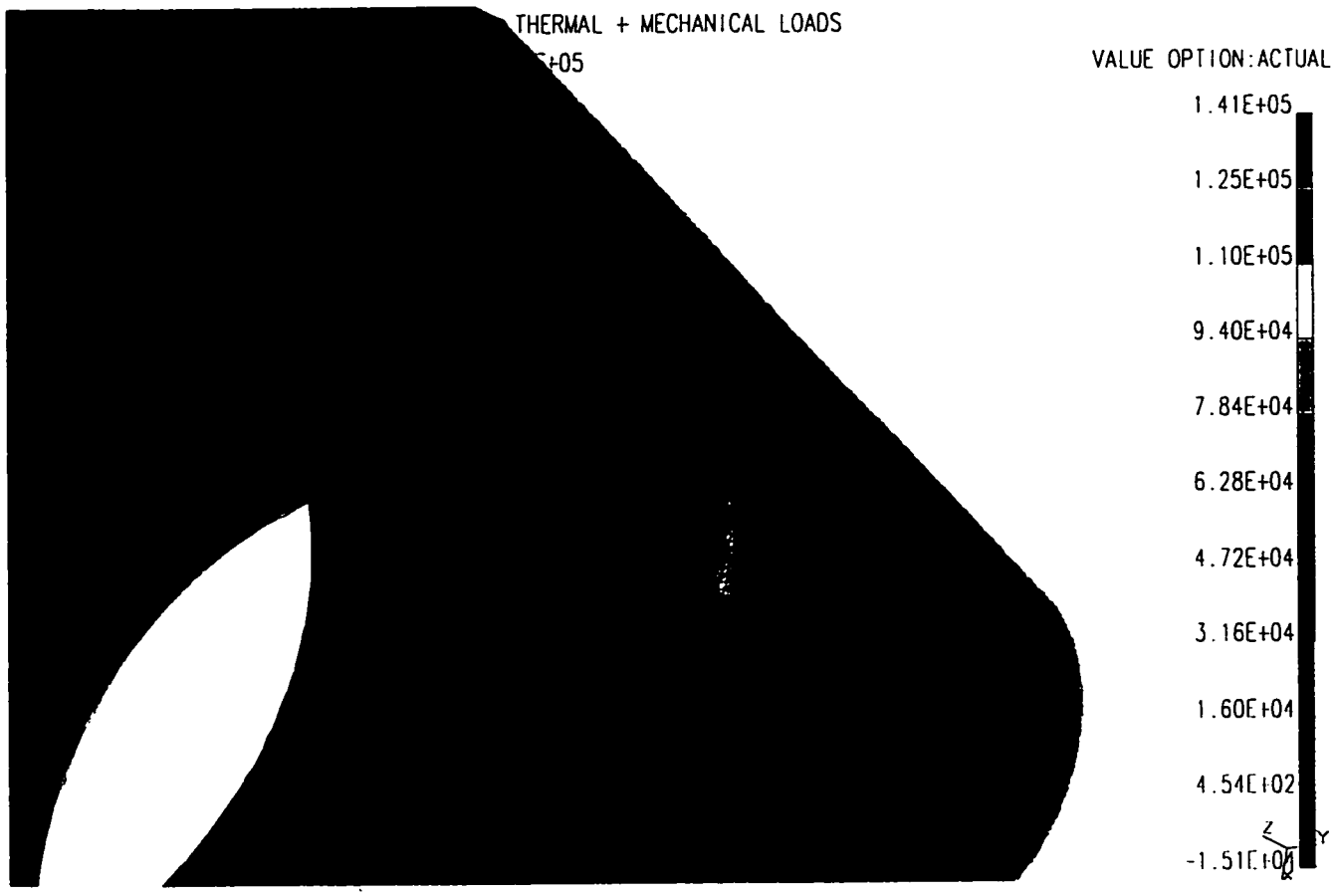

Figure 5.1.15b: Max. principal stresses [x10^{-3} MPa]- PCD tool
(v = 894 m/min, f = 0.35 mm/rev, d = 1.5 mm)

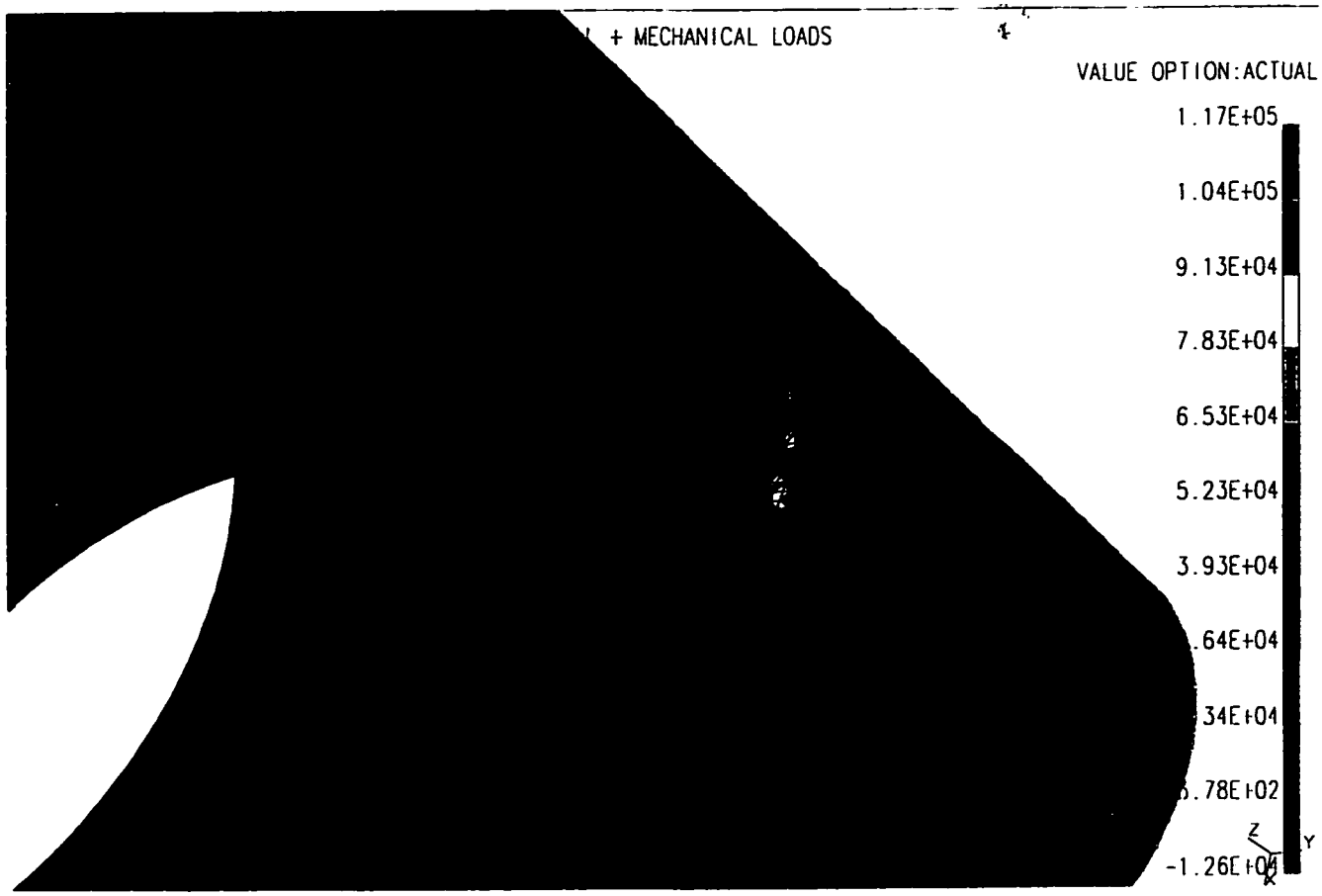

Figure 5.1.15c: Max. principal stresses [x10^{-3} MPa]- PCD tool
(v = 670 m/min, f = 0.35 mm/rev, d = 2.5 mm).

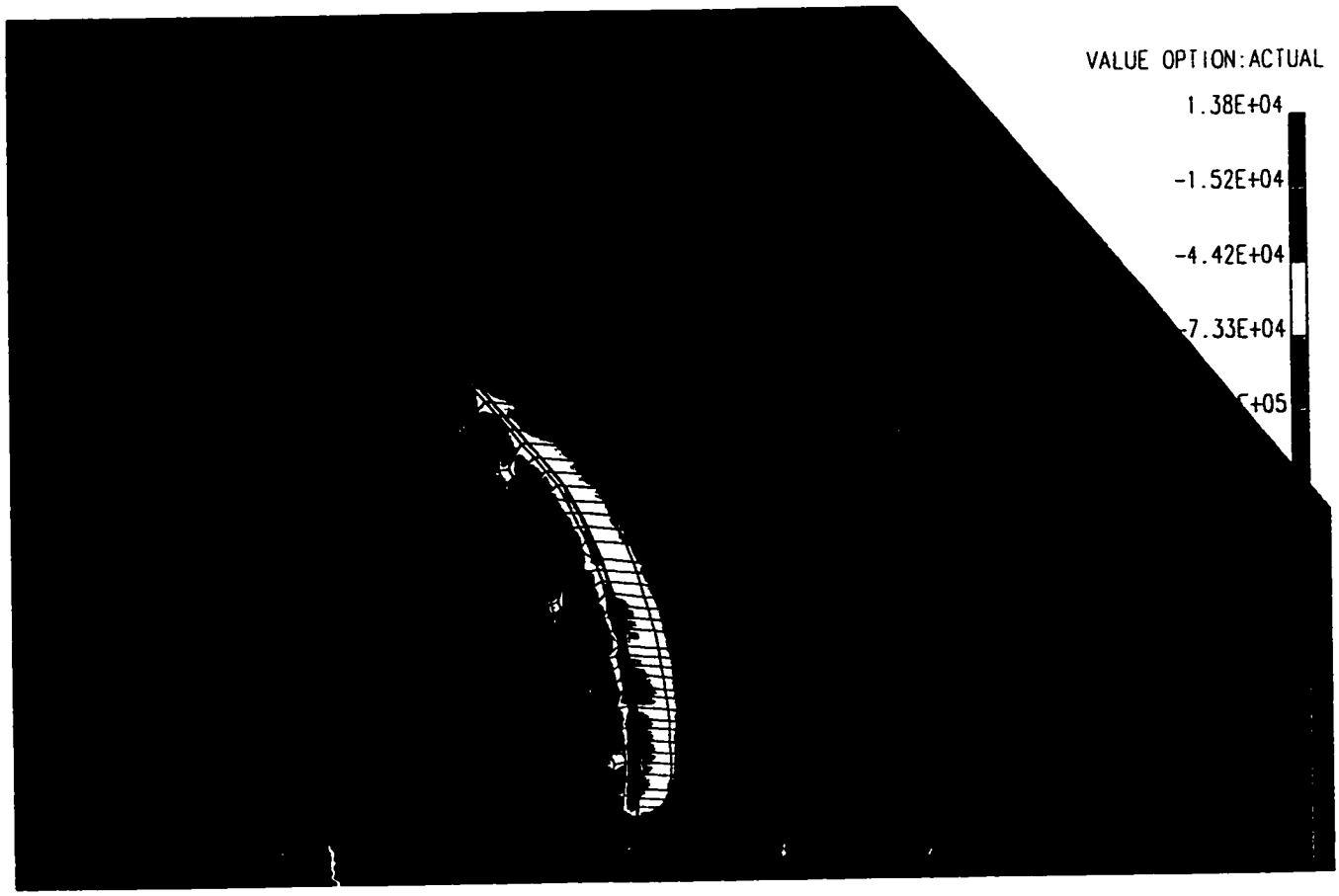

Figure 5.1.16a: Minimum principal stresses [x10^{-3} MPa]– PCD tool
(v = 894 m/min, f = 0.25 mm/rev, d = 2.5 mm) .

113

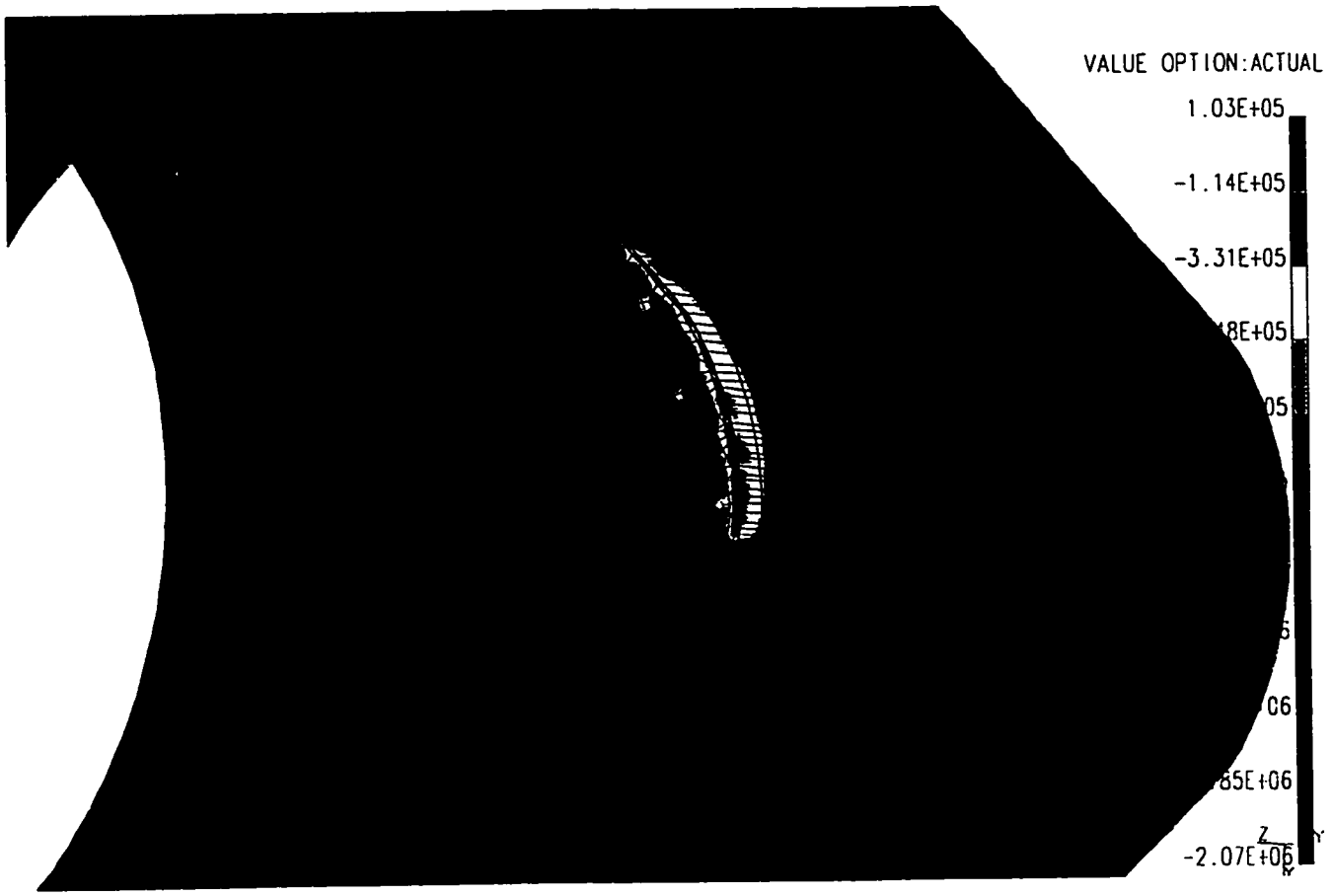

Figure 5.1.16b: Minimum principal stresses [x10^{-3} MPa] – PCD tool
(v = 894 m/min, f = 0.35 mm/rev, d = 1.5 mm).

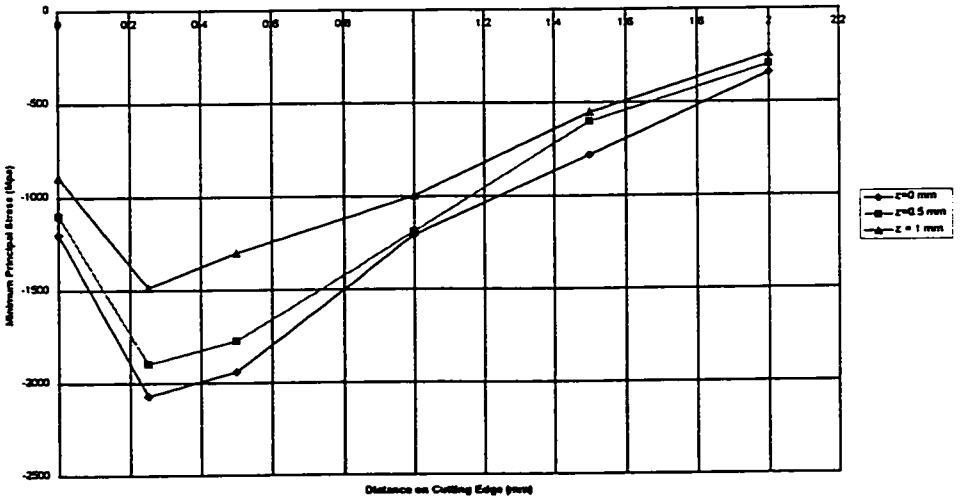

Figure 5.1.16c: Minimum principal stress distribution on tool rake face
(v = 894 m/min, f = 0.45 mm/rev, d = 1.5 mm).

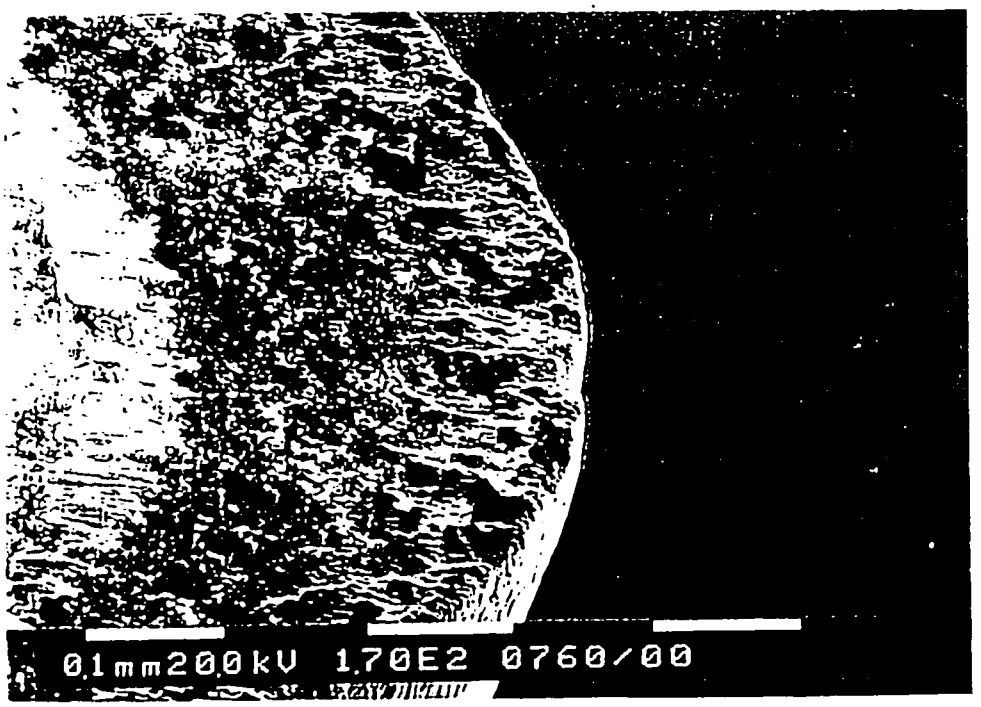

Figure 5.1.17: PCD Tool Wear
(v =894 m/min, f = 0.25 mm/rev., d = 2.5 mm).

Another important stress component is the shear stress. Fig. 5.1.18a, Fig. 5.1.18b and Fig. 5.1.18c show the maximum shear stress distribution along the tool rake face. As can be seen from Fig. 5.1.18a, Fig. 5.1.18b and Fig. 5.1.18c high shear stresses exist at the tool tip. Similar trends occurred for the other tool materials. These high shear stresses combined with high temperatures in the cutting tip vicinity could lead to ductile failure of the tool by shearing. These results are confirmed by the experimental observations shown in Fig. 5.1.19, which show chipped inserts. The appearance of the chipped surfaces is smooth indicating that it occurred gradually, i.e. shearing.

Fig. 5.1.20 and Fig. 5.1.21 show the effect of the cutting parameters on the shear stresses in the tool. As previously presented in [146] increasing the feed rate appears to be beneficial. Increasing the feed rate from 0.25 mm/rev to 0.55 mm/rev led to an increase of less than 5% in the shear stresses.

Finally, Fig. 5.1.22 shows the variation of the tool life with the cutting speed and feed rate at a depth of cut = 2.0 mm.

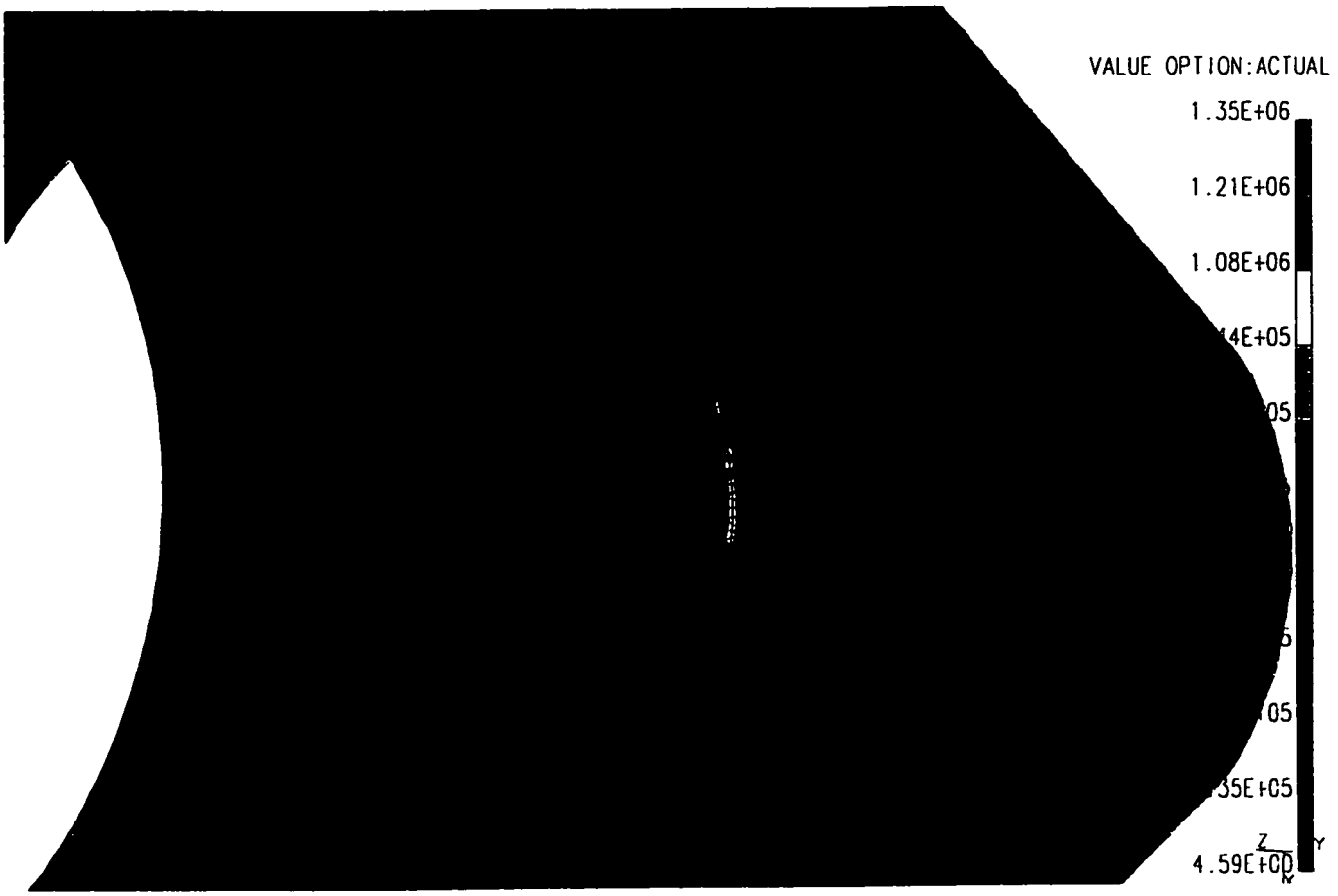

Figure 5.1.18a: Maximum shear stresses [x10^{-3} MPa]– PCD tool
(v = 894 m/min, f = 0.25 mm/rev, d = 2.5 mm) .

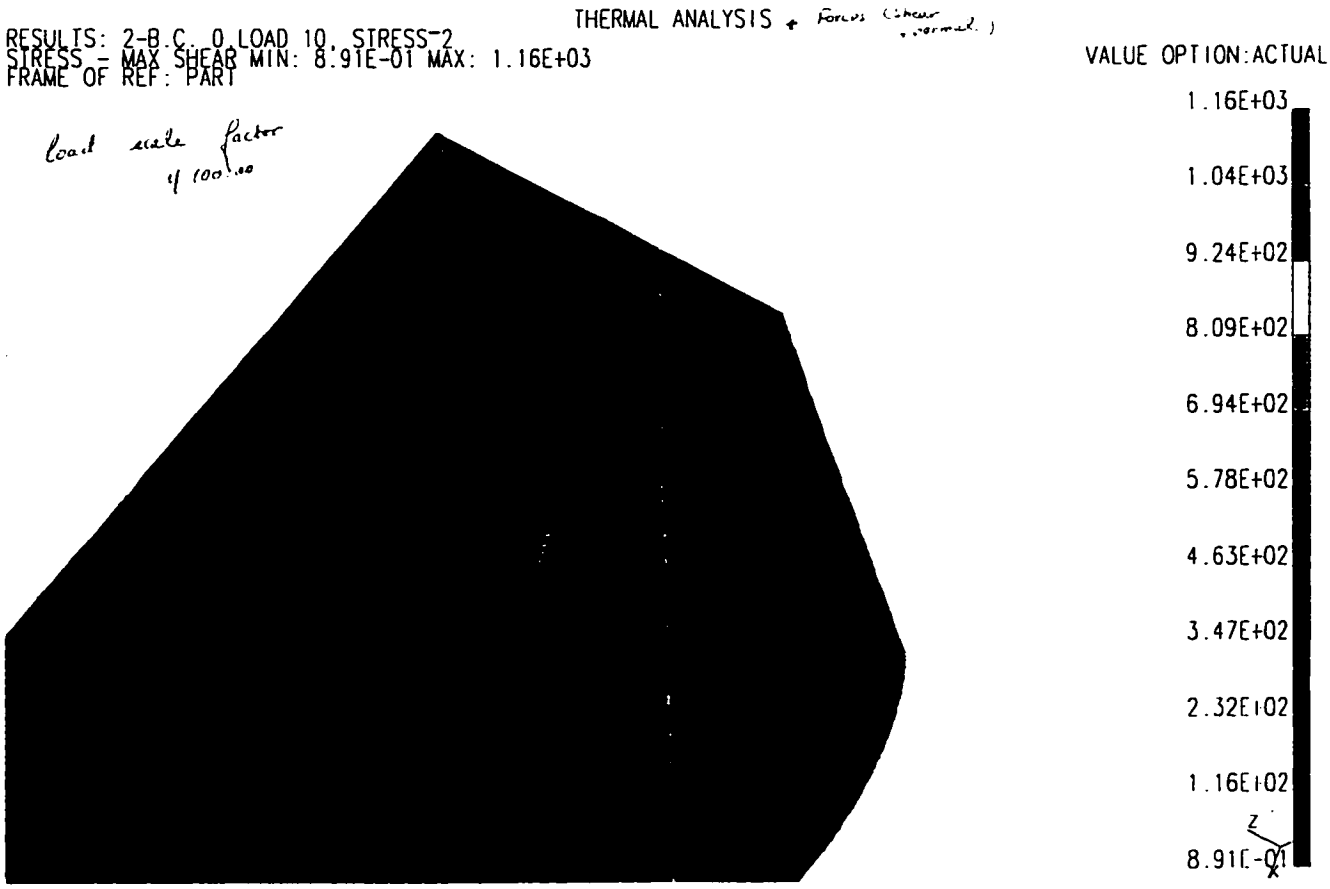

Figure 5.1.18b: Maximum shear stresses [x10^{-3} MPa]– PCD tool
(v = 894 m/min, f = 0.35 mm/rev, d = 1.5 mm) .

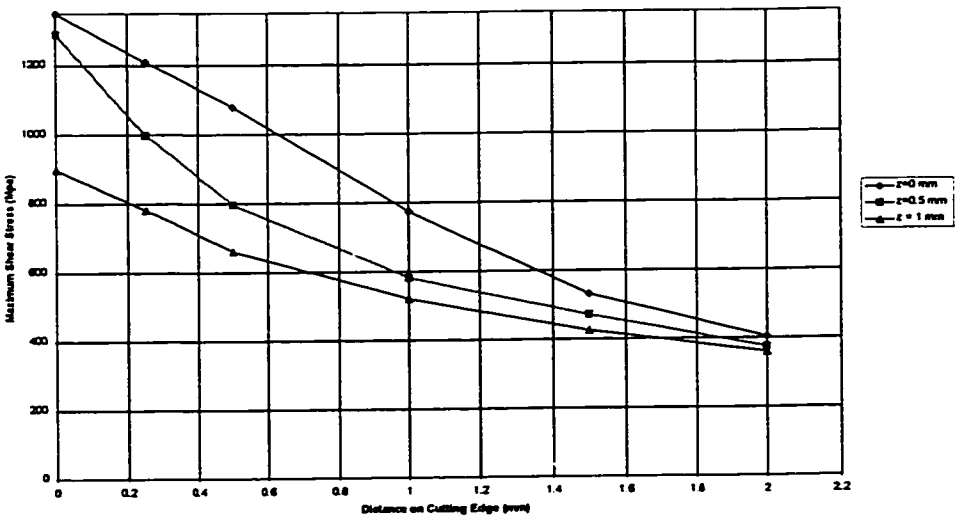

Figure 5.1.18c: Maximum Shear Stress distribution on Tool Rake Face

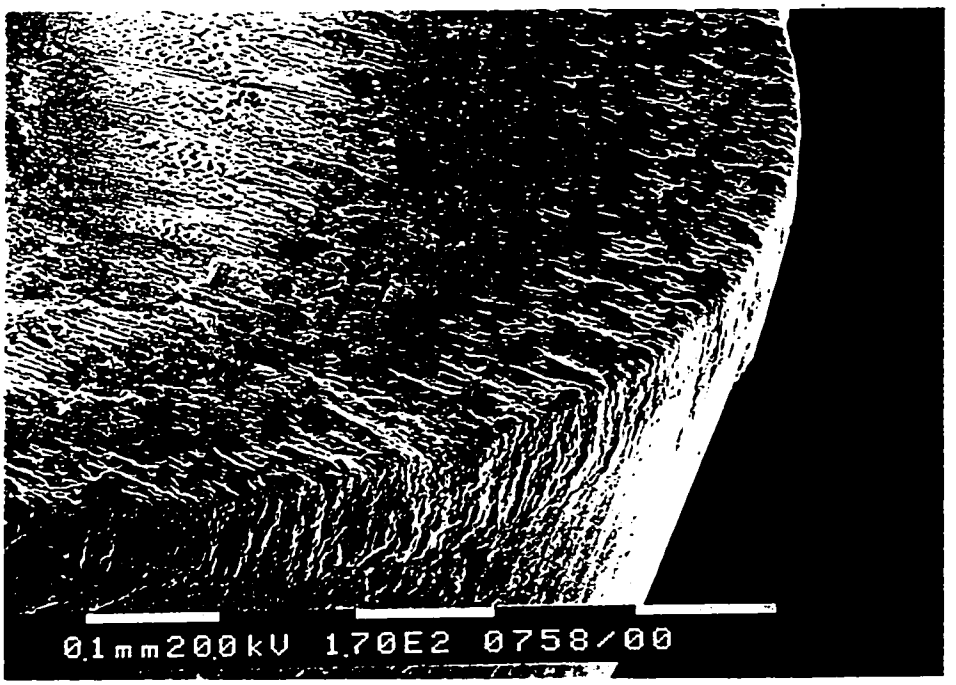

Figure 5.1.19: Chipping in PCD Tool

(v = 894 m/min, f = 0.35 mm/rev., d = 1.5 mm).

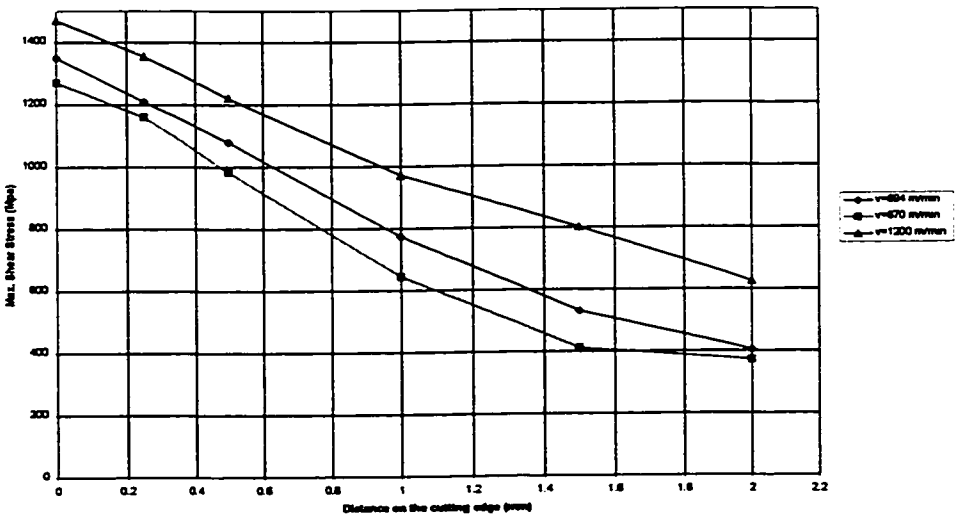

Figure 5.1.20: Effect of Cutting Speed on Maximum Shear Stress Distribution on the Tool Rake Face (f = 0.25 mm/rev., d = 2.5 mm).

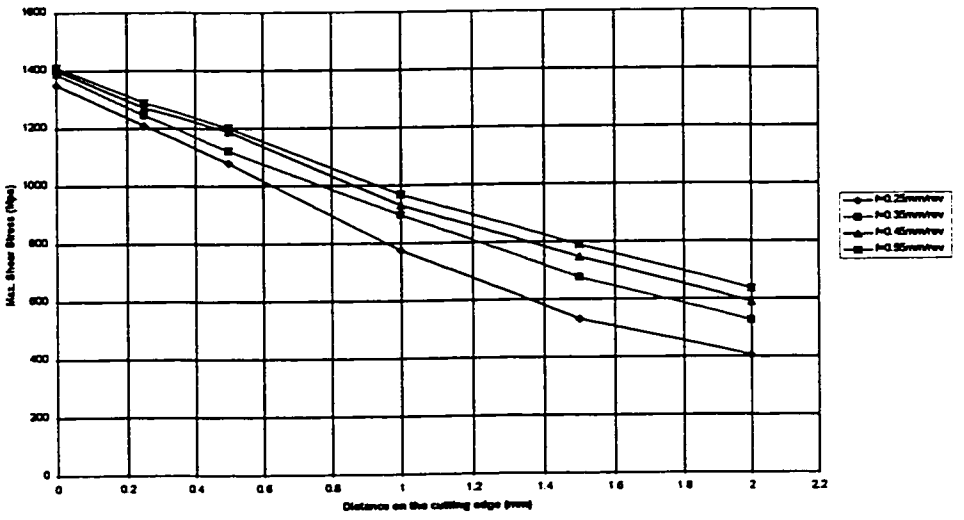

Figure 5.1.21: Effect of Feed Rate on Maximum Shear Stress Distribution on the Tool Rake Face (v = 894 m/min, d = 2.5 mm).

(a)

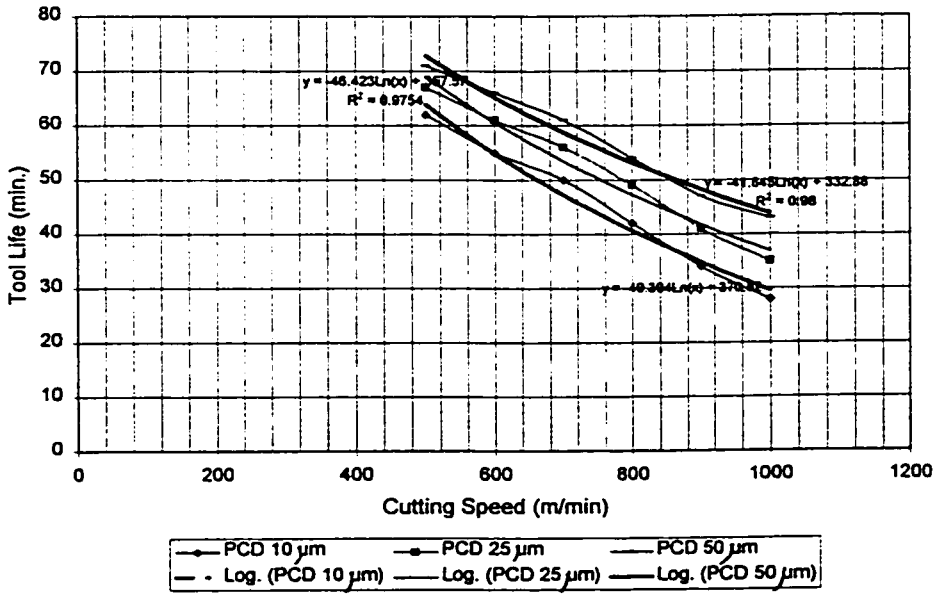

(b)

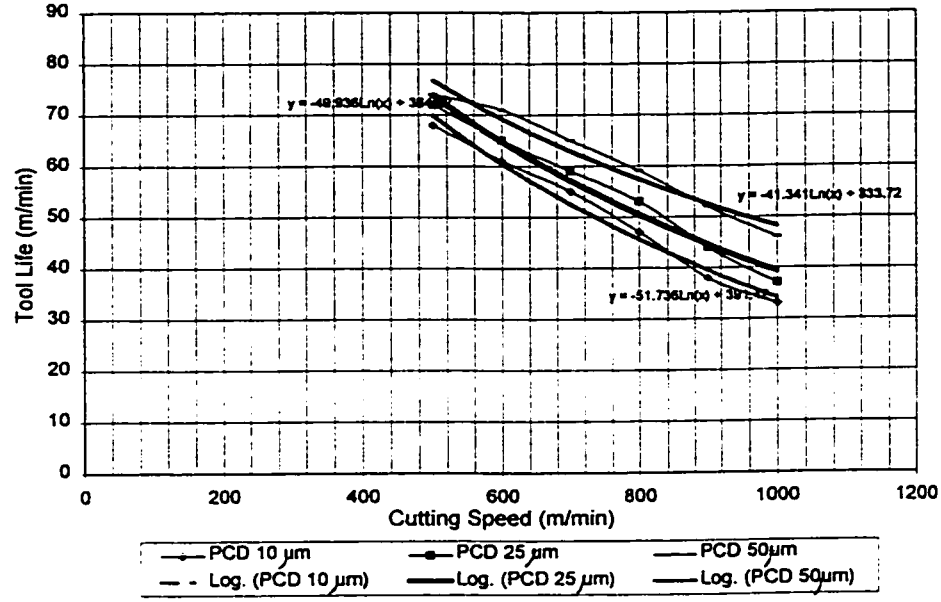

Figure 5.1.22: Variation of the tool life with the cutting speed and feed rate.

(a) f = 0.35 mm/rev; (b) f = 0.55 mm/rev.

5.1.3 Effect of tool geometry

Tool geometry plays an important role in determining the tool wear pattern. As shown in Fig. 5.1.23 reducing the tool nose radius increases the maximum shear stresses significantly.

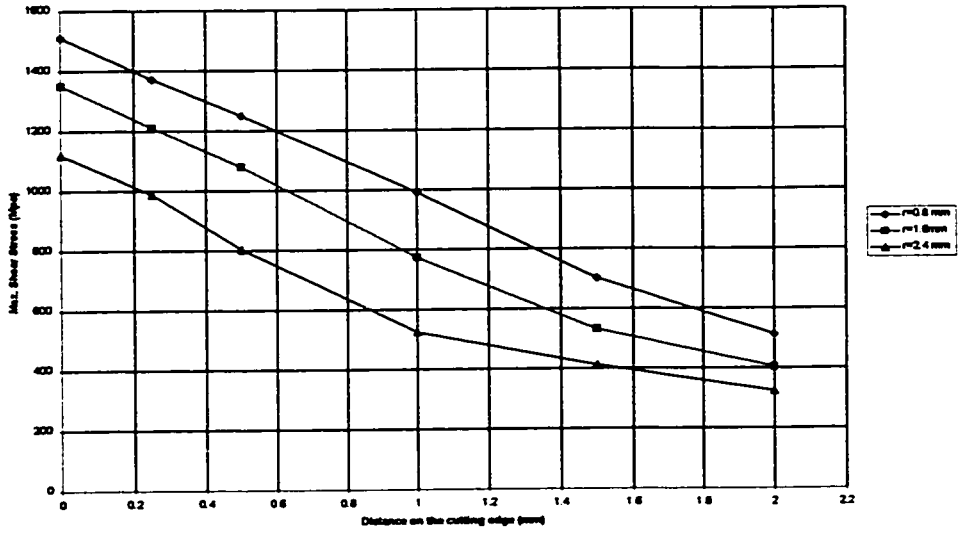

Figure 5.1.23: Effect of Tool Nose Radius on Tool Maximum Shear Stress (v = 894 m/min, f = 0.25 mm/rev., d = 2.5 mm).

The tool rake angle had a profound effect on the wear of PCD tools. Three different rake angles were examined. As can be seen from Fig. 5.1.24a tools with 0^{o} rake angle outperformed positive and negative rake angle tools. A possible reason for the increased flank wear, in the case of negative rake angle, is the higher cutting forces encountered with negative rake angles (Fig. 5.1.24b). Moreover, the produced chips got

caught between the tool and workpiece, causing damage to the tool surface. Tools with positive rake angle showed irregular flank wear and excessive pitting in cutting edge zone, as shown in Fig. 5.1.24c.

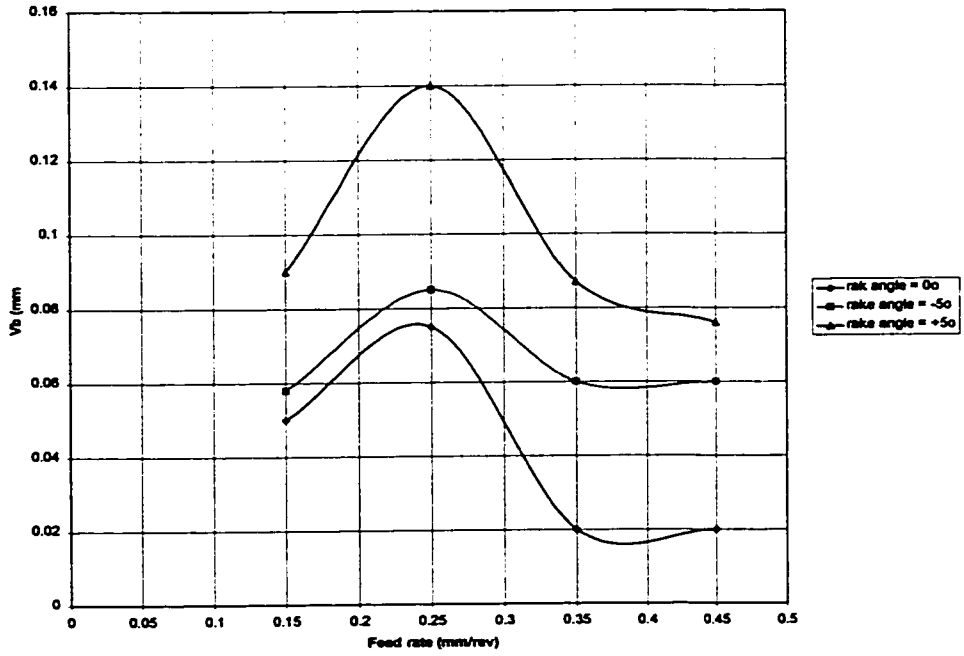

Figure 5.1.24a: Effect of PCD tool rake angle on tool flank wear
(v = 894 m/min, d = 2.5 mm, r = 1.6 mm).

The tool nose radius plays a key role in determining the wear mode of the tool. As the tool nose radius was decreased from 1.6 mm to 0.8 mm, the tool was found to suffer from excessive chipping and crater wear as shown in Fig. 5.1.25a. This tool chipping leads to an increase in cutting forces and flank wear as shown in Fig. 5.1.25b. Tools with small nose radii are, thus, recommended for finishing operations where light cutting parameters are used. Small nose radii are also expected to yield better geometrical accuracy.

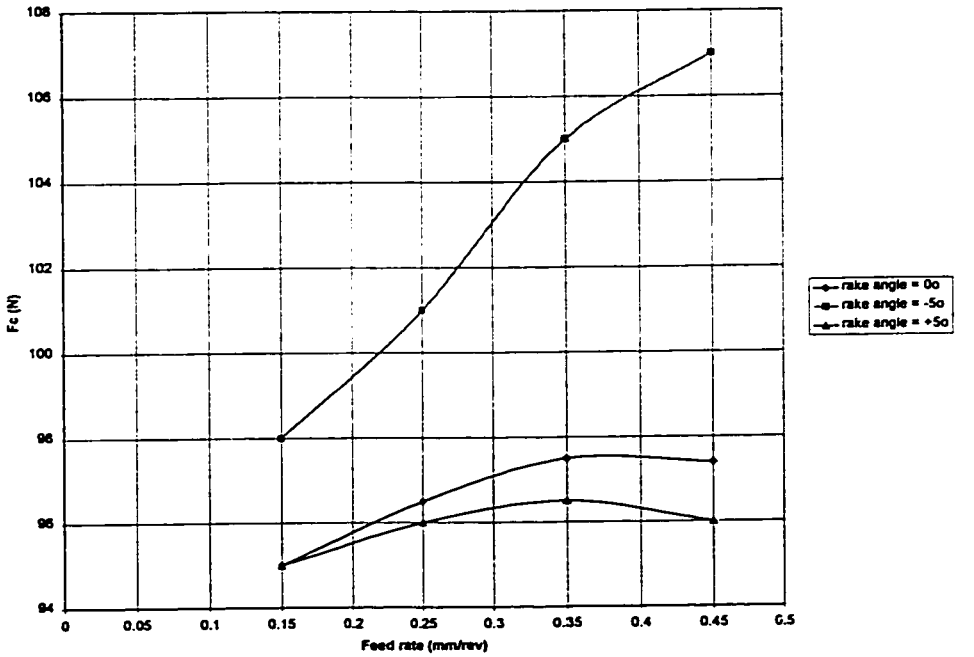

Figure 5.1.24b: Effect of PCD tool rake angle on the cutting forces (v = 894 m/min, d=2.5 mm, r = 1.6mm).

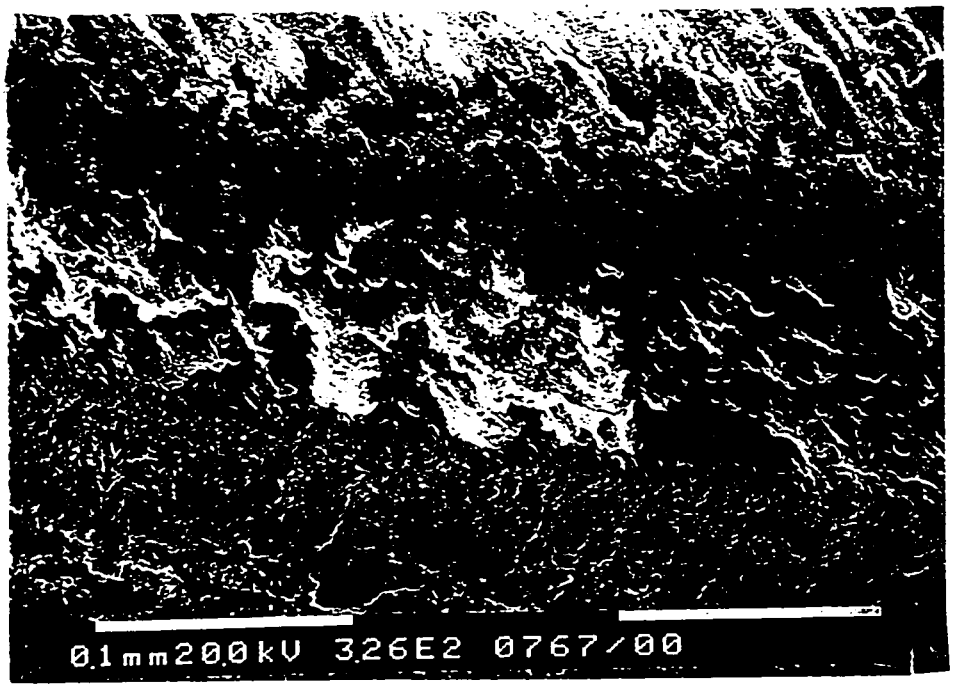

Figure 5.1.24c: SEM image illustrating tool wear by pitting (v = 670 m/min, d = 1.5 mm, f = 0.25 mm/rev., r = 1.6 mm, $\alpha = +5^{o}$)

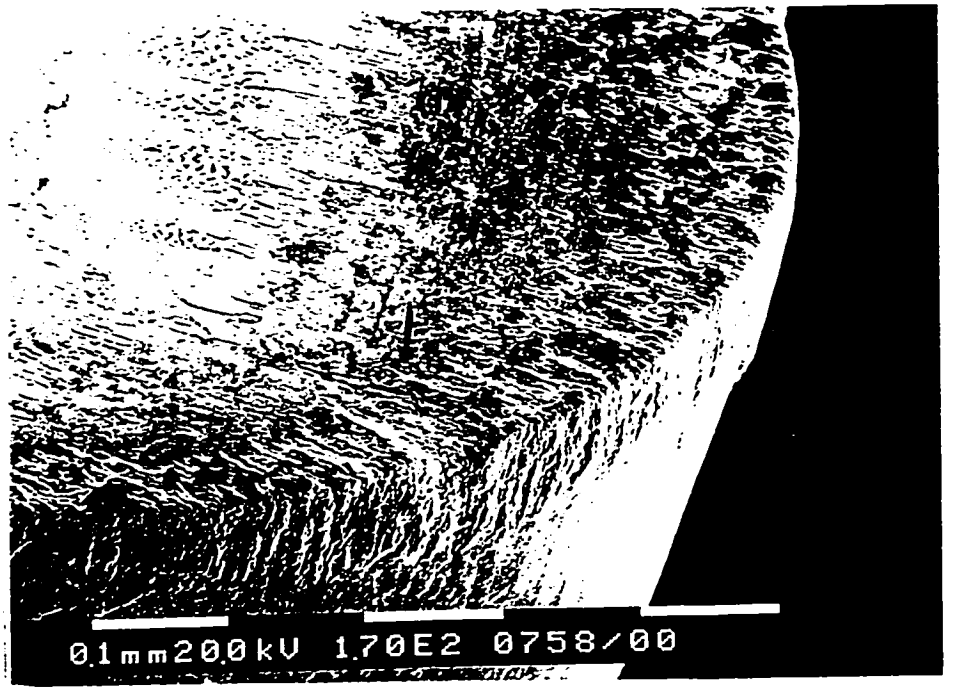

Figure 5.1.25a: SEM image illustrating tool wear by chipping
(v = 894 m/min, d = 1.5 mm, f = 0.35 mm/rev., r = 0.8 mm, $\alpha = 0^{o}$).

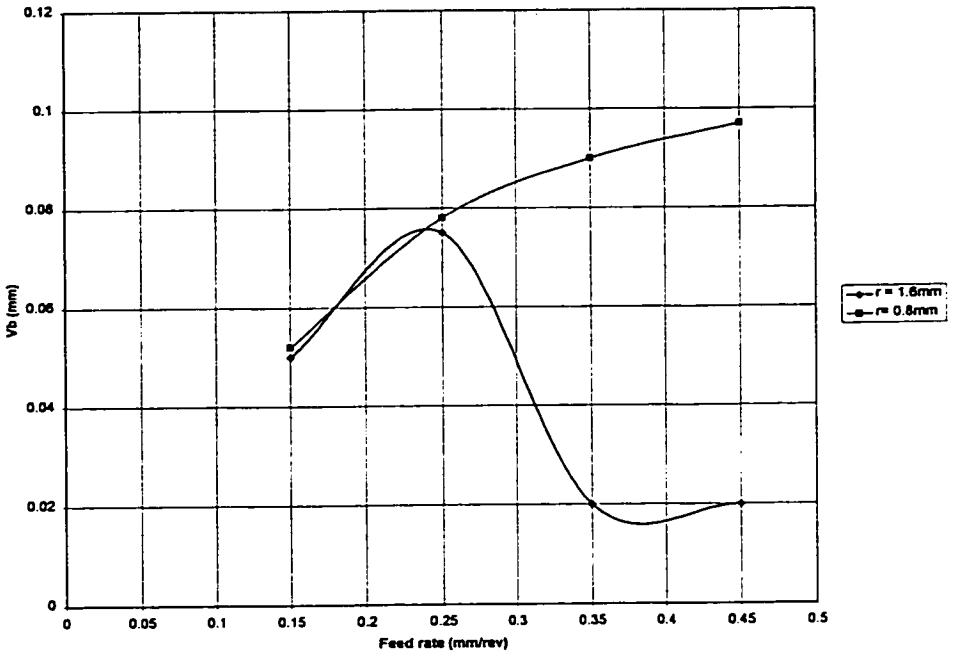

Figure 5.1.25b: Effect of tool nose radius on tool flank wear
(v = 894 m/min, d = 2.5 mm, $\alpha = 0^{o}$).

5.1.4 Stresses on the tool flank

During machining PMMCs the tool's flank is exposed to high stresses that result in high tool flank wear, which has a direct implication on the produced workpiece surface finish, which is discussed in section 5.2. Fig. 5.1.26 and Fig. 5.1.27 show the distribution of the minimum principal stresses and maximum shear stresses on the PCD tool flank face, respectively.

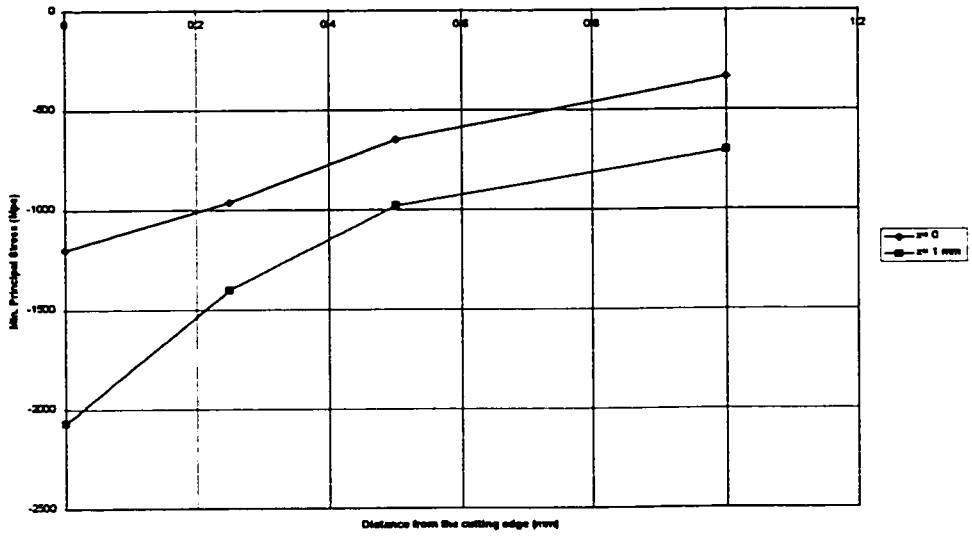

Figure 5.1.26: Minimum principal stress distribution on the tool flank face

(v = 894 m/min, f = 0.45 mm/rev, d = 1.5 mm)

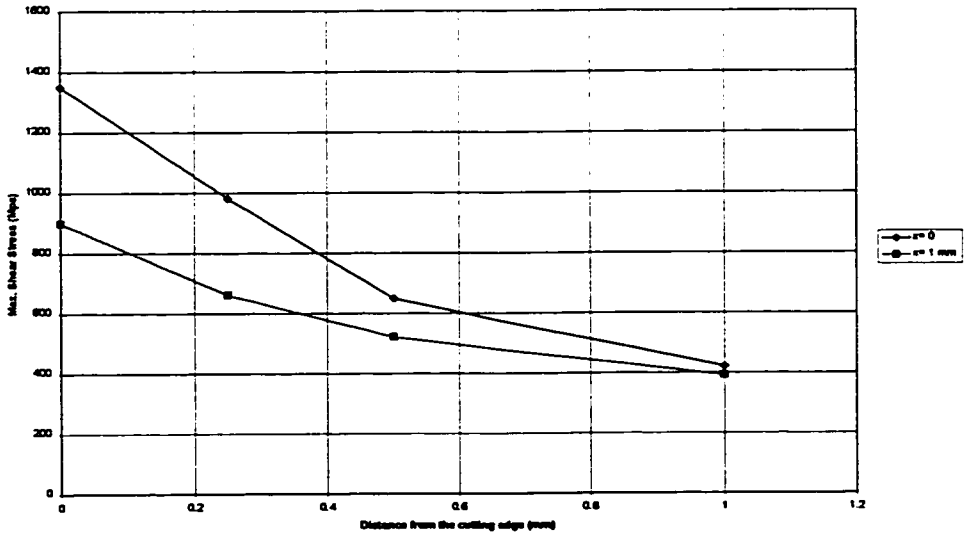

Figure 5.1.27: Maximum shear stress distribution on the tool flank face

(v = 894 m/min, f = 0.45 mm/rev, d =1.5 mm)

As can be seen from Fig. 5.1.26 and Fig. 5.1.27 the tool's tip suffers the highest shear and minimum principal stresses, and thus is expected to weaken and fail by edge chipping or breakage if the tool tip cannot resist the machining loads.

5.2. Machined Workpiece

The finite element prediction of the distribution of minimum principal and maximum shear stresses in the primary and secondary deformation zones are shown in Figures 5.2.1a, 5.2.1b and 5.2.1c and Figures 5.2.2a, 5.2.2b and 5.2.2c, respectively.

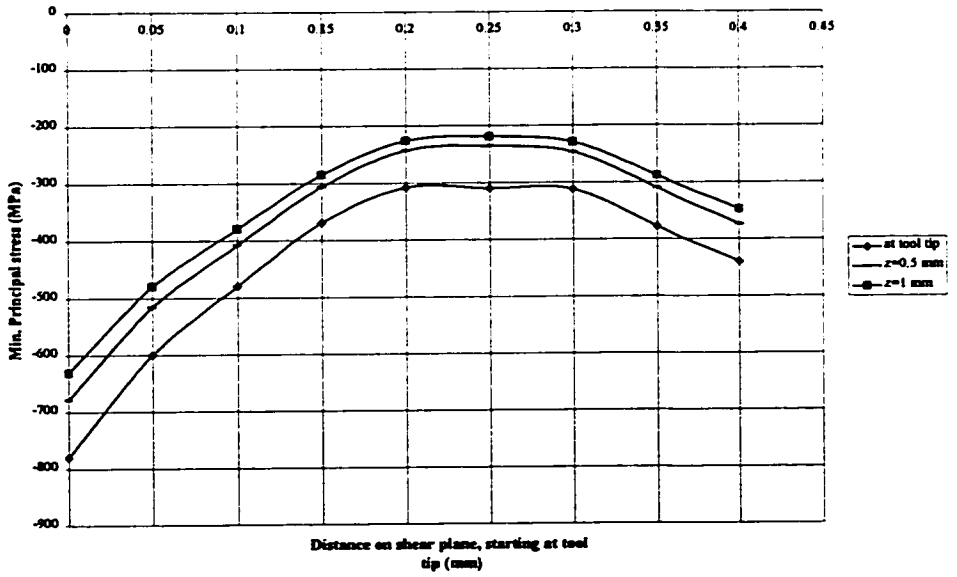

Figure 5.2.1a: Minimum principal stress distribution along the primary deformation zone. (v = 894 m/min., f = 0.35 mm/rev., d = 2.0mm., α=0°, r = 1.6 mm).

In the primary deformation zone, the minimum principal stresses (Fig. 5.2.1a) are compressive, where the stresses are at peak at the two ends of the chip being formed; -780 MPa occurs near the tool tip and -440 MPa occurs at the top layer of the chip. A low compressive stress of about –308 MPa occurs in the middle of the deformation zone. The distribution of the shear stresses shows a peak of 510 MPa near the tool tip and a uniform distribution (from 410 to 440 MPa) up to the top layer of the chip, and hence the matrix material in the chip fails by shearing. The hydrostatic stresses (Fig. 5.2.3) are compressive and reach –550 MPa at the tool tip. These high compressive hydrostatic

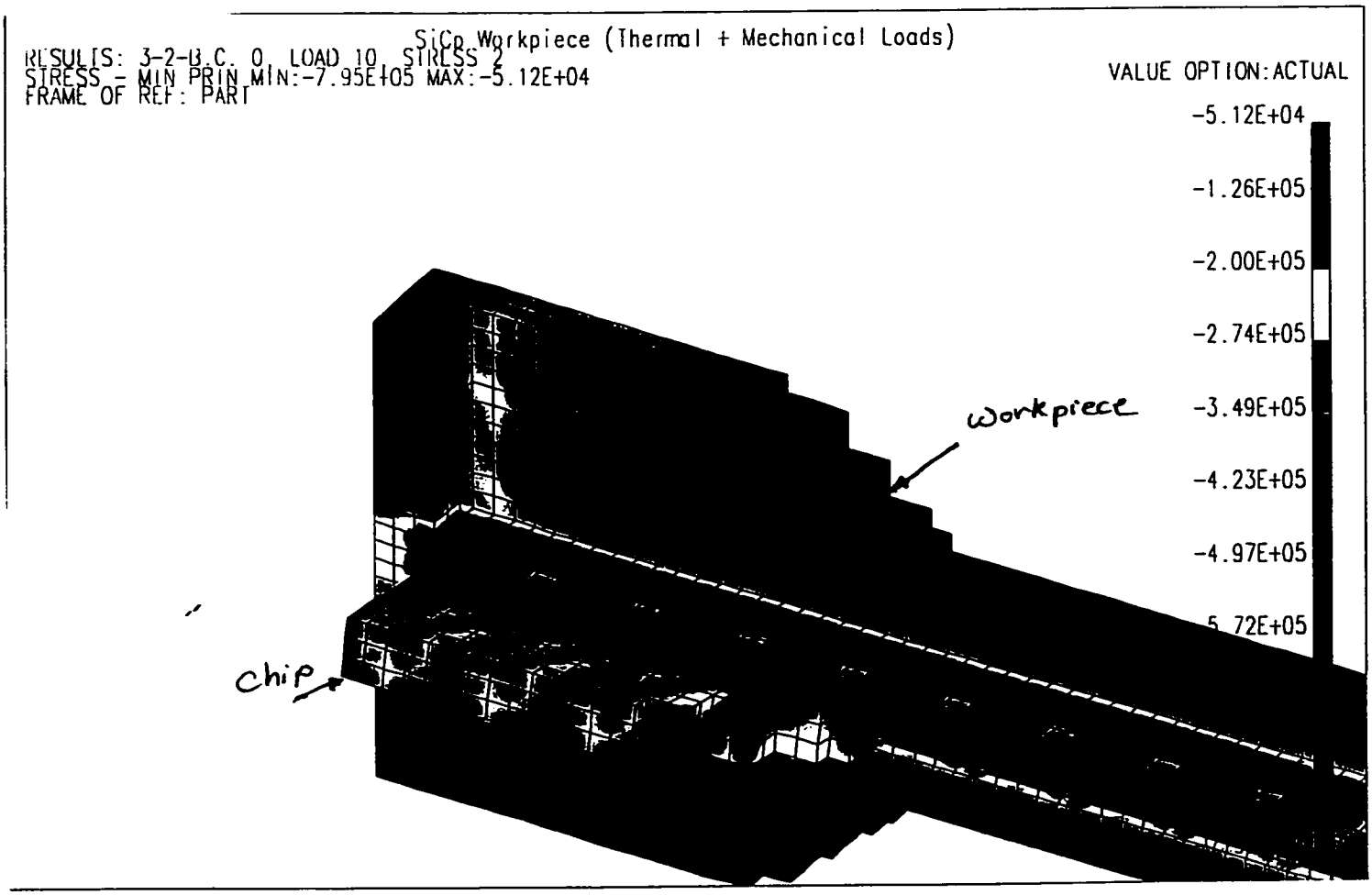

Figure 5.2.1b: Minimum principal stress distribution along the primary deformation zone (v = 894m/min., f = 0.15 mm/rev., d = 1.5 mm., α=0°, r = 1.6 mm).

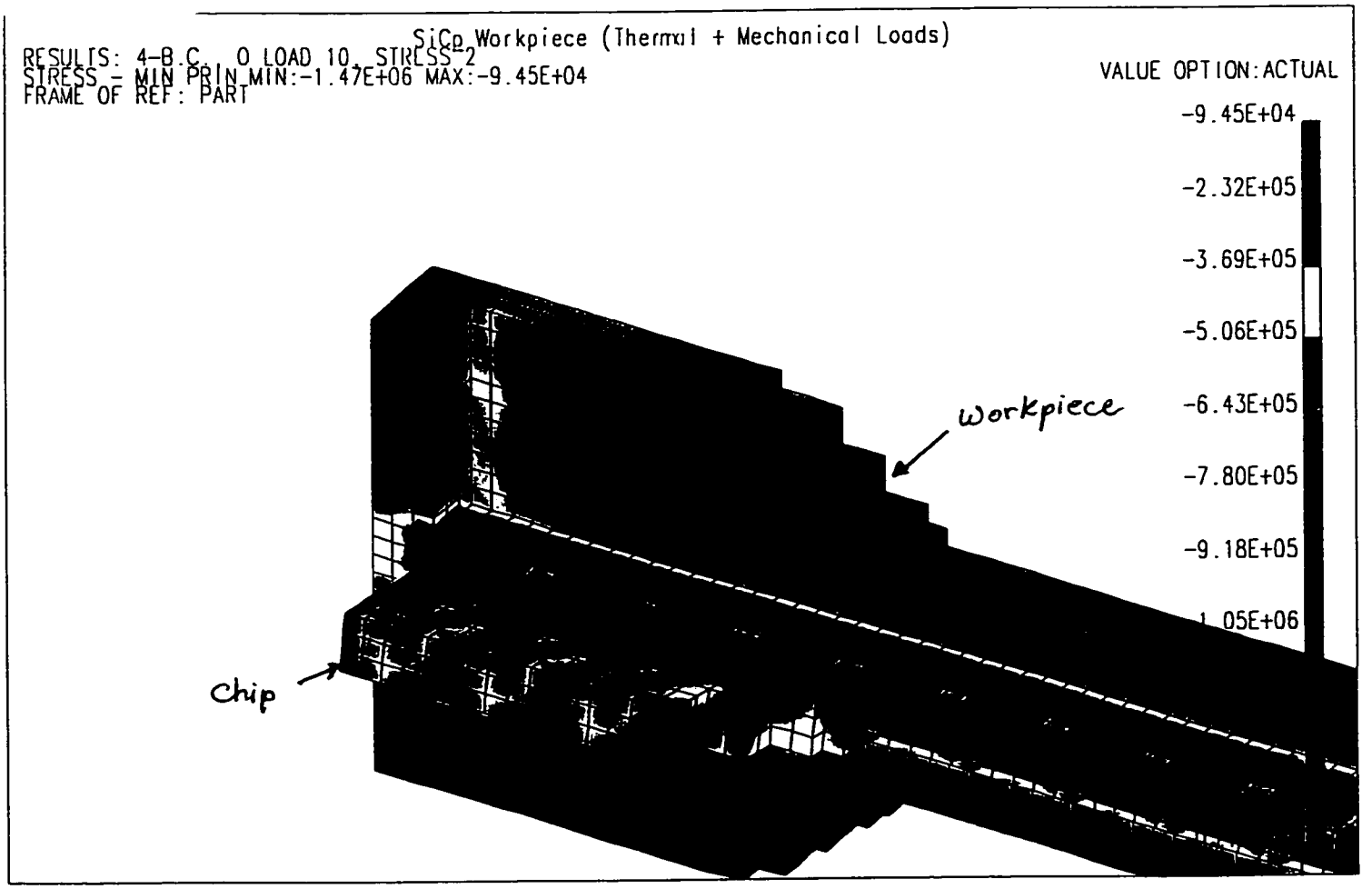

Figure 5.2.1c: Minimum principal stress distribution along the primary deformation zone (v = 1200 m/min., f = 0.35 mm/rev., d = 1.5 mm., α=0°, r = 1.6 mm).

stresses could easily cause the fracture of the matrix, yet the SiC reinforcing particles remain elastic. These predictions are in agreement with the SEM observations shown in Figures 5.2.4a, 5.2.4b, 5.2.4c and 5.2.4d.

These results also indicate that the chip formation mechanism is due to the combined effect of shearing of the matrix and the joining of voids (formed around the SiC particles, where high compressive stresses occur) to form cracks.

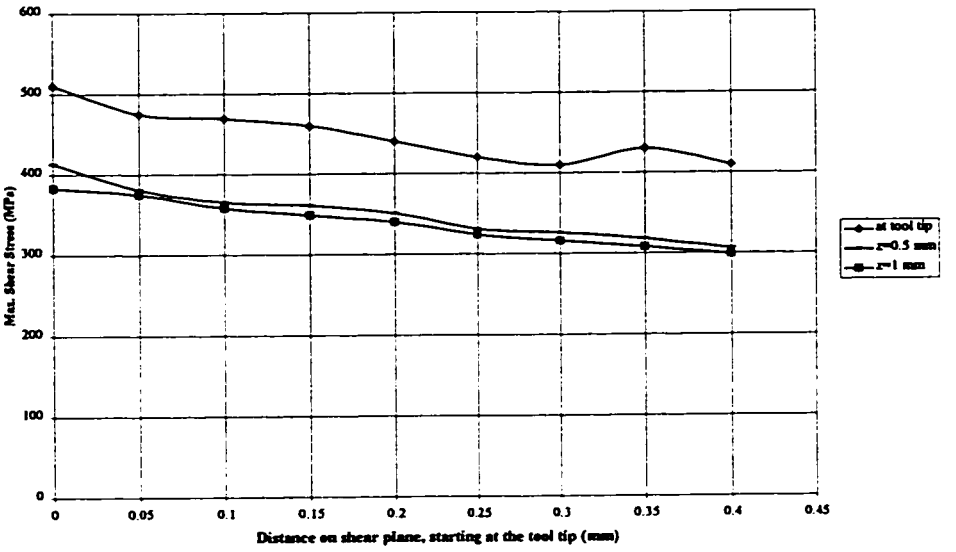

Figure 5.2.2a: Shear stress distribution along the primary deformation zone (v = 894 m/min., f = 0.35 mm/rev., d = 2.0 mm., $\alpha = 0^{o}$, r = 1.6 mm).

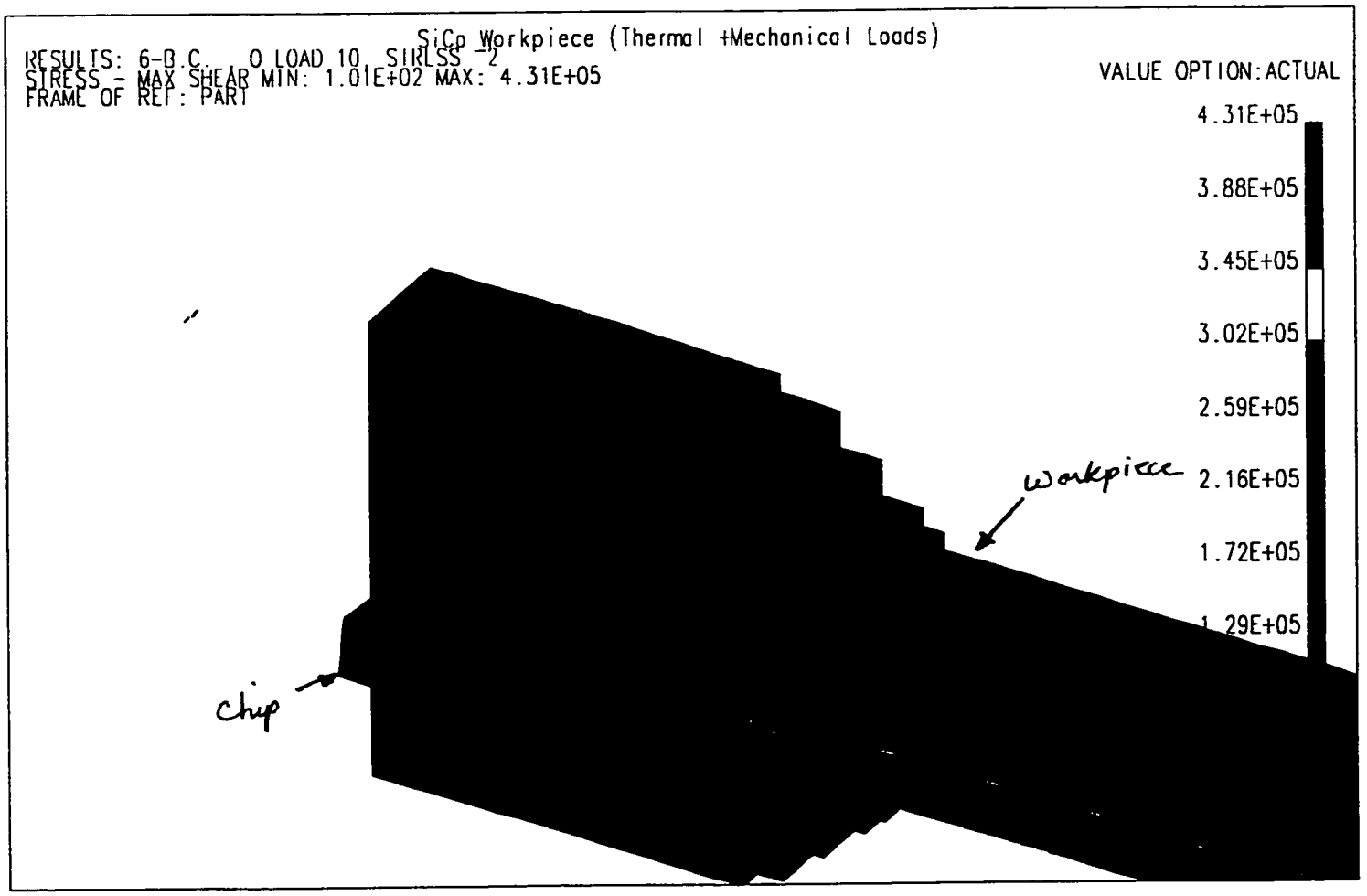

Figure 5.2.2b: Maximum shear stress distribution along the primary deformation zone ($v = 894$ m/min., $f = 0.15$ mm/rev., $d = 1.5$ mm., $\alpha = 0^{o}$, $r = 1.6$ mm).

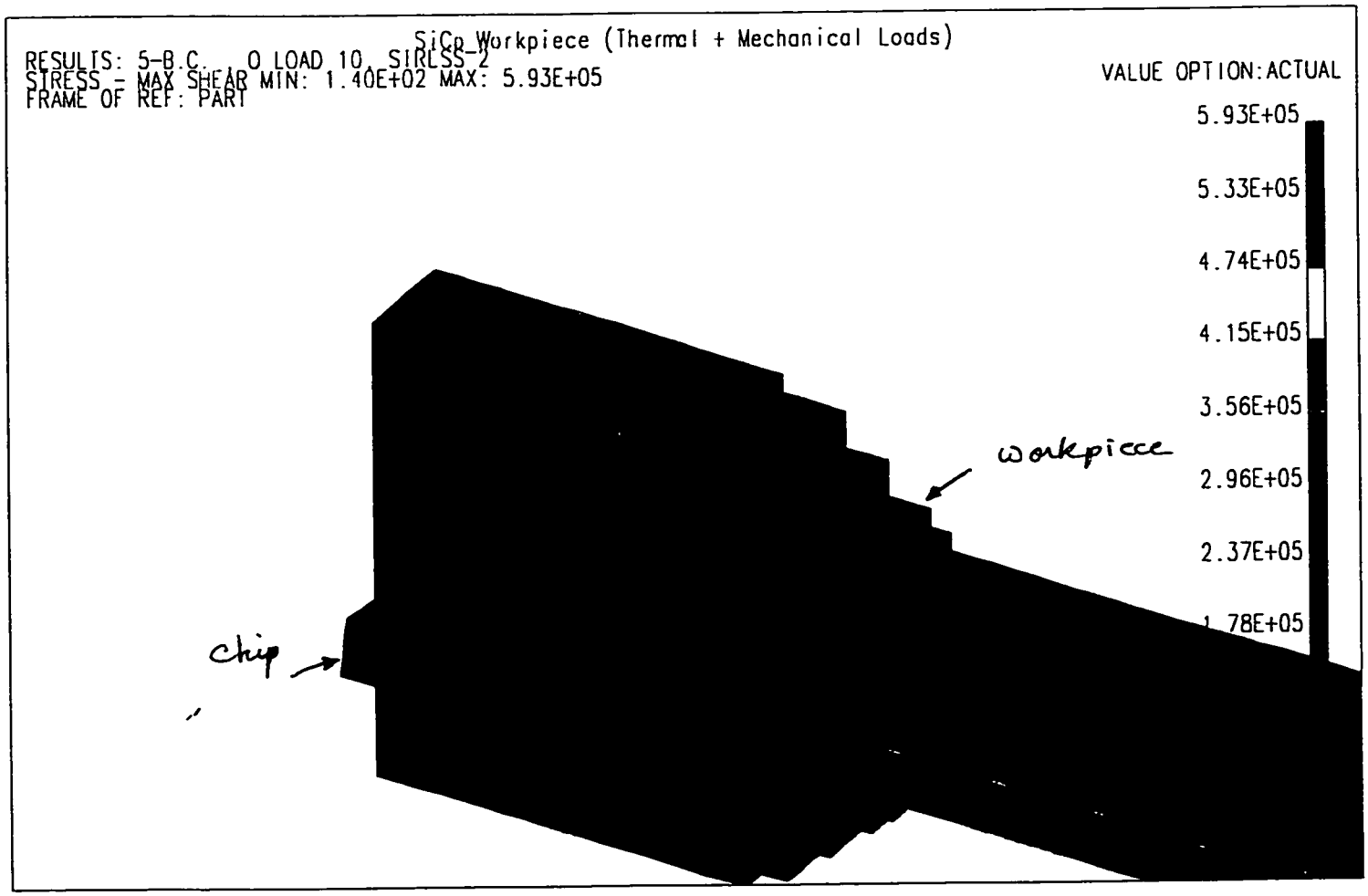

Figure 5.2.2c: Maximum shear stress distribution along the primary deformation zone ($v = 1200$ m/min., $f = 0.35$ mm/rev., $d = 1.5$ mm., $\alpha = 0^{o}$, $r = 1.6$ mm).

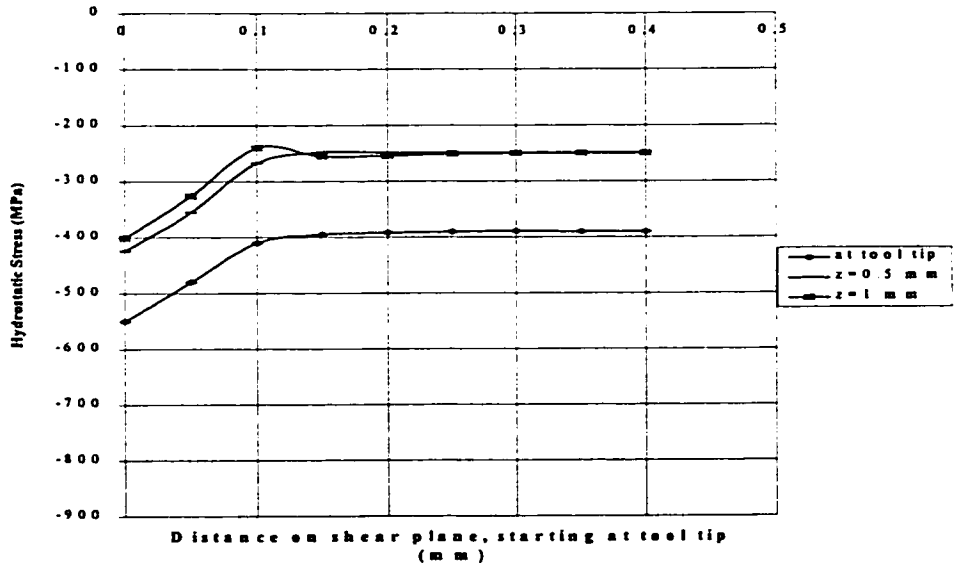

Figure 5.2.3: Hydrostatic stress distribution along the primary deformation zone
(v = 894 m/min., f = 0.35 mm/rev., d = 2.0 mm., $\alpha = 0^{o}$, r = 1.6 mm)

Generally, the chip undergoes two types of deformation (Fig. 5.2.5 through Fig. 5.2.8). The first is due to large compressive stresses and the second is large bending stresses, resulting from the restriction by the tool face. Both stresses act simultaneously leading to the breakage of the chip at the end. The matrix material in the chip experiences large plastic strains; both along the shear plane and through the secondary deformation zone. The plastic deformation in the matrix leads to the fracture of the matrix and hence affect the load transfer process to the particles. The silicon carbide particles, on the other hand, do not experience any plastic deformation. Thus, another possible failure mode could be excessive plastic deformation of the matrix material around the non-deforming reinforcement particles, leading to the creation of voids around the particles as shown in Fig. 5.2.4b.

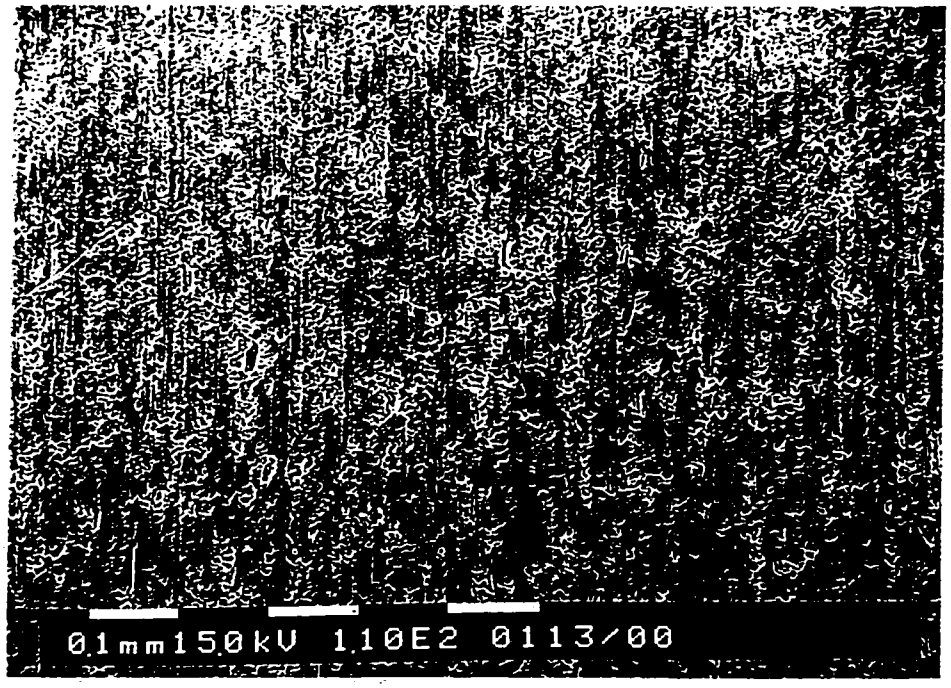

Figure 5.2.4a: SEM images of the chip showing typical topography

(v = 894 m/min., f = 0.35 mm/rev., d = 2.0 mm., $\alpha = 0^{o}$, r = 1.6 mm)

Figure 5.2.4b: SEM images of the chip showing voids formed around SiC particles

(v = 894m/min., f = 0.35 mm/rev., d = 2.0 mm., $\alpha = 0^{o}$, r = 1.6 mm)

Figure 5.2.4c: SEM images of the chip showing pulled out SiC particles

(v = 894 m/min., f = 0.35 mm/rev., d = 2.0 mm, $\alpha = 0^{o}$, r = 1.6 mm)

Figure 5.2.4d: SEM images of the chip showing fractured or crushed SiC particles

(v = 894 m/min., f = 0.35 mm/rev., d =2.0 mm, $\alpha = 0^{o}$, r = 1.6 mm)

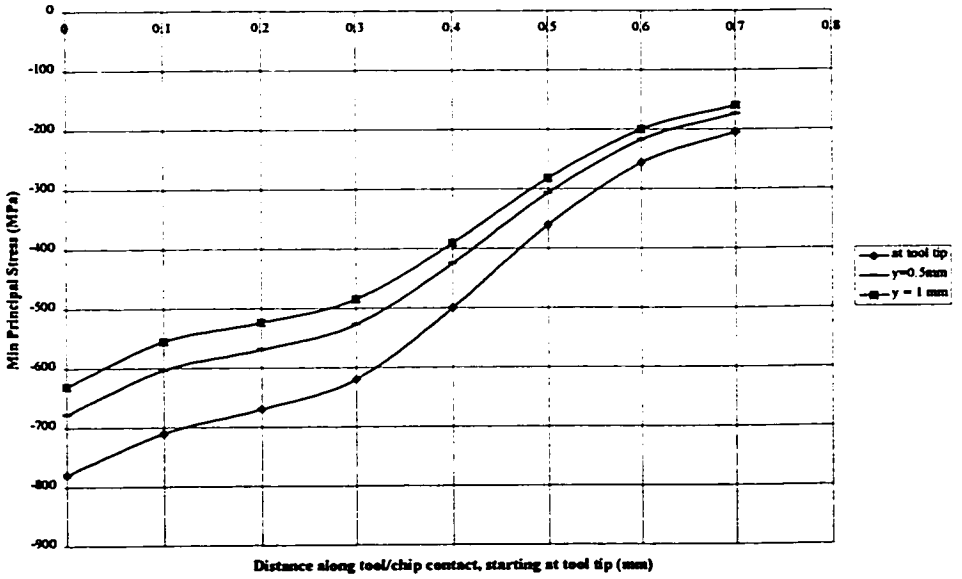

Figure 5.2.5: Minimum principal stress distribution along the secondary deformation zone. (v = 894 m/min., f = 0.45 mm/rev., d = 1.5 mm , $\alpha = 0^{o}$, r = 1.6 mm)

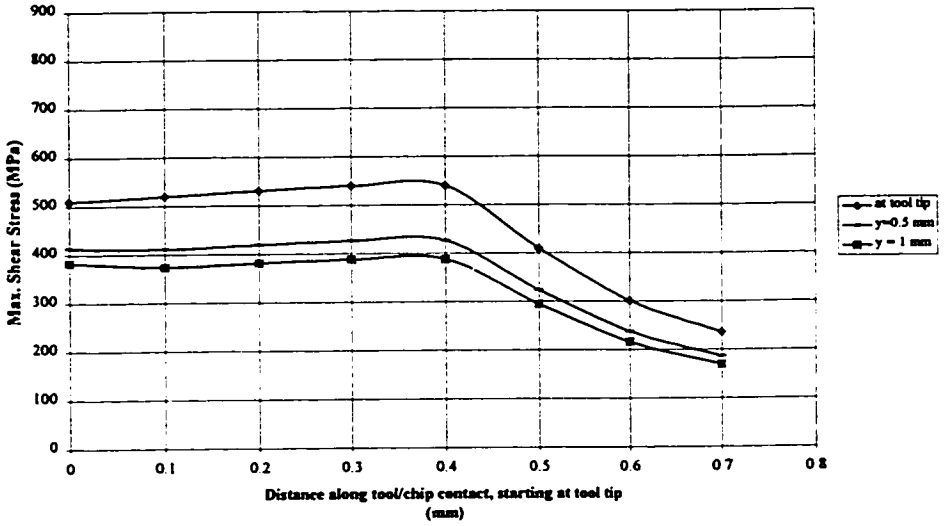

Figure 5.2.6: Shear stress distribution along the secondary deformation zone (v = 894 m/min., f = 0.45 mm/rev., d = 1.5 mm., $\alpha = 0^{o}$, r = 1.6 mm)

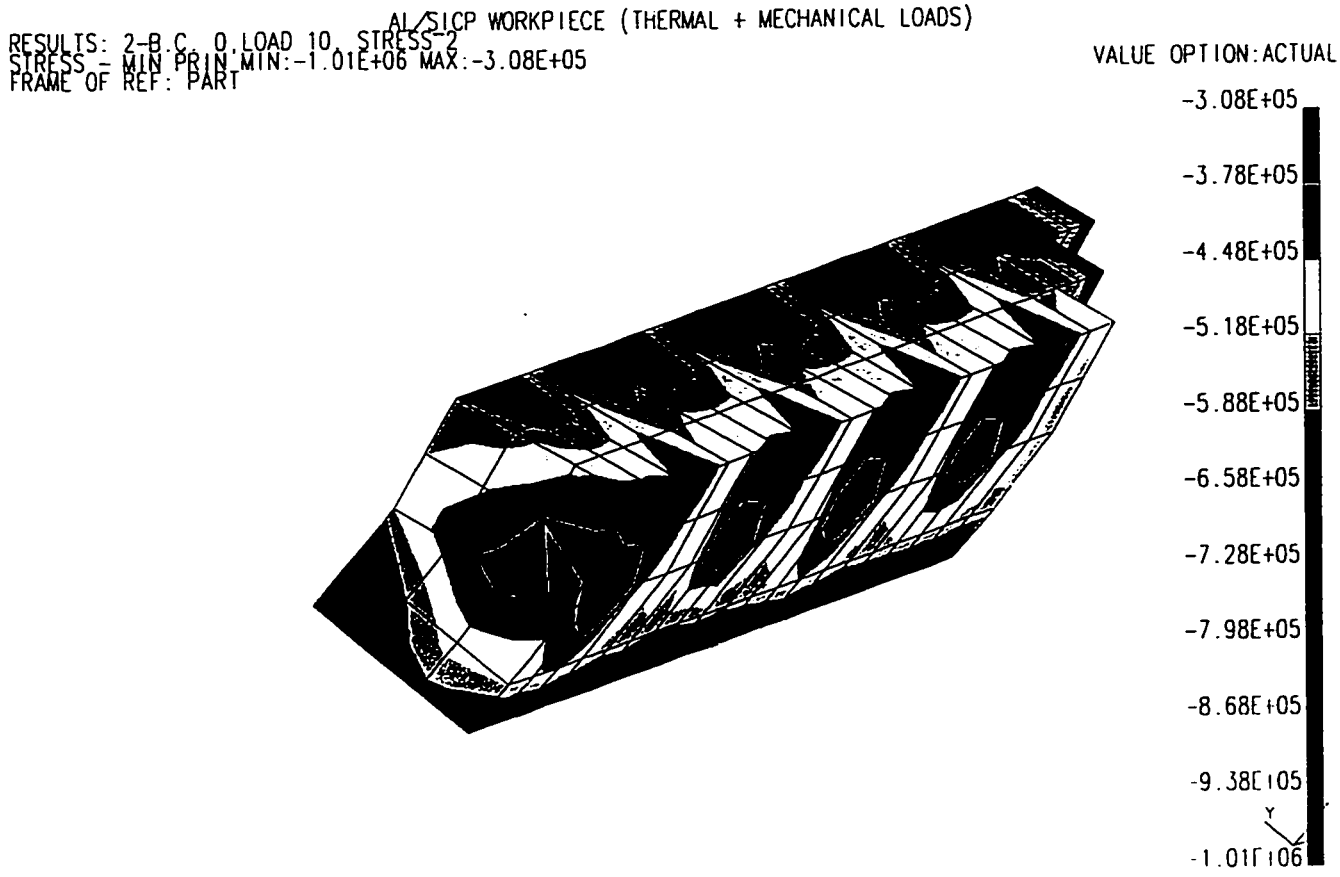

Figure 5.2.7a: Minimum principal stresses induced in the chip

(v = 894 m/min, f = 0.3 mm/rev, d = 2.5 mm, r = 1.6 mm)

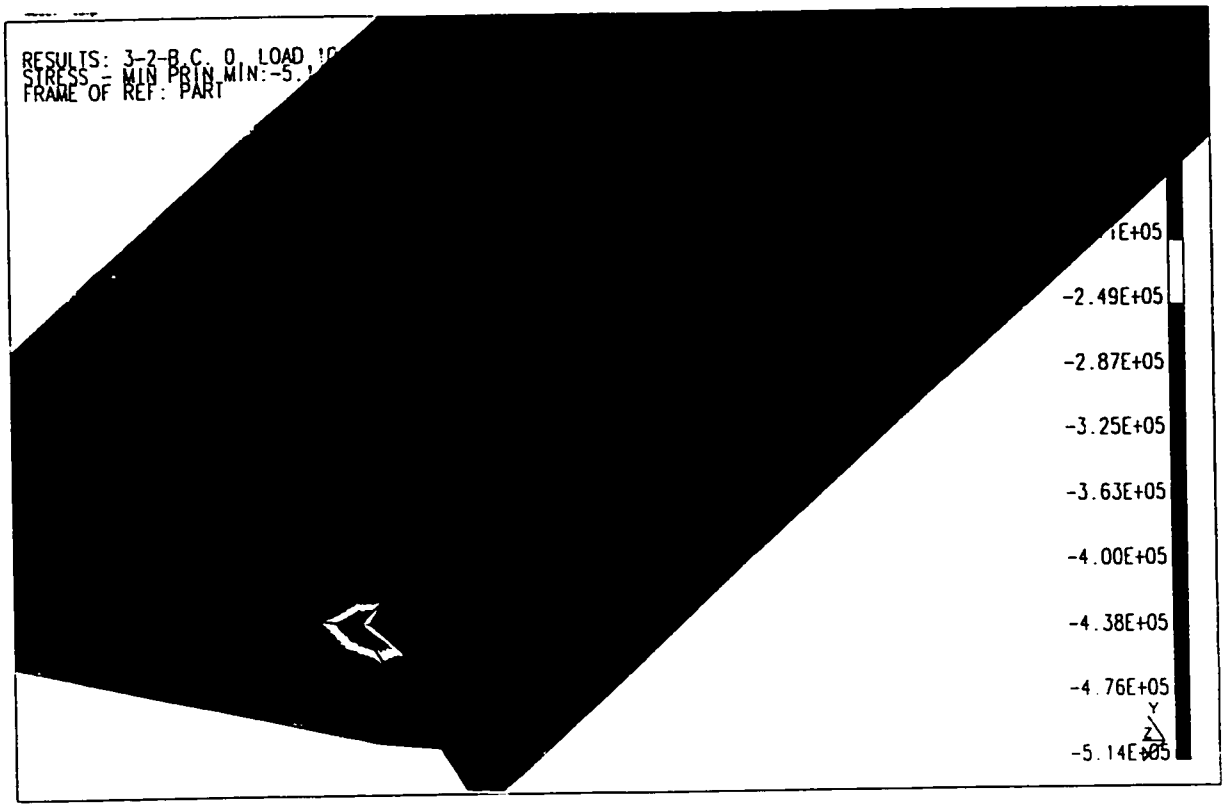

Figure 5.2.7b: Minimum principal stresses induced in the chip

(v = 670 m/min, f = 0.15 mm/rev, d = 1.5 mm, r = 1.6 mm)

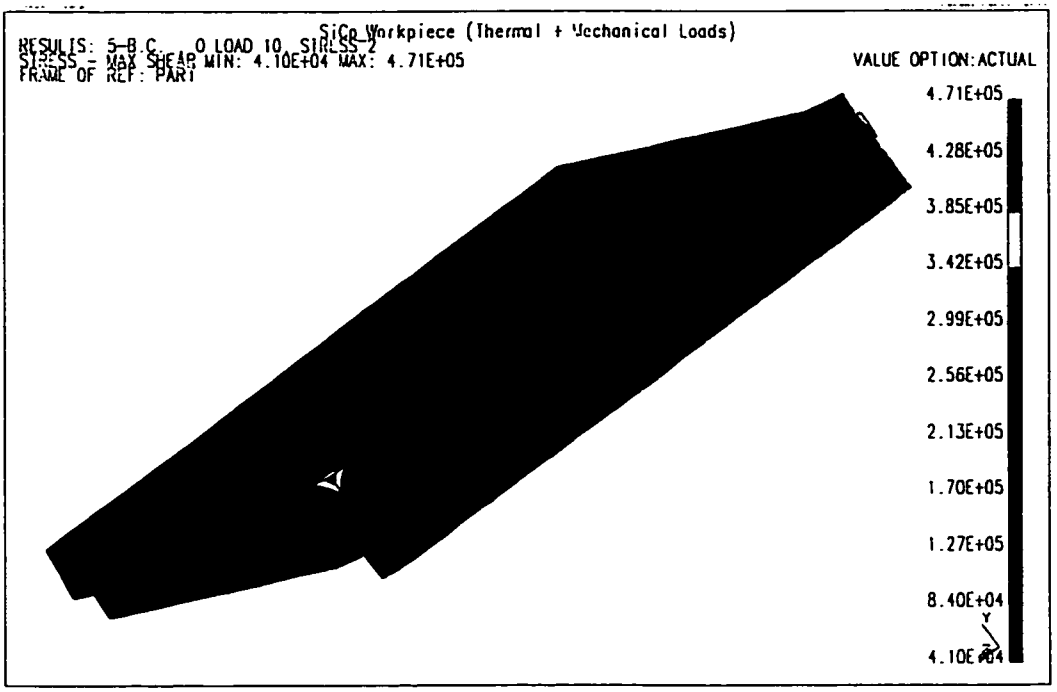

Figure 5.2.8a: Maximum shear stress distribution in the chip

(v = 894 m/min, f = 0.3 mm/rev, d = 2.5 mm, r = 1.6 mm)

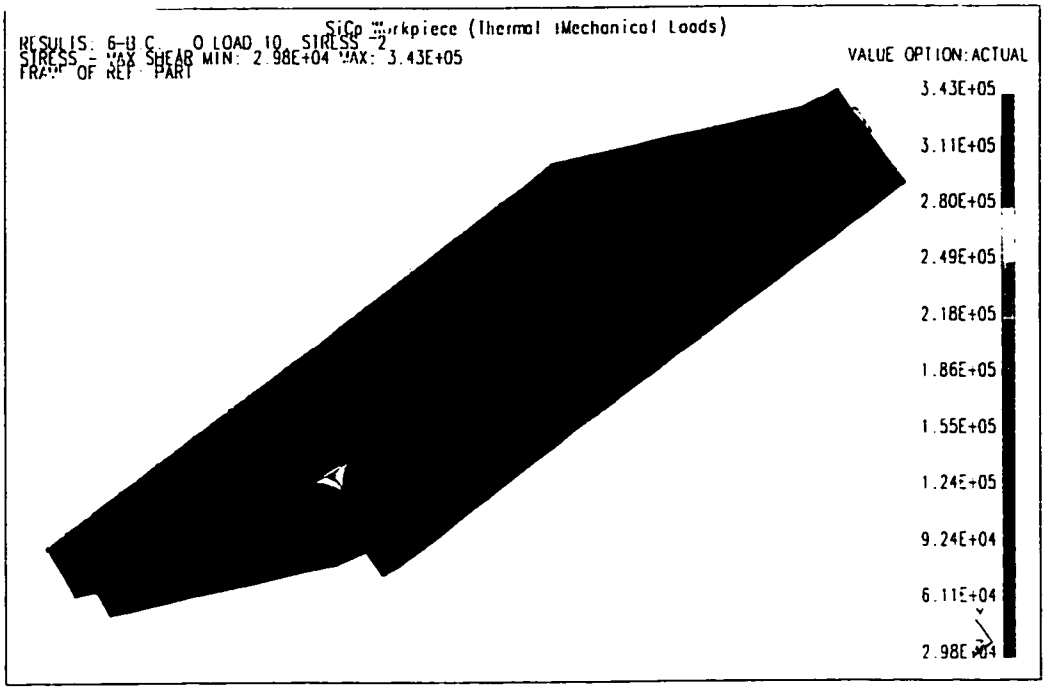

Figure 5.2.8b: Maximum shear stresses induced in the chip

(v = 670 m/min, f = 0.15 mm/rev, d = 1.5 mm, r = 1.6 mm)

The surface being machined experiences large plastic strains (Fig. 5.2.9), due to the thermal effects combined with rubbing of the tool flank. These plastic strains continue to decrease beneath the machined surface. The finite element predictions explain the increase in the microhardness beneath the machined surface, as shown in Fig. 5.2.10a. Beneath the machined surface the matrix material strain hardens. The finite element model, however, reveals peak plastic strains at the top layer, which is not in agreement with the microhardness measurements. This could be attributed to the ploughing and cracking of the SiC particles in the top surface. It should also be mentioned that the results of the TEM analysis indicated an increase in the dislocation density as shown in Fig. 5.2.10b and Fig. 5.2.10c, due to plastic working of the matrix material.

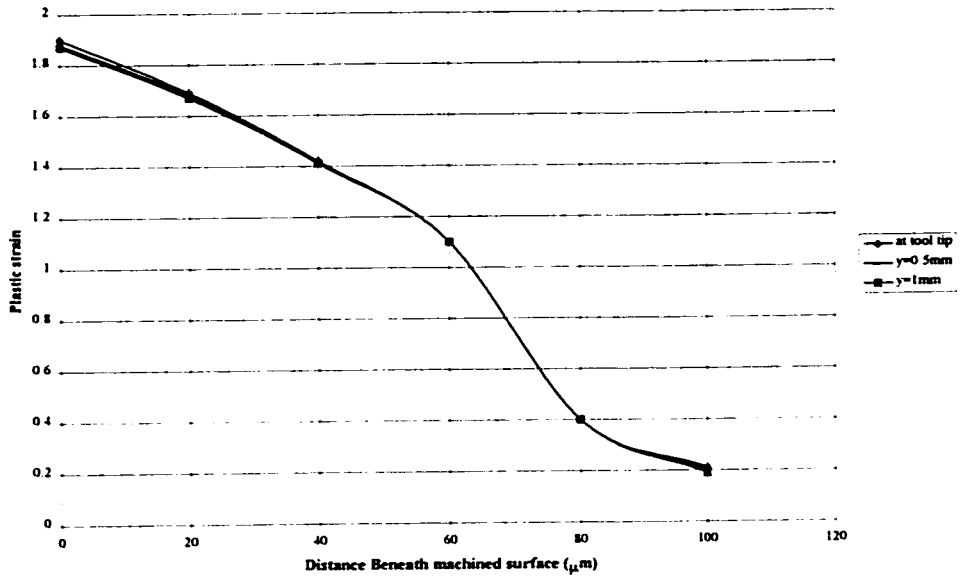

Figure 5.2.9: Plastic Strain distribution beneath the machined surface ($v = 894$ m/min., $f = 0.45$ mm/rev., $d = 1.5$ mm., $\alpha = 0^o$, $r = 1.6$ mm).

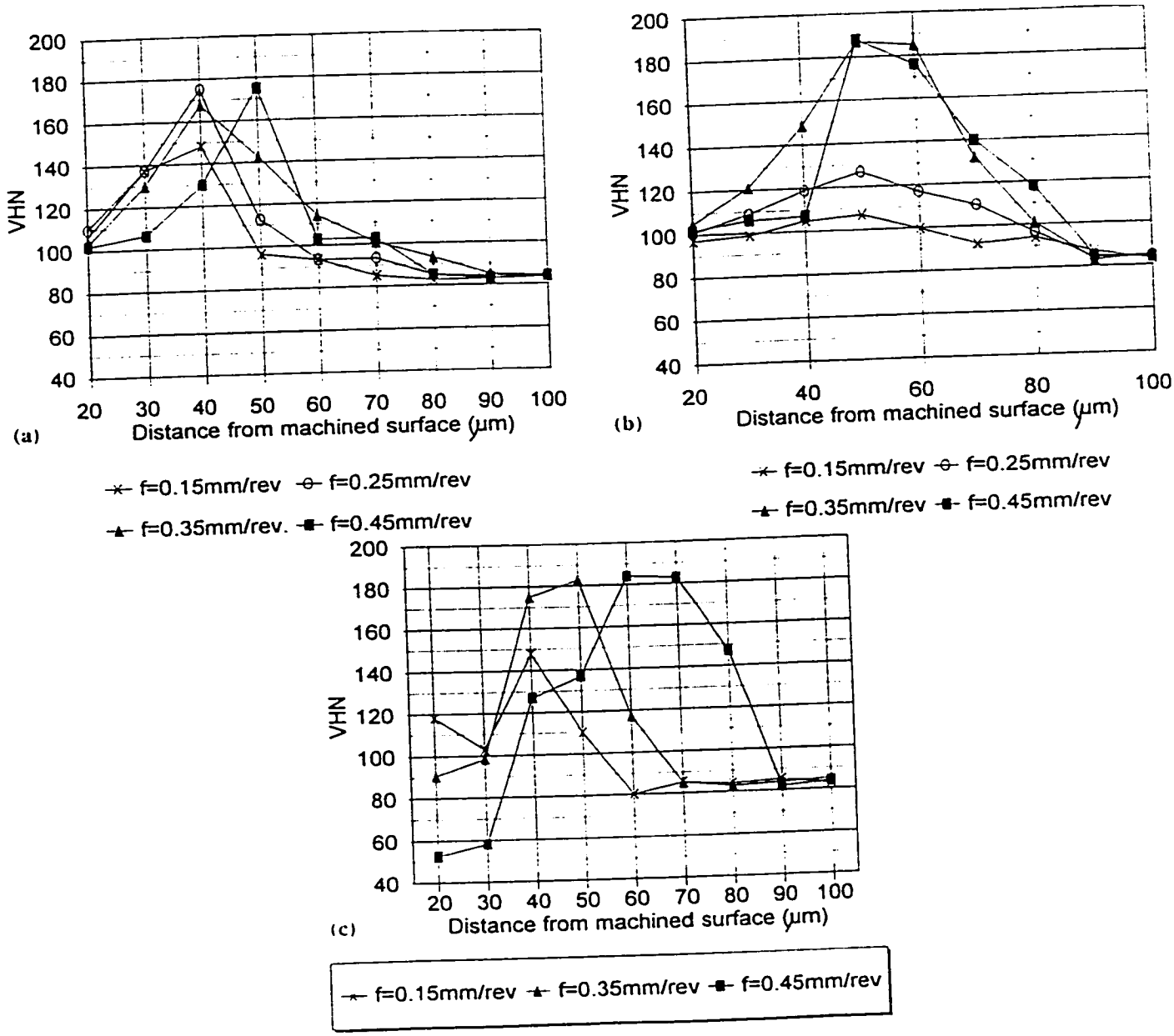

Figure 5.2.10a: Vickers microhardness measurements beneath the machined surface

(v = 894 m/min., f = 0.45 mm/rev., d =1.5 mm., $\alpha = 0^{o}$, r = 1.6 mm) .

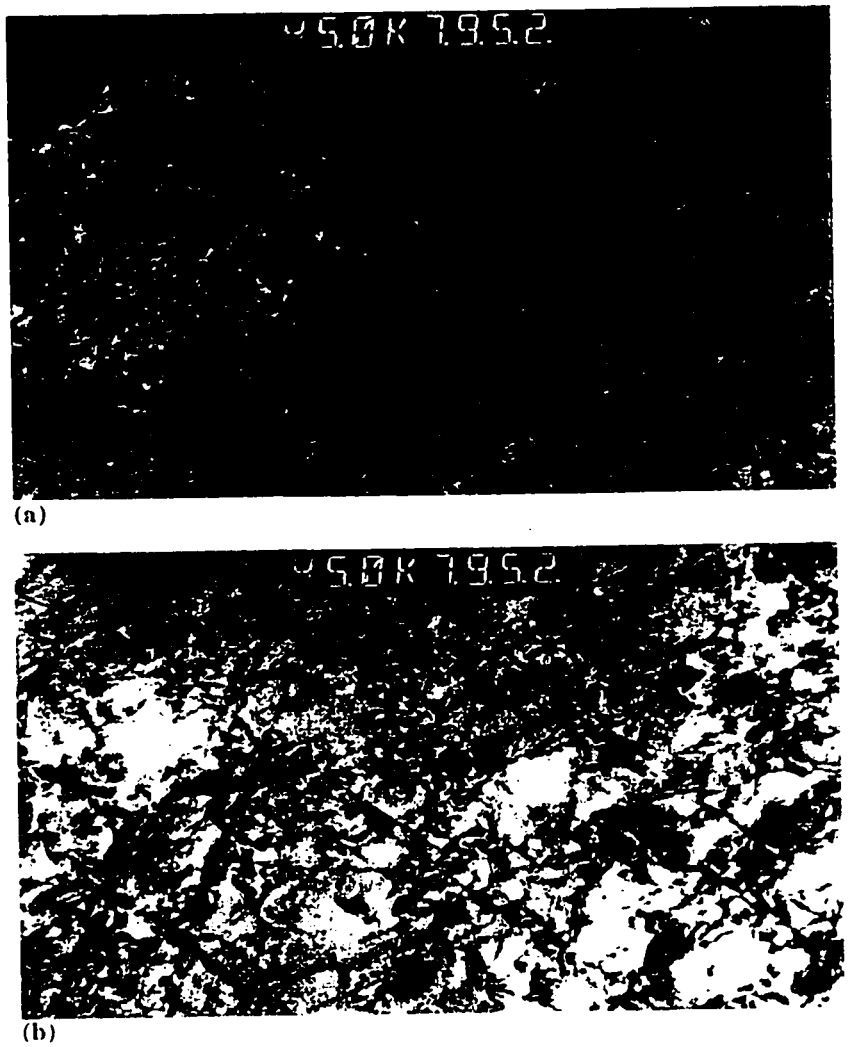

Figure 5.2.10b: TEM micrographs of cross-sectional samples showing the matrix grains and dislocation substructure (v = 670 m/min, f = 0.45 mm/rev, d = 2.5 mm, r = 1.6mm, $\alpha = 0^{o}$) (b) 50 μm below machined surface; (c) 58 μm below machined surface.

The Von Mises effective stress shows a similar trend as shown in Fig. 5.2.11a and Fig. 5.2.11b The hydrostatic stress also peaks at the top surface and continues to decrease beneath the top surface, as shown in Fig. 5.2.12. These stresses are also high enough to cause matrix failure.

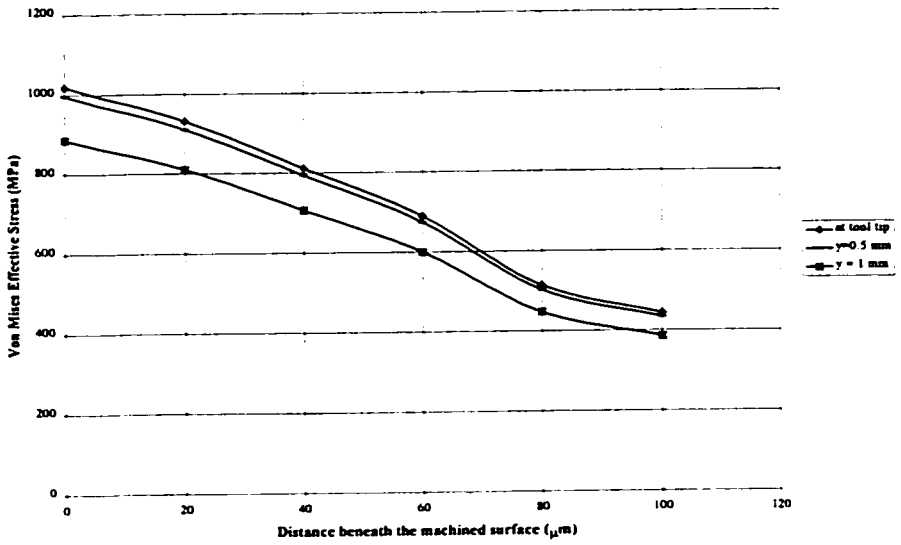

Figure 5.2.11a: Von Mises effective stress distribution beneath the machined surface (v = 894 m/min., f = 0.25 mm/rev., d = 2.5 mm., $\alpha = 0^{o}$, r = 1.6 mm).

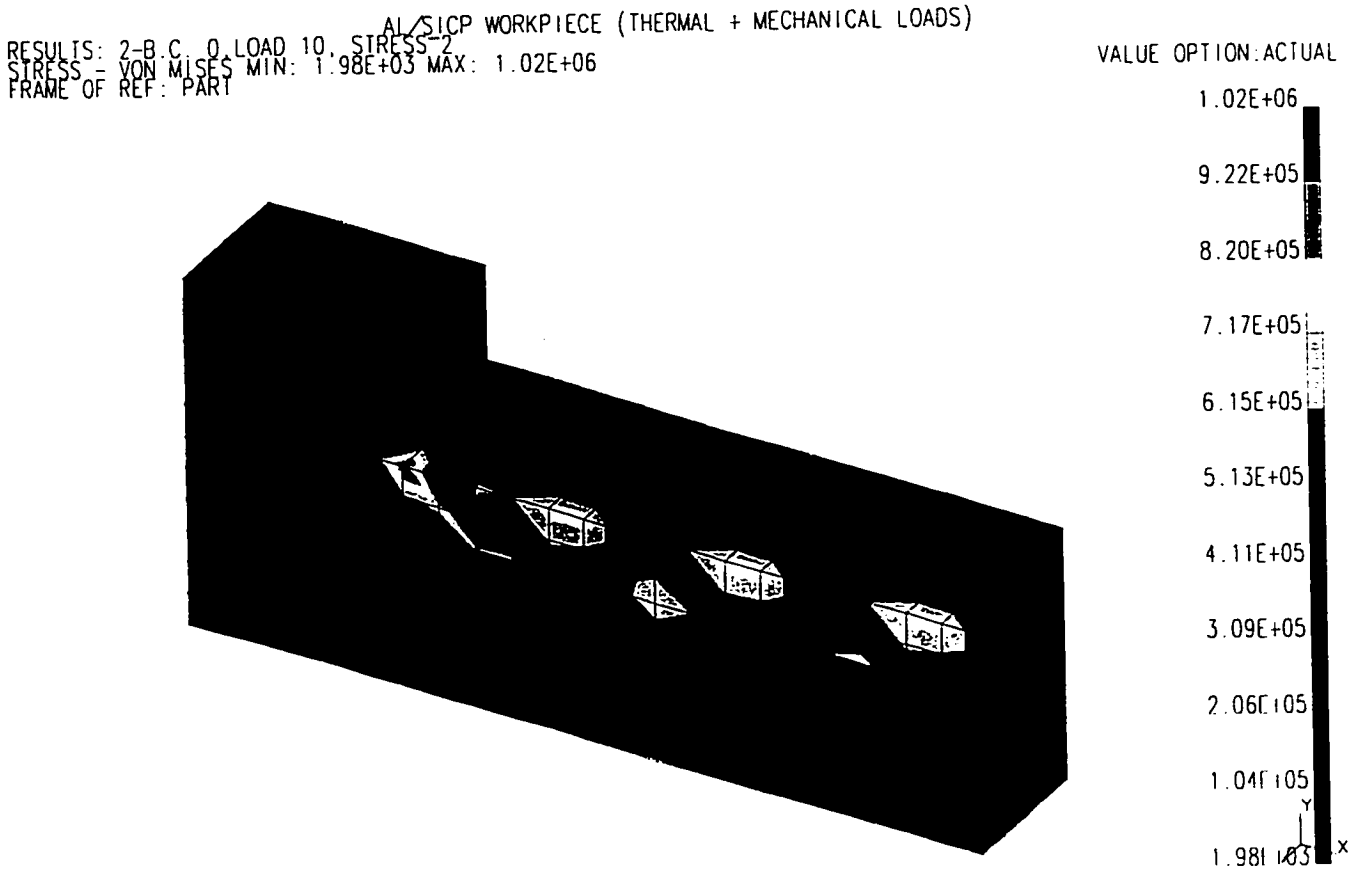

Figure 5.2.11b: Von Mises effective stress distribution beneath the machined surface

(v = 894 m/min., f = 0.35 mm/rev., d = 2.5 mm., $\alpha = 0^{o}$, r = 1.6 mm).

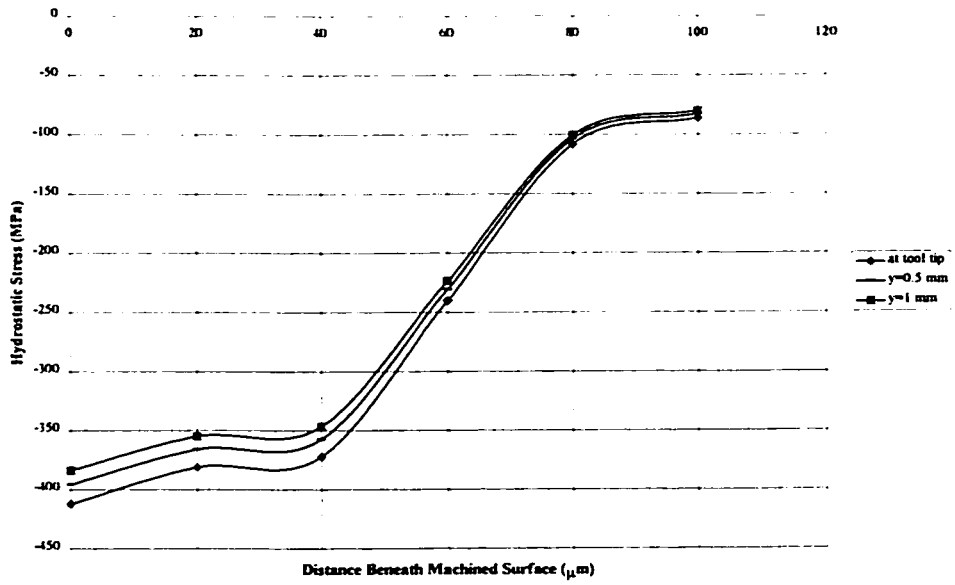

Figure 5.2.12: Hydrostatic stress distribution beneath the machined surface (v = 894 m/min., f = 0.25 mm/rev., d = 1.5 mm., $\alpha = 0^{o}$, r = 1.6 mm).

Increasing the cutting speed results in an increase in the hydrostatic stresses (Fig. 5.2.13), whereas increasing the feed rate does not result in an appreciable increase in the hydrostatic stresses (Fig. 5.2.14). This is attributed to the reduced tool wear at high feed rates [147]. Thus, increasing the feed rate does not result in an increase in the subsurface damage.

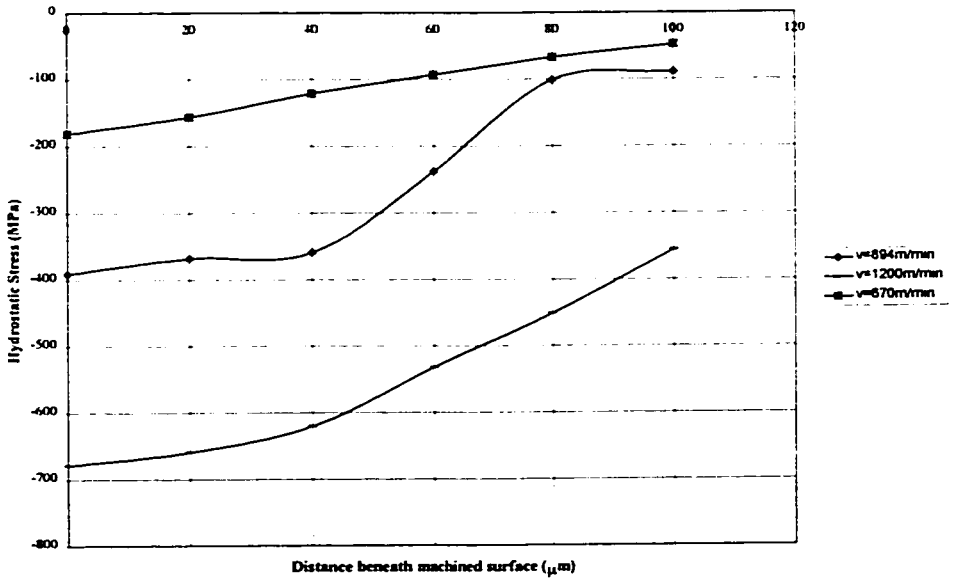

Figure 5.2.13: Effect of cutting speed on the hydrostatic stresses in machined subsurface (f = 0.25 mm/rev., d = 1.5 mm., $\alpha = 0^{o}$, r = 1.6 mm).

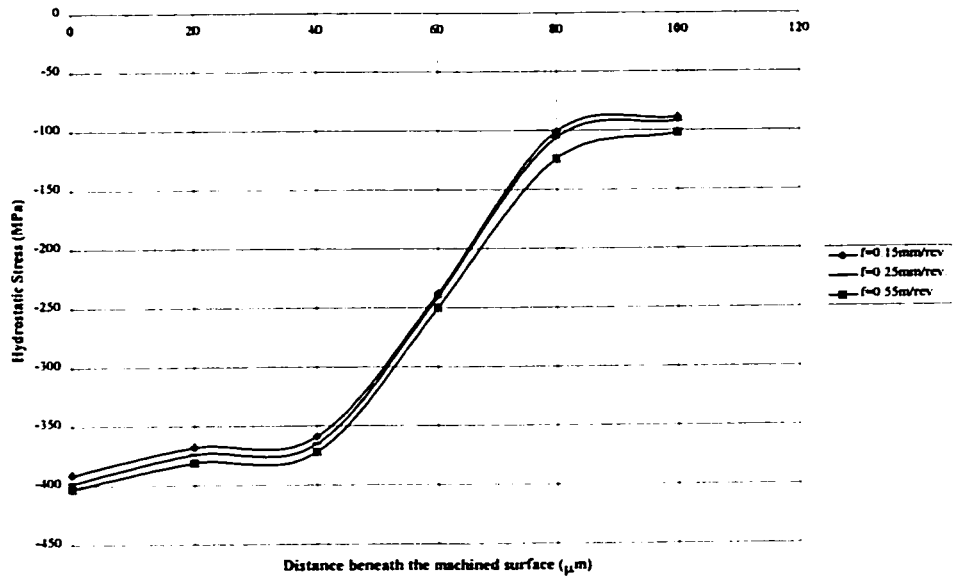

Figure 5.2.14: Effect of feed rate on the hydrostatic stresses in machined subsurface (v = 894 m/min., d = 1.5 mm., $\alpha = 0^{o}$, r = 1.6 mm).

Figure 5.2.15a and 5.2.15b indicate the existence of grooves on the machined surface. These grooves could be attributed to SiC particles being pulled out of the composite material and they get dragged along the machined surface causing scratches. Oxidized aluminium could have the same effect. Further, since the wear mechanism of the tool is abrasion, pulled out PCD grains could also be responsible for the formation of these grooves.

Figure 5.2.16a and 5.2.16b show the influence of the various cutting parameters on the surface roughness R_{max}. A common feature in Fig. 5.2.16a and Fig. 5.2.16b is the reduction in the surface roughness with the increase in the feed rate. This effect is attributed to the reduction in the tool flank wear with the increase in the feed rate. Figure 5.2.16b shows that surface roughness improves at higher cutting speeds (v) and depth of cut (d). This could be attributed to the stable built-up edge, which is formed and protects the tool from wear by abrasion. On the other hand, Fig. 5.2.16b indicates that employing low feed rates and high depths of cut results in a poor surface quality, which is attributed to the unstable BUE formed.

Finally, tool geometry affects the surface roughness of the machined product. Negative rake angles led to higher surface roughness (Fig. 5.2.17a). This is attributed to the clogging of the hot chips between the tool and the machined surface, causing severe damage to the workpiece surface finish. A similar trend was also observed when a clamped chip breaker was used. In the latter case R_{max} increased to 12.2 μm (f = 0.45 mm/rev, v= 894 mm/rev), as shown in Fig. 5.2.17b. At feed rates less than 0.35 mm/rev. and speeds less than 894 m/min PCD tools with small tool nose radius (r = 0.8 mm) produced better surface finish than PCD tools with nose radius of 1.6 mm (Fig. 5.2.17c).

However, at higher feed rates and/or cutting speed, tools with radius 1.6 mm outperformed the tools with a nose radius of 0.8 mm. This is attributed to the increased edge chipping of tools with small nose radius.

(a)

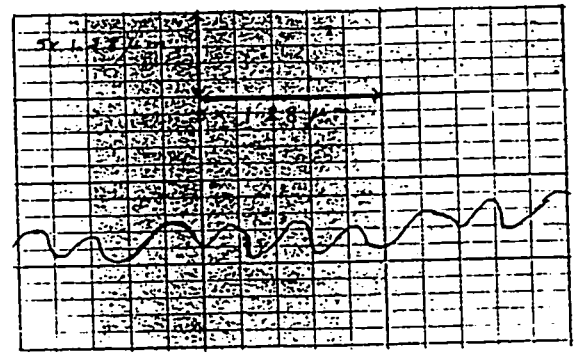

(b)

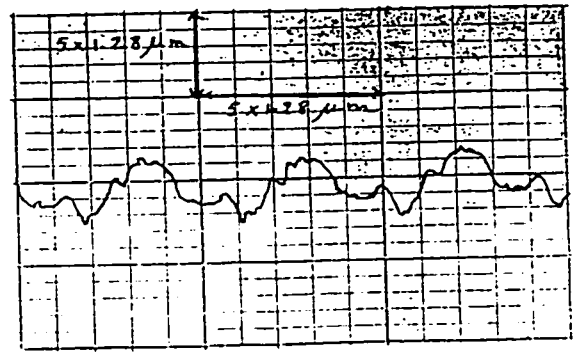

Figure 5.2.15: Surface roughness profiles of machined surfaces

(v = 894 m/min, f = 0.15 mm/rev., r = 1.6 mm, $\alpha = 0^{o}$). (a) d = 1.5 mm; (b) d = 2.5 mm.

(a)

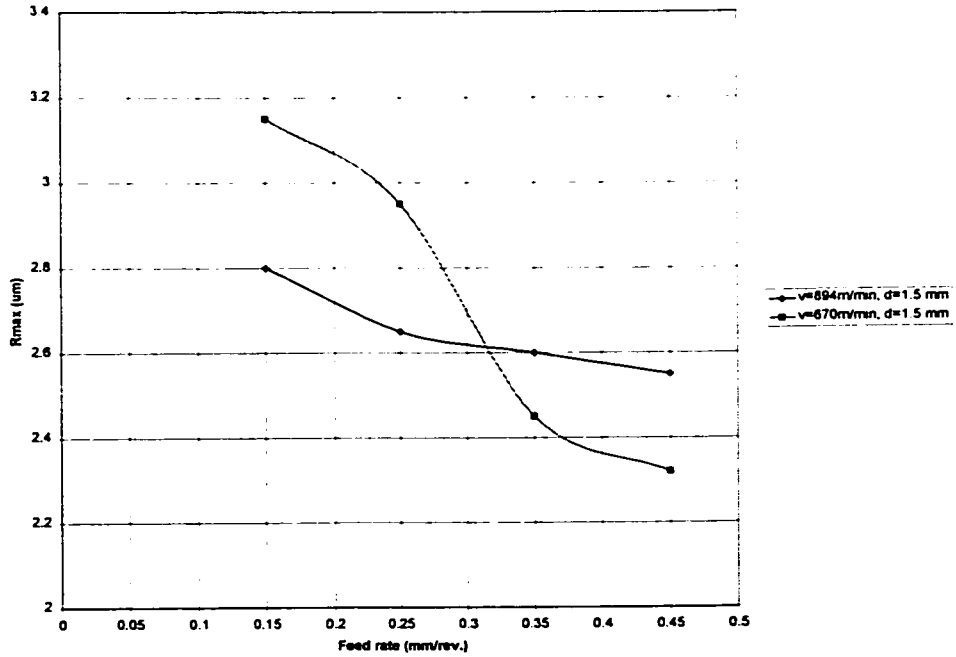

(b)

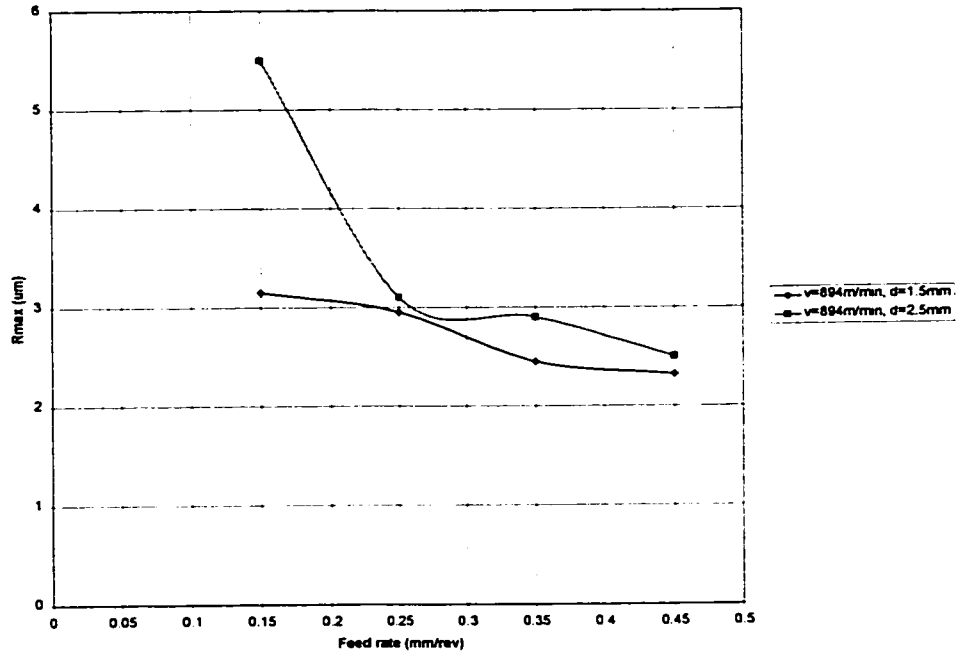

Figure 5.2.16: Variation of the surface roughness R_{max} (peak to valley) with the cutting parameters; (a) effect of cutting speed (d =1.5 mm, r = 1.6 mm, $\alpha = 0^o$); (b) effect of depth of cut (v = 894 m/min, , r = 1.6mm, $\alpha = 0^o$).

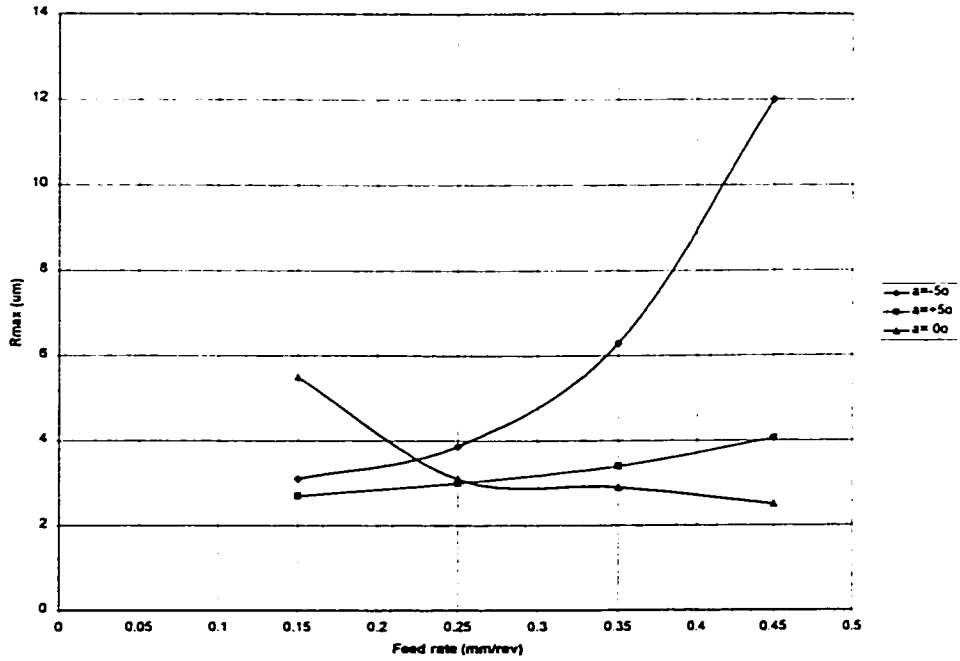

Figure 5.2.17a: Effect of PCD tool rake angle on R_{max} of the machined workpiece (v = 894 m/min, d = 2.5 mm, r = 1.6 mm)

Figure 5.2.17b: Surface roughness profiles of surfaces machined with a chip breaker clamped on top of the PCD insert (v = 894 m/min, f = 0.35 mm/rev., d = 1.5 mm, r = 1.6 mm, α=0°).

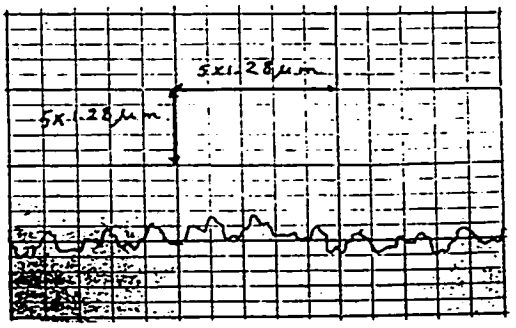

Figure 5.2.17c: Surface roughness profiles of surfaces machined with PCD tools having nose radius, r = 0.8 mm (v = 894 m/min, f = 0.25 mm/rev., d = 2.5 mm, $\alpha = 0^{o}$).

CHAPTER 6

DISCUSSION

6.1 Chip formation mechanism

The cutting parameters had a significant effect on the form of the chips produced. In general, at low feed rates and small depths of cut, the chips tended to be continuous, as shown in Fig. 6.1.1. This observation contradicts Monaghan's results [1], where discontinuous chips were always produced during turning of Al/SiC 25% SiC PMMCs. The difference in results could be attributed to one or both of the following factors:

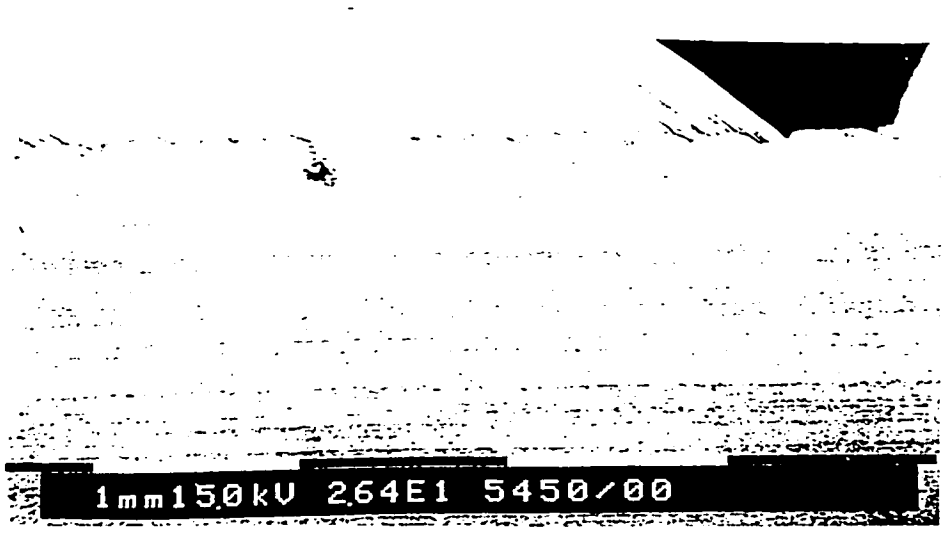

Figure 6.1.1: Typical image showing continuous chips formed at a speed of 670 m/min, d= 1.5 mm and feed rate = 0.25 mm/rev., r=1.6 mm, α= 0°.

1. Monaghan [1] used a quick stop test to study the chip formation mechanism. This type of test might be responsible for the produced form of the chips (i.e. discontinuous).
2. Monaghan [1] carried out the experimental work on Al/SiC PMMC where the SiC particles constituted 25% of the volume of the material. The difference in the SiC volume fraction changes the strain hardening properties of the composite material, which in turn influences the shear angle.

As the feed rate and/or depth of cut increase, the chips tend to be partially segmented with ductile tearing at the edges, as shown in Fig. 6.1.2. This segmentation is due to a decrease in the shear angle. The reduction in the shear angle is attributed to the "saturation" in strain hardening in the workpiece.

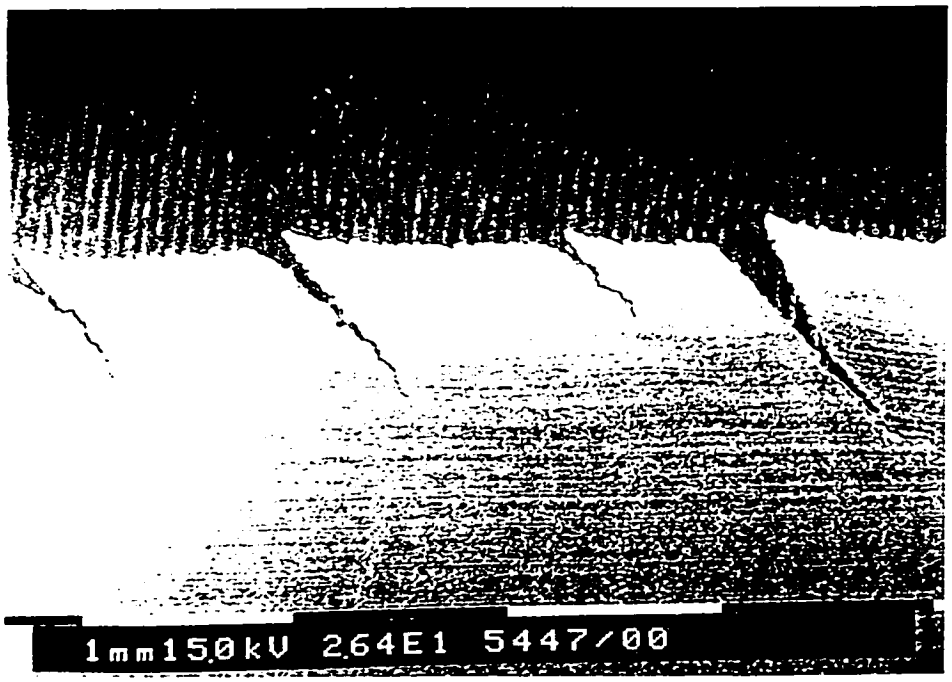

Figure 6.1.2: Typical image showing chips with ductile tearing at the edges formed at a cutting speed of 894 m/min, d=2.5 mm, f = 0.25 mm/rev., r= 1.6 mm, $\alpha = 0^{\circ}$.

At high cutting speeds shear localisation takes place due to two factors: first, geometrical softening due to the presence of the reinforcing SiC particles, and second, thermal softening due to the resulting increase in strain rates. Fig. 6.1.3 shows the SiC particles becoming aligned along the maximum shear bands. Consequently, voids are formed around the SiC particles. The voids tend to join up and form micro-cracks along the shear bands, leading to fracture/instability and the production of segmented chips.

To sum up, both geometrical and thermal softening of the workpiece material influence the chip formation mechanism, which depend on the cutting parameters. The "saw-tooth edges" of the segmented chips affect the tool wear and tool life, which are discussed in the following section.

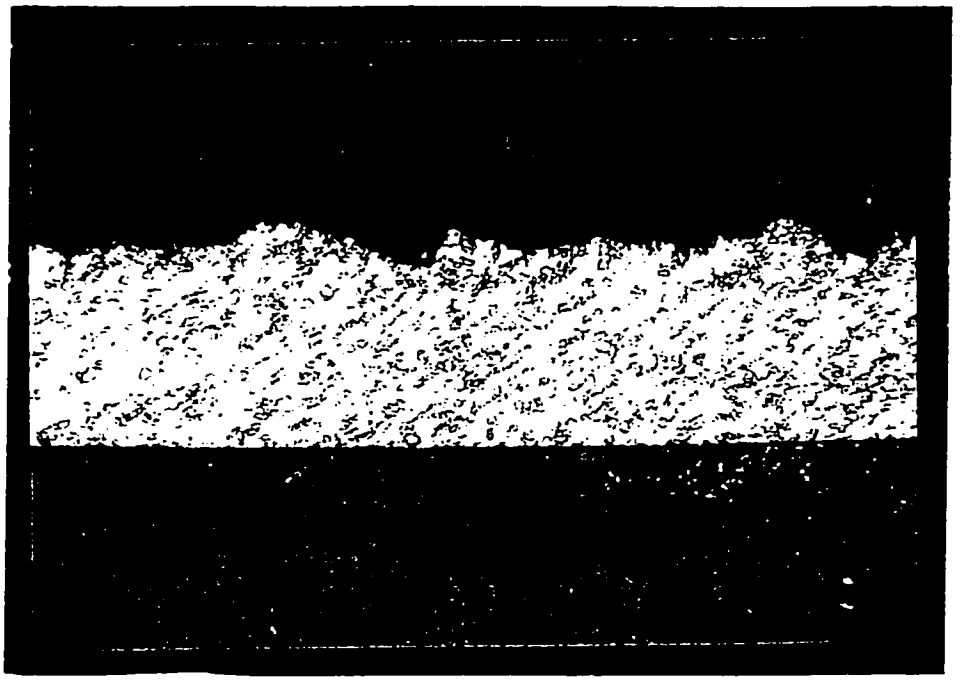

Figure 6.1.3: Typical image of the chips cross section showing the aligning of the SiC particles along the deformation bands in the chips formed at a cutting speed of 894 m/min, d=2.5 mm, f = 0.45 mm/rev., r= 1.6 mm, $\alpha = 0^{\circ}$.

6.2 Tool Wear

The primary tool wear mechanisms are:

1. Built up edge, which is formed when seizure condition prevails.

Built-up edge was observed in all tools under all cutting conditions. This is because particulate SiC/Al MMCs have all the characteristics of materials which form BUE (i.e. strain hardened two phase material under high temperature and pressure). "Crater-like" wear was also observed on some of the cutting tools. The thermal finite element analysis results indicated that the temperature is maximum at the cutting tip, which would suggest that in case a crater develops it would start right at the cutting edge (i.e. not shifted from the cutting edge as commonly observed in High Speed Steel tools [5,55,84,111]). The results are in good agreement with the experimental measurement as illustrated in Fig. 5.1.2. The difference between the analytical and the experimental temperatures is less than 30°C.

2. Abrasion due to the SiC particles.

Increasing the feed rate had a beneficial effect. As shown in Fig. 5.1.13 and Fig. 5.1.14, as the feed rate increases the tool wear decreases. In case of higher feed rates, for a fixed volume of metal removal, the tool surfaces will have less contact with the abrasive PMMC. Another advantage gained by increasing the feed rate is the change in chip form. At low feed rates, the chips formed were continuous, which are difficult and hazardous to handle. At high feed rates and high depths of cut (f > 0.35mm/rev., d > 2.0mm), the chips formed were discontinuous.

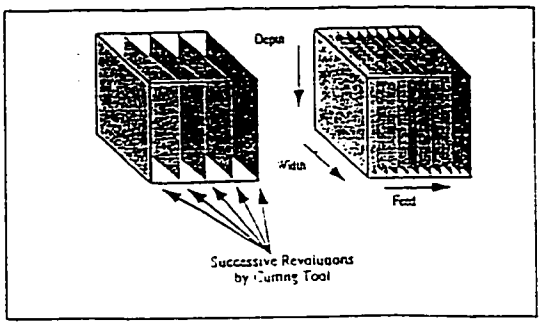

Figure 6.2.1: Illustration of the effect of feed rate on the chip/tool contact area.

6.3 Workpiece Sub-Surface Damage

Previous researchers [1-40] limited their analysis of the machined Al/SiC PMMCs workpiece to surface roughness measurements, which could be misleading since sub-surface damage is known to occur due to machining.

In all machined workpieces strain hardening occurs as depicted through the microhardness measurements shown in Fig. 5.2.10a. These results are confirmed through X-ray measurements of the residual stresses as shown in Fig. 6.3.1. This strain hardening is attributed to the increase in dislocation density as shown in Fig. 5.2.10b. Another possible explanation of the strain hardening is the formation of magnesium/silicon needle like and particle like precipitates as shown in Fig. 6.3.2a and Fig. 6.3.2b. X-ray analysis of the preciptates are shown in Fig. 6.3.3a and Fig. 6.3.3b. Magnesium/silicon compound particles form at temperatures in the vicinity of 400°C. Small particles are formed during recrystallization and then grow with time.

Since increasing the feed rate helped to reduce the tool flank wear, surface roughness also improved as previously shown in Fig. 5.2.16a and Fig. 5.2.16b. Nevertheless, a conclusive decision about the optimum cutting conditions has to take into consideration the sub-surface damage introduced into the workpiece. Fig. 6.3.4 to Fig. 6.3.7 show the effect of the different cutting parameters on the damage rate of the machined workpiece, where P/K designates the ratio of the hydrostatic stress beneath the machined surface to the shear flow strength, which is affected by the temperature and strain rate. The higher the ratio (>1.0), the less likely is the damage to occur, since cracks will tend to close due to the larger hydrostatic stress. On the other hand, when P/K ratio is less than 1.0, failure by shearing is expected. As shown in Fig. 6.3.4 to Fig. 6.3.7 the damage rate is higher at higher feed rates. Thus, for finishing operations, a low feed rate with a small tool nose radius (0.8 mm) is expected to yield lower surface roughness (Fig. 5.2.17c) and smaller damaged sub-surface layer.

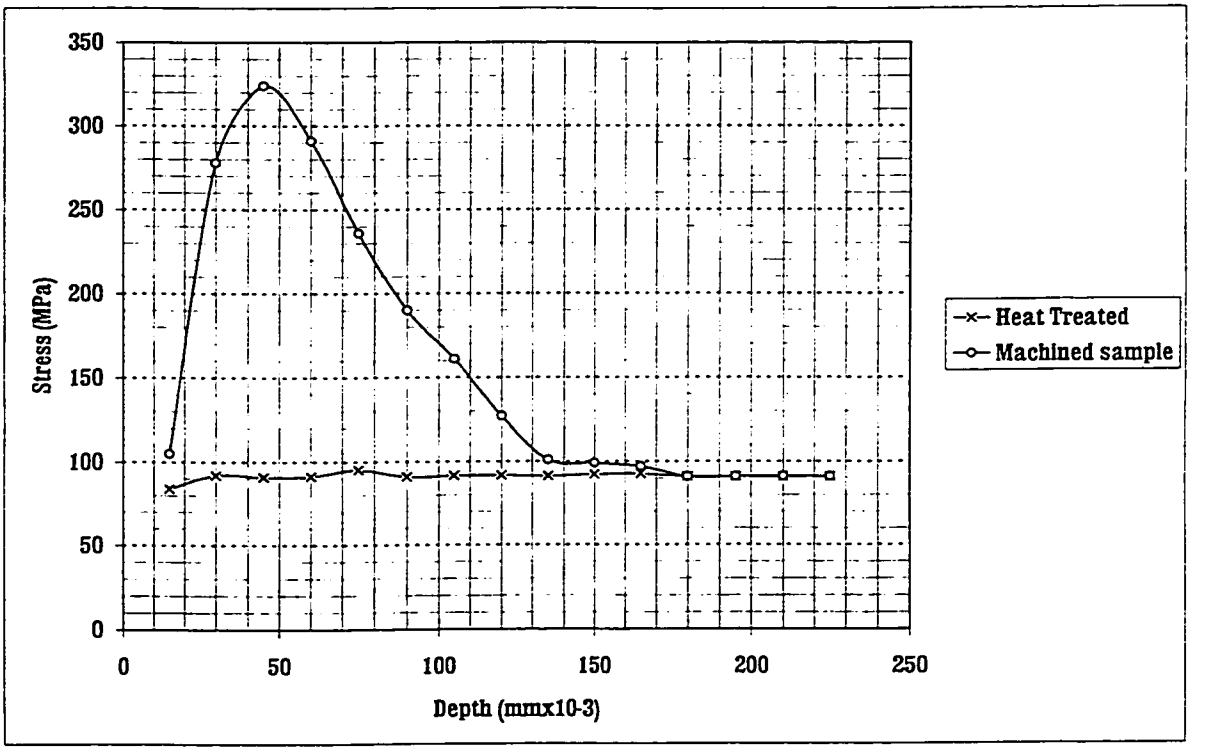

Figure 6.3.1: X-ray measurements of residual stresses beneath the machined surface

(a) (b)

Figure 6.3.2: Precipitates formed beneath the machined surface;

(a) Needle-like (b) particles

(a)

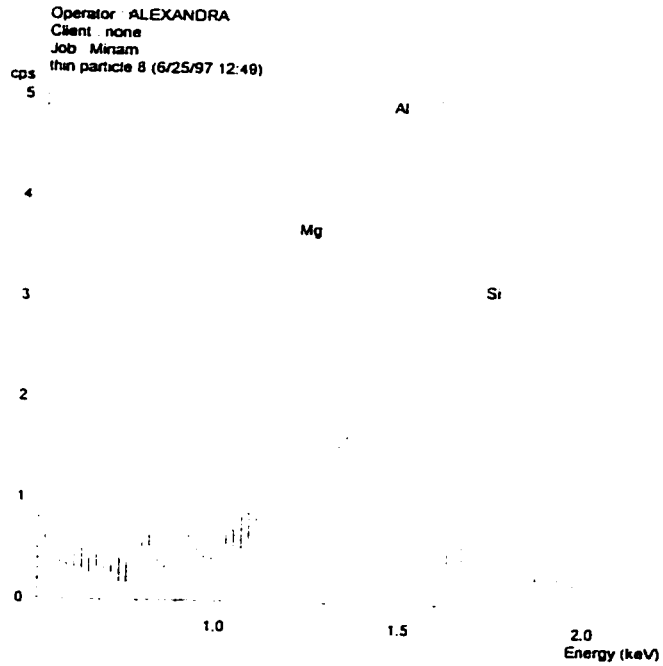

(b)

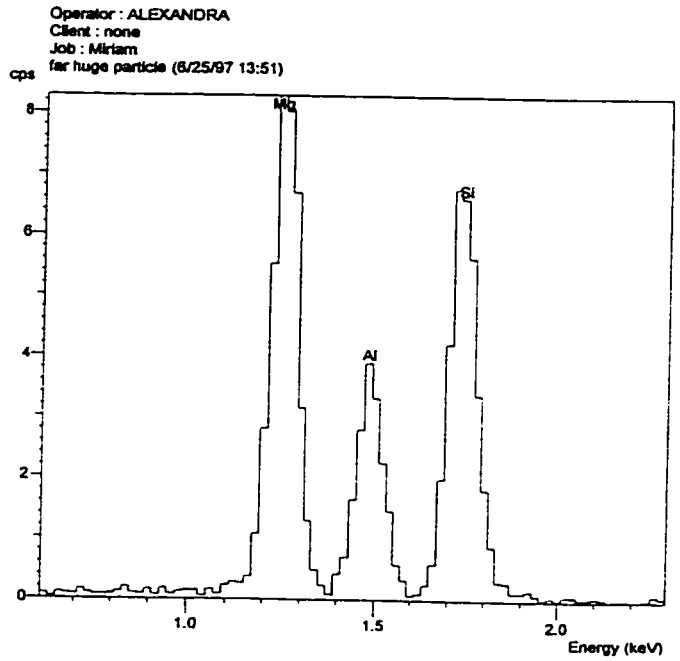

Figure 6.3.3: X-ray analysis of the precipitates shown in Fig. 6.3.2a and Fig. 6.3.2b.

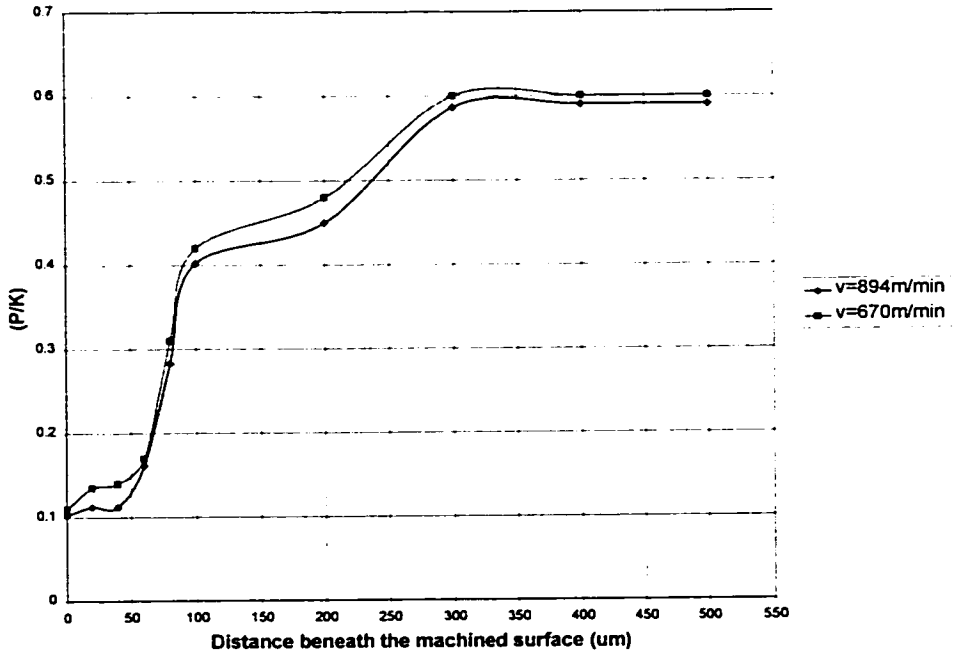

Figure 6.3.4: Effect of speed on damage rate (f=0.25 mm/rev, d=1.5 mm, r=1.6 mm, α=0°)

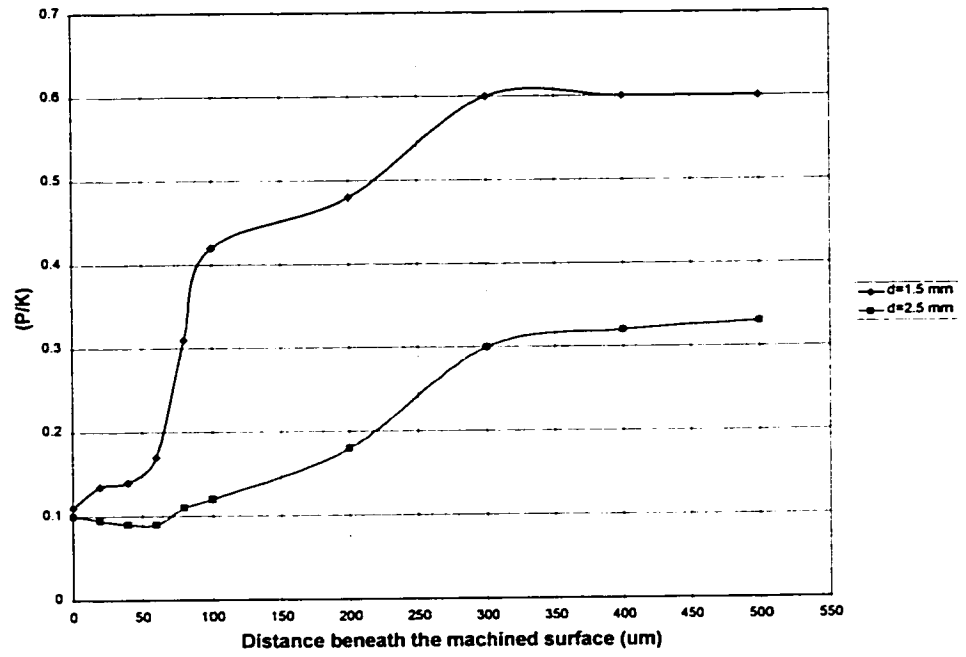

Figure 6.3.5: Effect of depth of cut on damage rate (f=0.25 mm/rev, v=670 m/min, r=1.6 mm, α=0°)

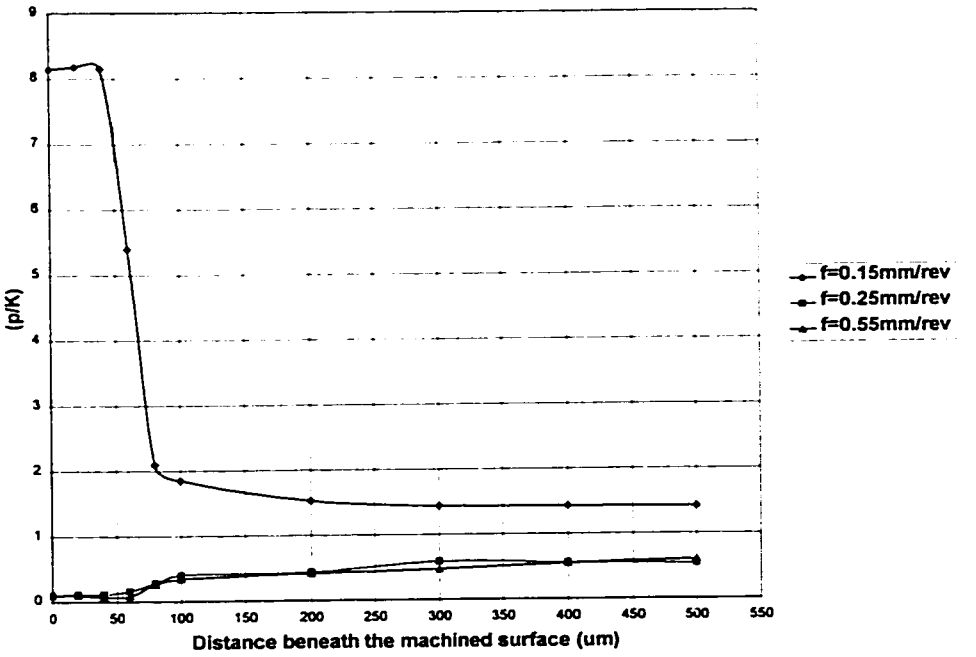

Figure 6.3.6: Effect of feed rate on damage rate (v=894 m/min, d=1.5 mm, r= 1.6mm, α=0°)

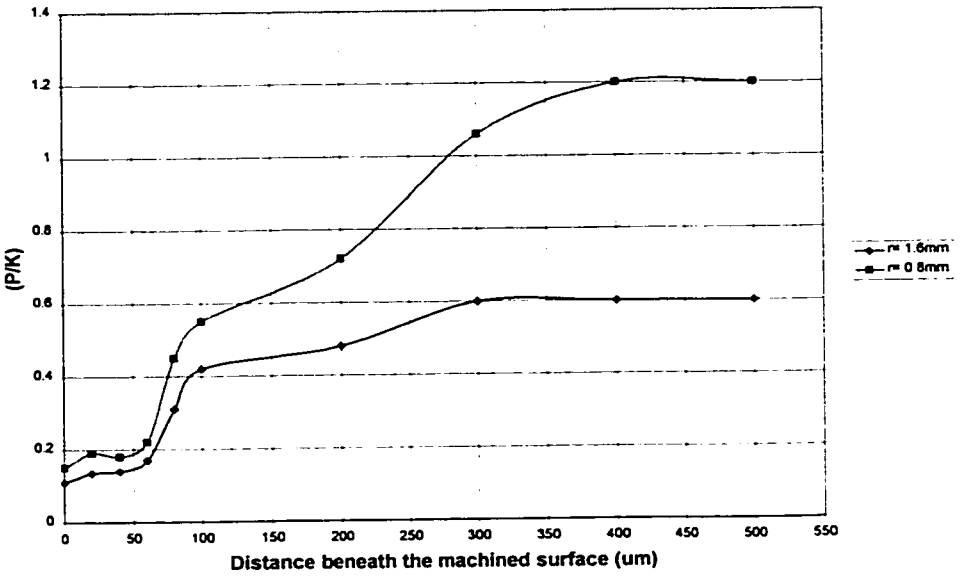

Figure 6.3.7: Effect of tool nose radius on damage rate (f=0.25 mm/rev, v=670 m/min, d=1.5 mm, α=0°)

6.4 Cost Optimisation

A simple C++ program has been developed to find out the optimum cutting conditions iteratively. The mathematical relations in the program employ the results of both the experimental and the finite element models.

The input to the program is the batch size, available cutting speeds and feed rates, required surface finish and if a certain maximum "damaged" layer beneath the surface is required. Multiple regression technique was applied to the tool wear measurements for different tool materials and tool geometries. The general form for the tool life "T" relation with the cutting parameters is:

$$T = [C_1.f^{-m} * d^{-q} * v^{-1}]^{1/n} \quad \text{..... (6.4.1)}$$

where,

T: Tool life in minutes

C_1, n ,m ,q are constants dependant on the tool geometry and tool material.

This form of tool life relation yields a coefficient of determination R^2= 0.97 for tools with 25 μm PCD layer and R^2 = 0.98 for tools with 50 μm PCD layer thickness at feed rate of 0.55 mm/rev. and d=2.0 mm. Similar relations were built for all the tools tested.

The regression technique was also applied to the surface roughness measurements, and equation (6.4.2) shows the general form for the variation of the surface roughness with the cutting parameters.

$$R_{max} = C_2 . v^a + C_3 . f^b + C_4 d^c \qquad \text{.....(6.4.2)}$$

Where, a,b,c, C_2,C_3 and C_4 are constants that depend on the tool material and tool geometry.

A similar relation is developed for the depth of the damaged layer for P/K values <1.0.

The cost for turning a part is given as:

$$C = C_o [T_c + T_h] + C_t [T_c/T] + C_{ch} [T_c/T] \qquad \text{.....(6.4.3)}$$

Where,

C: the total cost to produce one unit, dollars per piece;

C_o: cost of operating time in dollars per minute;

T_c: cutting time in minutes (for straight tuning).

$$T_c = \pi.D.L/(1000. v_c . f)$$

D: diameter of the workpiece in mm;

L : length of the workpiece in mm.

T_h: handling time in minutes;

C_t: tool cost per edge in dollars;

C_{ch}: cost of changing the tool.

Finally, the output of the program is the cost per unit for the various tool materials and tool geometries. It is believed that the utilisation of such a simple regression model, that is based on machining experiments data and the results of the finite element analysis, could help reduce the total manufacturing cost and machine downtime, and hence lead to a highly cost effective production.

CHAPTER 7

CONCLUSION

- ***Cutting Tool***

The results of the experimental work show that the cutting parameters profoundly affect the tool life and the tool wear. Thus, a model that predicts the tool temperatures and tool stresses, depending on the cutting parameters (speed, feed rate, depth of cut, tool material and tool geometry), has been developed. The model takes into account the effect of the cutting parameters on the cutting forces and temperatures. The model results are in good agreement with the experimental observations. The model, whose geometry could be fairly easily modified, is capable of predicting the tool stresses and flank wear patterns. The model was utilised to find the cutting parameters that yield the minimum tool stresses and thus the least expected tool wear. The optimum tool material and tool tool geometry (rake angle, tool nose radius and PCD layer thickness) are also determined by the model for each given set of cutting parameters.

- ***Workpiece***

The results of the experimental work show that the cutting parameters also affect the workpiece stresses and surface finish. Surface finish, however, is a reflection of the

tool flank wear. Thus, the tool F.E. model could be used to predict the resulting workpiece surface finish using interpolation techniques. In order to predict the effect of the machining stresses and temperatures on the workpiece stresses a finite element model of the workpiece and chip was developed. In the workpiece/chip model the matrix and the particles were modeled separately (in the cutting region) to enable predicting the stresses due to the thermal mismatch between the two phases. The model was capable of showing localised plastic stresses in the matrix material around the elastically deforming particles. These high stresses developing in the matrix could lead to void creation around the particles or fracture of the matrix, which were observed experimentally. The workpiece model is also used to predict the expected damage rate in the machined workpiece.

The finite element predictions of the 3-D thermo-mechanical model of oblique turning reveal that increasing the feed rate, i.e. increasing the metal removal rate, up to 0.55 mm/rev.; results in a small increase in the stresses beneath the machined surface, and a slight increase in the damage rate. On the other hand, increasing the cutting speed results in an increase in the depth of the damaged layer beneath the machined surface. The predictions of the finite element model are in good agreement with the experimental observations. The model is easily extended to calculate the residual stresses in the machined part after releasing the cutting loads.

By combining the results of the above mentioned models, the optimum cutting parameters for machining Al/20%SiC PMMC could be estimated.

The model results are further utilised in selecting the most economic cutting parameters, where the required surface finish and thickness of damaged layer are the

criteria. The model takes into consideration the batch size, which profoundly affects the selection of the tool material.

Generally, integrating the two basic elements (experimental and numerical models of the tool and workpiece) presents a rather comprehensive scheme of analysing tool wear and workpiece stresses during turning operation. Although particulate metal matrix composites have been recently extensively used by different industries, few researchers have yet attempted to analyse the stresses and tool wear during machining of PMMCs. Thus, the presented work constitutes the first attempt to integrate more than one factor involved during machining of PMMCs.

Further Research

Two future research points are recommended:

First, detailed analysis of the changes in the microstructure of the chip and the workpiece could help better understand the stress state beneath the machined surface. Analysing changes in the shear angle with the change in the material flow characteristics would help identify the chip formation mechanism.

Second, including the incipient chip formation in the F.E. model could help predict the transient stresses on both the tool and the workpiece. Including tool deflections (such as those due to chatter) through utilising DeVors' models, for instance, would help enhance the model. Also, including the heat loss through radiation in the finite element model would improve the results of the thermal analysis.

References

[1] Monaghan, J.M., "The Use of Quick Stop Test to Study the Chip Formation of a SiC/Al Metal Matrix Composite and its Matrix Alloy", "Journal of Processing of Advanced Materials, vol. 4, 1994, pp. 170-179.

[2] Ramrattan, S., Sitkins, F. and Nallakatala, M., "Optimization of the Casting and Machining Processes for Metal Matrix Composites", Proceedings of the Canadian Society for Mechanical Engineers Symposium, McMaster University, 1996, pp. 624-629.

[3] Sadat, A., "Surface characterisation of machined Inconel 718 Nickel based superalloy using controlled and natural contact length tools", International Journal of Machine Tools and Manufacturing, vol. 27, no. 3, 1987, pp. 333-342.

[4] Sadat, A.B. and Reddy, M.Y., "Surface integrity of Inconel 718 Nickel based superalloy using controlled and natural contact length tools. Part II: Lubricated", International Journal of Machine Tools and Manufacturing, vol. 33, December 1993, pp. 343-348.

[5] Abdel Hamid, A., Wifi, A.S. and El-Gallab, M., "Three dimensional finite element thermo-mechanical analysis of end milling" Journal of Material Processing Technology, May 1996, vol 56, pp. 643-654.

[6] Drawish, S. M., Niazi, A., and Ghaneya, A., "Phase stability of Duraluminum Machined with bonded and brazed carbide tools", International Journal of Machine Tools and Manufacturing vol. 32, no. 4., 1992, pp. 593-600.

[7] Tomac, N. and Tonnessen, K., "Machinability of particulate aluminum matrix composites", CIRP Annals, vol 41, 1992, pp. 55-58.

[8] Oreilly, P. and Monaghan, J., "Machinability of aluminum alloy/silicon carbide metal matrix composite", Processing of Advanced Materials, vol. 2, 192, pp.37-46.

[9] Brun, M.K. and Lee, M., "Wear characteristics of various hard materials for machining SiC reinforced aluminium alloy", Wear, vol. 104, 1985, pp. 21-29.

[10] Winert, K., "A consideration of tool wear mechanism when machining metal matrix composites (MMC), CIRP Annals, vol . 42, 1993, pp. 95-98.

[11] Cronjager, C., "Machining of fibre and particle reinforced aluminum", CIRP Annals, vol. 411, 1992, pp. 63-66.

[12] Clark, I.E., "A guide to machining metal matrix composites with syndite PCD", Machining Guide, March 1994, pp. 135-138.

[13] Vaccari, J. and Lane, C., "Machining of a new breed of aluminum" American Machinist, November 1993, pp. 56-60.

[14] Lane, C., "Drilling and tapping of SiC particle reinforced aluminum", Proceedings of Machining of Composite Materials Conference, ASM International, Pittsburgh, USA, October 1993.

[15] Lane, C., and Lennox, M., "Economics of machining cast MMC brake rotors", Duralcan report.

[16] Lane, C., "Machining discontinuously reinforced aluminum composites", Tool and Manufacturing Engineers Handbook, vol. 7.

[17] Lane, C., "Machinability of aluminum composites as a function of the matrix alloy and heat treatment", Proceedings of the Machining of Composites Symposium, ASM International, Chicago, IL, November 1992.

[18] "Face milling, end milling, drilling, reaming and tapping of SiC/A356 cast aluminum - Duralcan designation No. F3A.15S - Metal matrix composite", Metcut report no. 2852-49512-3.

[19] Lane, C., "The effect of different reinforcements on PCD tool life for aluminum composites", Duralcan report.

[20] Finn., M., and Lane, C. , "Observations on using CVD diamond in milling MMCs" Proceedings of a Symposium on Materials Issues in Machining and the Physics of the Machining Process, TMS, Chicago, IL, November 1992.

[21] Lane, C. and Finn, M., "A comparison of PCD and CVD diamond in milling MMCs", Proceedings of a Symposium on Advances in Production and Fabrication of Light Metals and Metal Matrix Composites", CIM, Edmonton, Alt., Canada, August 1992.

[22] "Duralcan Composites for Gravity Castings", Duralcan Report.

[23] "Duralcan Composites for High-Pressure Die Casting", Duralcan Report.

[24] "Duralcan Composites - Machining Guidelines", Duralcan Report.

[25] Lane, C., "The state of the art in manufacturing with MMCs", Duralcan report.

[26] Finn, M., and Srivastava, A., "Machining of advanced and engineered materials", Proceedings of the Canadian Society for Mechanical Engineers Symposium, McMaster University, 1996, pp. 616-623.

[27] Morin, E., Masounave, J. and Laufer, E.E., "Effect of drill wear on cutting forces in drilling of metal matrix composites", Wear, vol 184, 1995, pp. 11-16.

[28] Oden, M., and Ericson, T., "Near Surface Deformation in an Aluminum Silicon Carbide Whisker Composite due to Surface Machining", Journal of the American Ceramic Society, v. 79, 1996, pp. 2134-40.

[29] Chandrasekaran, H. and Johansson, J-O., "On the behaviour of fibre/particle reinforced aluminum alloy matrix composites in milling and grinding", VDI Berichte, vol. 1276, 1996, pp. 463-478.

[30] Sidhar, N., Rickman, J.M., and Srolovitz, D.J., "Effect of reinforcement morphology on matrix microcracking", Acta Metall Mater., vol. 44, no. 3, 1996, pp. 915-925.

[31] Ramakrishnan, N., "An Analytical study on strengthening of particulate metal matrix composites", Acta Metall Mater., vol 44, no. 1, 1996, pp.69-77.

[32] Corbin, S.F. and Wilkinson, D.S., "Influence of matrix strength and damage accumulation on the mechanical response of a particulate metal matrix composite", Acta Metall Mater, vol. 42, no.4, 1994, pp. 1329-1335.

[33] Wilkinson, D.S. and Embury, J.D., "The influence of particle spatial distribution on damage accumulation in metals and ceramics", Proceedings of the International Conference on Deformation and Fracture of Multi-phase Materials, France, 1995.

[34] Corbin, S.F. and Wilkinson, D.S.,"The Influence of particle distribution on the mechanical response of particulate metal matrix composites", Acta Metall Mater, vol. 42, no. 4, 1994, pp. 131-1318.

[35] Corbin, S.F., and Wilkinson, D.S., "The effects of temperature on the mechanical behaviour of a SiC particulate reinforced alloy", International Symposium Proceedings of Ceramics and MMCs, Pergamon, 1989, pp. 404-411.

[36] Davis, E.A., and Ward, I.M., "An introduction to metal matrix composites", Cambridge University Press, New York, 1993.

[37] Bao, G., Hutchinson, W. and McMeeking, R.M., "Particle reinforcement of ductile matrices against plastic flow and creep", Acta Metall Mater, vol. 39, no. 8, 1991, pp. 1871-1882.

[38] Corbin, S.F. and Wilkinson, D.S., "Low Strain Plasticity in a Particulate Metal Matrix Composite", Acta Metall Mater, vol. 42, no. 4, 1994, 1319-1327

[39] Nan, C.W. and Clarke, D.R. , "Influence of particle size and particle fracture on the elastic/plastic deformation of metal matrix composites" Acta Metall Mater., vol 44, no. 9, 1996, pp. 3801-3811.

[40] Dong, Z., and Wu, Y., "Micromechanics analysis of particulate reinforced composites and their failure mechanisms", Journal of Materials Science, vol 31, 1996, pp. 4401-4405.

[41] Lissaman, A.J. , "Principles of Engineering Production", Second Edition, Hodden and Staughton Ltd., 1982.

[42] Cook, N.H., Finnie, I.and Shaw, M.C., Journal of Enginnering for Industry, Trans. ASME, v. 76, 1954, pp. 153-162.

[43] Komanduri, R., and Brown, RH., Journal of Engineering for Industry, Trans. ASME, v. 103,1982, pp. 35-51.

[44] Sullivan, K.F, Wright, P.K. and Smith, P.D., Journal of Metals Technology, 1978, pp. 181-189.

[45] Komanduri, R.K. and Von Turkovich, B.F., Wear, vol. 69, 181, pp. 170-188.

[46] Lemonds, J. and Needleman, A., "Finite Element Analyses of Shear Localization in Rate and Temperature Dependant Solids", Mechanics of Materials, v. 5, 1986, pp. 339-361.

[47] Trigger, K.J., Zylstra, L.B. and Chao, B.T. , Journal of Engineering for Industry, Trans. ASME, v. 74, 1952, pp. 1017.

[48] Zener, C. and Hollomon, J.H., "Effect of Strain Rate Upon Plastic Flow of Steel", Journal of Applied Physics, v. 15, 1944, pp. 22.

[49] Recht, R.F., Journal of Applied Mechanics, Trans. ASME, 1964, p. 189.

[50] Culver, R.S., Metallurgical Effects at High Strain Rates, Ronda, B.M. Butchrt, J.R. Holland, C.H. Karnes, Plenum Press, New York, 1973, pp. 519-530.

[51] Backman, M.E. and Finnegan, S.A., Metallurgical Effects of High Strain Rates, Plenum Press, New York, 1973, pp. 531.

[52] Merzer, A. M., "Modeling of Adiabatic Shear Band Development from Small Imperfections", Journal of Mechanics of Physics of Solids", v. 30, 1982, pp. 323.

[53] Fressengeas, C. and Molinari, A., "Formation des bandes cisaillement: Une analyse de stabilite relative", Journal de Physique, v. 46, pp. 283.

[54] Shawki, T.G., "Analysis of Shear Band Formation at High Strain Rates and the Viscoplastic Response of Polycrystals", Ph.D. Thesis, Brown University, 1974.

[55] Tay, A.O., "A Numerical study of the temperature distribution generated during orthogonal machining", Ph.D. thesis, University of New South Wales, 1973.

[56] Brockenbrough, J.. and Zok, F.W., "On the role of particle cracking in flow and fracture of metal matrix composites", Acta Metall Mater, vol. 43, no. 1, 1995, pp. 11-20.

[57] Buckley, D.H., "Tribology in 80's" vol. 1, NASA Conference, National Aeronautics and Space Administration, 1983, pp. 19-44.

[58] Trent, E.M. , Metal Cutting, 3rd edition, Butterworth-Heinmann, London, 1984.

[59] Wright, P.K. and Trent, E.M., Journal of Iron and Steel, 1973, pp. 364.

[60] Wright, P.K., Horne, J.G. and Tabor, D., Wear, vol. 54, 1979, pp. 371-390.

[61] Bowden, F.P. and Tabor, D., Friction and Lubrication of Solids, Clarendon Press, Oxford, 1964.

[62] Greenwood, J.A. and Williamson, J.B., Proceeding of Society of Manufacturing Engineering Conference, v. 195, 1966, p.300.

[63] Ernst, H., "Physics of Metal Cutting", Machining of Metals, ASM, 1938, pp. 24.

[64] Merchant, M.E., Journal of Applied Physics, v. 16., 1945, pp. 318.

[65] DeGarmo, E.P., Black , J.T. and Kohser, A., "Materials and Processes in Manufacturing", MacMillan Publishers, 1984.

[66] Lee, E.H. and Shaffer, B.W., Journal of Applied Mechanics, v. 18, 1951, pp. 405

[67] Lee. E.H. and Shaffer B.W. "Theory of Plasticity Applied to a Problem of Machining", Journal of Applied Mechanics, vol. 73, 1951, pp. 405-413

[68] Boothroyd, G. and Dieter, G. "Fundamentals of Machining and Machine Tools", Scripta Book Company, New York, 1990.

[69] Oxley, P.L.B., Mechanics of Machining, Ellis Harwood, Chicheste, UK, 1980.

[70] Shaw, M.C., Metal Cutting Principles, Oxford Science Publications, Oxford, 1991.

[71] Wright, P.K., and Robinson, J.L., "Material Behavior in Deformation Zones of Machining Operations", Journal of Metals Technology, v. 4, 1977, pp. 240-248.

[72] Bagci A. "Discussion: Predicting Shear Plane Angle from Work Material Strain Hardening Characteristics", Journal of Engineering for Industry, Trans. ASME, vol. 105, 1983, pp. 129-131.

[73] Yellowley, I., "Observations on the Mean Values of the Forces, Torque and Specific Power in the Peripheral Milling Process", International Journal of Machine Tool Design Research, vol 25, 1985, pp. 337-346.

[74] Baily, J.A., Bhavandia, D.G., "Correlation of Flow Stress with Strain Rate and Temperature During Machining", Jpurnal of Engineering for Industry, Trans. ASME, April 1973, pp. 94-98.

[75] Muraka , P.D. Hinduja, S. , Barrow, G., "Influence of Strain, Strain Rate and Temperature on the Flow Stress in the Primary Deformation Zone in metal Cutting" International Journal of Machine Tool Design Research, vol. 21, 1981, pp. 207-216.

[76] Zorev, N.N., "Interrelation Between Shear Processes Occurring Along Tool Face and Shear Plane in Metal Cutting", Proceedings of the International Research in Production Engineering, Pittsburgh, 1963, p. 42.

[77] Palmer, W.B. and Oxley, P.L.B., "Mechanics of Orthogonal Machining", Proceedings of the Institution of Mechanical Engineers, v. 173, 1959, pp. 623-654.

[78] Kato, S., Yamarguchi, K. and Yamada, M., "Stress Distribution at the Interface Between the Tool and Chip in Machining", Journal of Engineering for Industry, Trans. ASME, May 972, pp. 683-689.

[79] Wright, P.K., "Frictional Interaction in Machining: Comparison between Transparent Saphire and Steel Cutting Tools", Journal of Metal Technology, April 1981, pp. 150-161.

[80] Kottensette, J.P., "Measuring Tool Chip Interface Temperatures", Journal of Engineering for Industry, Trans. ASME, vol. 108, 1986, pp. 101-104.

[81] Hartley,, K.A., "Temperature Measurement During the Formation of Shear Bands At High Rates of Deformation", Ph.D. Thesis, Brown University, 1986.

[82] Qureshi, A.H. and Koenigsberger, F., Annals of CIRP, v. 14, 1996, pp. 189.

[83] Zener, C. and Holloman, J., Journal of Applied Physics, v. 15, 1944, pp. 22.

[84] Orady, E., "Thermal Cycling in the Intermittent Cutting Process," Proceedings of the Second Saudi Engineering Conference, University of Petroleum and Minerals, Dahran, November 1985, pp. 3505-3528.

[85] Weiner, J.H., "Shear Plane Temperature Distribution in Orthogonal Machining", Journal of Engineering for Industry, Trans. ASME, vol. 77, 1955, pp. 1331-41.

[86] Nakayama K., "Temperature Rise of Workpiece during Metal Cutting", Journal of Engineering for Industry, Trans ASME, 1956.

[87] Rapier, A.C., "A Theoretical Investigation of the Temperature Distribution in Metal Cutting Process", Journal of Applied Physics, vol. 5, 1956.

[88] El-Gallab, M.S., "Three Dimensional Finite Element Thermo-Mechanical Analysis of End Milling", M.Sc. Thesis, The American University in Cairo, 1993.

[89] Lowen E.G. and Shaw M.C., "On the Analysis of the Cutting Tool Temperatures", Trans ASME, vol. 75, 1955, pp. 109-120.

[90] Trent, E.M., Wear, v. 128, 1988, pp. 29-81.

[91] Dearnley, P.A., Wear, v. 101, 1985, pp. 33-68.

[92] El-Gallab, M., El-Wardany, T.I., and Elbestawi, M., "Wear mechanisms of silicon carbide whisker reinforced alumina tools during high speed machining of nickel based super alloys", Proceedings of the Canadian Society for Mechanical Engineers Symposium, McMaster University, 1996, pp. 680-687.

[93] Ramanujachar, K. and Subramanian, S.V., "Micromechanisms of Tool Wear in Machining Free Cutting Steels", Wear, v. 197, 1996, pp. 45-55.

[94] Ingle, S.S, Ph.D. Thesis, McMaster University, 1993.

[95] Timothy, S.P., Acta Metall, v. 35, 1987, pp. 301-306.

[96] Takeyama, H., and Murata, R., "Basic Investigation of Tool Wear", Journal of Engineering for Industry, February 1963, pp. 33-38.

[97] Kramer, B.M., "A Comprehensive Tool Wear Model", CIRP Annals, vol 35, 1986, pp. 67-70.

[98] Takeyama, H., and Ono, T., "Basic Investigation of Built-up Edge", Journal of Engineerng for Industry, May 1968, pp. 335-342.

[99] Kannatey-Aisbu, E., ":A Transport-Diffusion Equation in Metal Cutting and Its Application to Analysis of the Rate of Flank Wear", Journal of Engineering for Industry, Vol. 107, February 1985, pp. 81-89.

[100] Bhattacharyya, A. and Ham, I., "Analysis of Tool Wear – Part I: Theoretical Models of Flank Wear", Journal of Engineering for Industry, August 1969, pp. 790-798.

[101] Tay, A.O.,Stevenson, M.G. and De Vahl Davis G., "Using the FEM to Determine the Temperature Distributions in Orthogonal Machining", Journal of Engineering for Industry, Tans. ASME, vol 88, pp. 627-638.

[102 Klamecki, B.E., "Incipient chip formation in metal cutting - A 3-D finite element analysis", PhD Thesis, University of Illinois, 1973.

[103] Osui, E. and Takeyama, Journal of Engineering for Industry, Trans. ASME, v. 82, 1960, pp. 303.

[104] Tlusty and Massood, Journal of Engineering for Industry, Trans. ASME, v. 100, 1978, pp. 403.

[105] Hsu, J.C. , International Conference on Production Improvement – New Tools and Application, International Technology Researh Institute, Chicago, 1979.

[106] Stevenson, M.G., Wright, P.K. and Chow, J.C., "Further Developments in Applying the FEM to the Calculation of Temperature Distributions in Machining and Comparisons with Experiment", Journal of Engineering for Industry, Trans ASME, August 1993, pp. 149-154.

[107] Iwata, K., Osakada, K. and Terasaka, Y., "Process modelling of orthogonal cutting by rigid plastic finite element method", Journal of Engineering for Industry, April 1984, pp. 132-138.

[108] Strenkowski, J.S., and Carrol, J.T., "A finite element model of orthogonal metal cutting", Journal of Engineering for Industry, November 1990, pp. 349-354.

[109] Orady, E., "Thermal Cycling in Intermittent Cutting", Ph.D. Thesis, McMaster University, 1985.

[110] Dokainish, M.A. , Elbestawi, M. , Polat, U., and Tole, B., Analysis of Stresses During Exit In Interrupted Cutting With Chamfered Tools", International Journal of Machine Tools and Manufacturing, v. 29, 1989, pp. 519-534.

[111] Younis, M.A., "Mechanical and thermal stresses in clamped, brazed and bonded carbide tools", Journal of Engineering for Industry, Nov. 1992, pp. 377-385.

[112] Strenkowski, J.S. and Moon, K.J., "Finite element prediction of chip geometry and tool/workpiece temperature distribution in orthogonal metal cutting", Journal of Engineering for Industry, August 1991, pp. 313-318.

[113] Chan, J.F.L. and Braiden, P.M., International Conference for Numerical Methods, Venice, 1981, pp. 407.

[114] Komvopolous, K. and Erpenbeck, S.A., "Finite element modelling of orthogonal metal cutting", Journal of Engineering for Industry, August 1991, pp. 253-267.

[115] Stephenson, D.A. and Ali, "Tool Temperatures in Interrupted Metal Cutting", Journal of Engineering for Industry, Trans. ASME , November 1990, pp. 127-136.

[116] Ueda, K., "Rigid Plastic Finite Element Analysis of Three Dimensional Deformation Field in Chip Formation Process", CIRP Annals, v. 42, 1993, pp. 35-38.

[117] Ahmad, M.M., Draper, W.A. and Derricott, R.T., "Ann Application of the Finite Element Method to the Prediction of the Cutting Tool Performance", International Journal of Machine Tools and Manufacturing, v. 29, 1989, pp. 197-206.

[118] Bayoumi, A.E. and Zbib V.H., "Charcterization of Chip formation in Shear Banding in Orthogonal Machining Using Finite Element Analysis", Symposium on Material Instabilities, ASME WAM, 1994.

[119] Sekhon, G.S. and Chenot, J.L., "Numerical Simulation of Continuous Chip Formation During Non-Steady Orthogonal Cutting", Engineering Computations, v. 10, 1993, pp. 31-48.

[120] Zang, B. and Bagchi, A., "Finite Element Simulation of Chip Formation and Comparison With Machining Experiments", Journal of Engingeering for Industry, v. 116, 1994, pp. 289-297.

[121] Shih, A.J., "Finite element simulation of orthogonal metal cutting", Journal of Engineering for Industry, Trans. ASME, February 1995, pp. 84-91.

[122] Essam, M., and Elbestawi, M. "Cutting Termperature of Ceramic Tools", International Journal of Machine Tools and Manufacturing, 1996.

[123] Marusich, T.D. and Ortiz, M. , "A Finite Element Study of Chip Formation in High Speed Machining", Manufacturing Science and Engineering, ASME Trans., 1995, pp. 245-258.

[124] Athavale, S.M. and Strenkowski, J.S., "Material Damage Based Model for Predicting Chip Breakability", Journal of Manufacturing Science and Engineering, v. 119, 1997, pp. 675-680.

[125] El-Gallab, M. , "Literature review on mechanics of strengthening in particulate metal matrix composites", report presented to M. Skald, McMaster University, Department of Mechanical Engineering, January 1997.

[126] Zahl., D.B. and McMeeking, R.M., "The influence of residual stresses on the yielding of metal matrix composites", Acta Metall Mater, vol. 39, no. 6, pp. 1117-1122.

[127] Chinghua, H. and Kobayashi, S., "Finite element deformation analysis of metal matrix composites", International Journal of Machine Tools and Manufacturing, vol 32, no. 4, 1992, pp. 601-617.

[128] Brayshaw, J. B. and Pindera, M., "The effect of matrix constitutive model on residual thermal stresses in MMC", Journal of Engineering Materials and Technology, vol 116, October 1994, pp. 505-511.

[129] Caceres, C.H. and Griffiths, J.R., "Damage by the cracking of SiC particles in an Al-7Si-0.4Mg casting alloy", Acta Metall Mater., vol. 44, no. 1, 1996, pp. 25-33.

[130] Kiser, M.T., Zok, F.W., and Wilkinson, D.S., "Plastic flow and fracture of a particulate metal matrix composite", Materials, December 1995.

[131] Ahn, Y., Chandrasekar, S. and Farris, T.N., "Determination of Surface Residual Stresses in Machined Ceramics Using Indentation Fracture", Journal of Manufacturing Science and Engineering, Trans. ASME, v. 118, 1196, pp. 483-489.

[132] Wright, P.K., "Measurement of Residual Stresses in Metal Matrix Composites" Proceedings of the International Gas Turbine and Aeroengine Congress and Exposition, ASME Trans, Cincinnati, Ohio, 1993, pp. 1-8.

[133] Todd, R.T. and Derby, B., "Deconvolution of Measured Internal Strain Distribution Function for Al2O3/SiCp Composites from Neutron Diffraction Results", Proceedings of the Symposium on Residual Stresses in Composites – Measurement, Modeling and Effects on Thermo-Mechanical Behavior", Denver, Colorado, 1993, pp. 147-160.

[134] Arsenault, R.J. and Krawitz, A.D., "Thermal Residual Stresses in Discontinuous Metal Matrix Composites", Proceedings of the Symposium on Residual Stresses in Composites – Measurement, Modeling and Effects on Thermo-Mechanical Behavior", Denver, Colorado, 1993, pp. 115-130.

[135] Cerretti, M., Braham, C. , Lebun, J.L., Bannafe, J.P. and Perrin, J.L., "Residual Stress Analysis by Neutron and X-Ray Diffraction Applied to the Study of 2-Phase Materials: Metal Matrix Composites", Journal of Exerimental Techniques, v. 20, 1996, pp. 14-18.

[136] Liu, C. , Michal, G. and Lewandowski, J.J., "Residual Stresses in Al Based SiC Particulate Composites", Proceedings of the Symposium on Residual Stresses in Composites – Measurement, Modeling and Effects on Thermo-Mechanical Behaviour", Colorado, 1993, pp. 239-256.

[137] Levy, A. and Papazian, J.M., "Thermally Induced Residual Stresses in Discontinuously Reinforced Composites", Proceedings of the Symposium on Residual Stresses in Composites – Measurement, Modeling and Effects on Thermo-Mechanical Behaviour", Denver, Colorado, 1993, pp. 305-320.

[138] Ho, S. and Saigal, A., "Thermal Residual Stresses in Cast SiC/Al Composites", Proceedings of the Symposium on Residual Stresses in Composites –

Measurement, Modeling and Effects on Thermo-Mechanical Behaviour", Denver, Colorado, 1993, pp. 55-66.

[139] Peterson, G., Design and Analysis of Experiments, Marcel Dekker, Inc., New York, New York, 1985.

[140] Keller, G., Warrack, B. and Bartel, H., Statistics for Management and Economics – A Systematic Approach, second edition, Wadsworth Publishing Inc., California, 1988.

[141] Lorenzen, T., Design of Experiments – No Name Approach , Marcel Dekker, Inc. New York, New York, 1993.

[142] Wright, P.K., "Predicting the Shear Plane Angle in Machining From Workmaterial Strain-Hardening Characteristics", Journal of Engineering for Industry, Trans. ASME, v. 104, pp.285292, 1982.

[143] I-DEAS Master Series 6 - Manual, Structural Dynamics Corporation, 1998.

[144] MSC/NASTRAN version 70, The MacNeal-Schwendler Corporation, 1997.

[145] Maple view, v. 4.4

[146] El-Gallab, M. and Sklad, M., "Machining of Al/SiC Particulate Metal Matrix Composites. Part I: Tool Performance", Journal of Materials Processing Technology, v. 83, 1998, pp. 151-158.

[147] El-Gallab, M. and Sklad, M., "Machining of Al/SiC Particulate Metal Matrix Composites. Part II: Workpiece Surface Integrity", Journal of Materials Processing Technology, v. 83, 1998, pp. 277-285.

[148] El-Gallab, M. and Sklad, M., "Machining of Al/SiC Particulate Metal Matrix Composites. Part III: Comprehensive Tool Wear Models", Accepted for publication in the Journal of Materials Processing Technology.

[149] El-Gallab, M. and Sklad, M.,"Stresses in Metal Matrix Composites Due to Machining", Accepted for presentation and publication in the proceedings of the 8th International Conference on Material Behavior, Univ. of Victoria, British Colombia, May 1999.

[150] El-Gallab, M. and Sklad, M.,"Improving the Economics of Machining PMMCs", Submitted for review at the proceedings of the Machining Symposium "Symposium on Machining Science and Technology", ASME sponsored, Nashville, 1999.

[151] El-Gallab, M. and Sklad, M., "Machining of Al/SiC Particulate Metal Matrix Composites. Part IV:Modeling of Workpiece Residual Stresses", under preparation for publication in the Journal of Materials Processing Technology.

[152] Bliki, I., "Economic and Technical Advantages of Utilizing PCD, PCBN and CBN Ceramic Tool Materials in Metal Removal Applications", Proceedings of a Conference on Superabrasives. sponsored by the Society of Manufacturing Engineers, SME, Chicago, Illinois, 1991.

[153] "Hidden Aspects of Superabrasives Economics", GE Superabrasives Report.

[154] Bhattacharyya, A., and Faria-Gonzalez, R., "Regression Analysis for Predicting Surface Finish and its Application in the Determination of the Optimum Machining Conditions", Journal of Engineering for Industry, Trans. ASME, 1970, pp. 711.

[155] Pekelharing, A.J., "The Exit Failure in Interrupted Cutting", CIRP Annals, v. 27, pp.5-10, 1978.